

SNE SIMULATION NOTES EUROPE



Journal on Developments and Trends in Modelling and Simulation

EUROSIM Scientific Membership Journal

Vol. 32 No.2, June 2022

ISSN Online 2306-0271

DOI 10.11128/sne.32.2.1060

ISSN Print 2305-9974

ISBN Print 978-3-903311-31-2



EUROSIM 2023:

Simulation for a Sustainable Future

June 28-30, 2023, Amsterdam, The Netherlands

The 11th edition of the EUROSIM Congress is dedicated to a sustainable future. And there is no better place than Amsterdam for celebrating the link between simulation and sustainability. You will be pleased to discover the fascinating and vibrant city of Amsterdam, a hub for many sectors such as logistics, ICT, art, financial and business services, fashion, and many others.

Authors are welcome to submit their contributions to the following, but not limited to areas such as:
Agent-Based Simulation • Methodology • Supply Chain Management, Logistics & Transportation • Industrial Case Studies • Complex, Intelligent, Adaptive and Autonomous Systems (CIAAS) • Data Science for Simulation • Environment and Sustainability Applications • Gaming • Healthcare Applications • Hybrid Simulation • Manufacturing Applications • Military Applications • Simulation in Education • Simulation-Optimization • Advanced Tutorials/workshops from academics and industry, PhD Track and many more

Paper deadlines and requirements:

The congress encourages researchers and practitioners to submit their original contributions as:

- Discussing paper (2-page extended abstract); peer-reviewed; accepted for presentation
- Full paper, (max 8 pages); peer-reviewed; accepted for presentation; published in the Congress proceedings; considered for journal publication.

Instructions, information, submission forms, and procedures are available on the EUROSIM 2023 website www.eurosim2023.eu. Each accepted contribution requires a paid registration.

Important dates:

- Extended abstract/ Full paper submission deadline: 30 November 2022
- Notification of acceptance: 28 February 2023
- Final paper submission deadline: 31 March 2023
- Early bird registration deadline: 30 April 2023
- Last call for registration deadline: 31 May 2023
- EUROSIM Congress 2023: 28-30 June 2023

Submit your paper at: <https://easychair.org/conferences/?conf=eurosim2023>

Editorial

Dear Readers, This issue SNE 32(2) presents submitted contributions, post-conference contributions from ASIM conferences, and the 'last' post-conference contributions from the EUROSIM 2019 congress, completing the two SNE Special Issues EUROSIM Congress 2019. The application-oriented contributions deal with the operating behaviour of an industrial Diesel engine (B. H. Herrmann et al.), with an adapted laboratory for mobile robotics t (by D. Gallarta Sáenz et al.), with pulse wave analysis attractor reconstruction (by C. Hörandtner et al.), highly viscous non-isothermal fluids with free surface (by E. Skeli et al.), and with simulation model to increase the resilience of Public Transit Networks (by O. Ullrich and D. Lücknerath). The methodological oriented contributions present approaches and case studies for order reduction in deterministic microscopic models (M. Rößler, N. Popper), a procedural model approach for energy-oriented simulation studies (B. Jacobsen et al.), and advanced machine learning for recursive data-based modelling by E. K. Juuso). Both contribution types underline the broad variety of classical simulation areas and looking into new areas.

SNE Volume 32 continues a SNE tradition: Vlatko Čerić, Past President of the Croatian Simulation Society, provides his artwork as cover pictures for SNE covers. For this volume, the artist and simulationist Vlatko Čerić has chosen four algorithmic art pictures from the series AMULETS, for this issue Amulet no. 3.

I would like to thank all authors for their contribution, and thanks to the editorial board members for review and support, and to the organizers of the EUROSIM conferences for co-operation in post-conference contributions. And many thanks to the SNE Editorial Office for layout, typesetting, preparations for printing, electronic publishing, and much more. And last but not least we are glad, that after the series of virtual conferences we can promote again EUROSIM face-to-face conferences, MATHMOD 2022 Vienna and ASIM 2022 Vienna in July 2022 (www.mathmod.at, www.asim-gi.org/asim2022; 'conferences as they used to be'), and the EUROSIM Congress 2023, June 2023 Amsterdam - see cover pages.

Felix Breitenecker, SNE Editor-in-Chief, eic@sne-journal.org; felix.breitenecker@tuwien.ac.at

Contents SNE 32(2)

Online SNE 32(2), DOI 10.11128/sne.32.2.1060 ARGESIM Publisher, Vienna, www.argesim.org Print SNE 32(2) ISBN 978-3-903311-31-2 TU Verlag Vienna, Print-on-Demand, www.tuverlag.at	
Modeling the Operating Behavior of an Industrial Diesel Engine used as an Electrical Power Generator. <i>B.H. Herrmann, D. Jörss, C. Fink</i>	55
Adapted Laboratory for Mobile Robotics Teaching and its Application to Coordinated Control of Robots. <i>D. Gallarta Sáenz, P. Álvarez Benito, J. Rico-Azagra, M. Gil-Martínez</i>	63
Pulse Wave Analysis by Quantified Reconstructed Attractors. <i>C. Hörandtner, M. Bachler, S. Wassertheurer, F. Breitenecker, C.C. Mayer</i>	69
Model Order Reduction of Deterministic Microscopic Models - A Case Study. <i>M. Rößler, N. Popper</i>	79
Procedure Model to Estimate Bundled Energy Demand for Energy-oriented Simulation Studies. <i>B. Jacobsen, M. Stange, M. Münnich, T. Schwarting</i>	85
Model Reduction of Highly Viscous, Non-isothermal Fluids with Free Surface Using Perturbation Theory. <i>E. Skeli, D. Weidemann, K. Panreck</i>	93
A Bi-Modal Simulation Model to Increase the Resilience of Public Transit Networks. <i>O. Ullrich, D. Lücknerath</i>	103
Advanced Machine Learning in Recursive Data-based Modelling. <i>E. K. Juuso</i>	113
EUROSIM Societies Short Info	N1 – N8
Schedule for EUROSIM Conferences	Cover Pages

SNE Contact & Info

SNE Online ISSN 2306-0271

SNE Print ISSN 2305-9974

→ www.sne-journal.org

✉ office@sne-journal.org, eic@sne-journal.org

✉ SNE Editorial Office

Johannes Tanzler (Layout, Organisation),
Irmgard Husinsky (Web, Electronic Publishing),
Felix Breitenecker (Organisation, Author Mentoring)
ARGESIM/Math. Modelling & Simulation Group,
Inst. of Analysis and Scientific Computing, TU Wien
Wiedner Hauptstrasse 8-10, 1040 Vienna, Austria

SNE SIMULATION NOTES EUROPE

WEB: → www.sne-journal.org, DOI prefix 10.11128/sne

Scope: Developments and trends in modelling and simulation in various areas and in application and theory; comparative studies and benchmarks (documentation of ARGESIM Benchmarks on modelling approaches and simulation implementations); modelling and simulation in and for education, simulation-based e-learning; society information and membership information for EUROSIM members (Federation of European Simulation Societies and Groups).

Editor-in-Chief: Felix Breitenecker, TU Wien, Math. Modelling Group

✉ Felix.Breitenecker@tuwien.ac.at, ✉ eic@sne-journal.org

Print SNE and Print-on-Demand: TU-Verlag, Wiedner Hauptstrasse 8-10, 1040, Vienna, Austria – www.tuverlag.at

Publisher: ARGESIM ARBEITSGEMEINSCHAFT SIMULATION NEWS
c/o Math. Modelling and Simulation Group, TU Wien / 101,
Wiedner Hauptstrasse 8-10, 1040 Vienna, Austria;
www.argesim.org, ✉ info@argesim.org on behalf of
ASIM www.asim-gi.org and EUROSIM → www.eurosim.info

© ARGESIM / EUROSIM / ASIM 2022

SNE - Aims and Scope

Simulation Notes Europe (SNE) provides an international, high-quality forum for presentation of new ideas and approaches in simulation - from modelling to experiment analysis, from implementation to verification, from validation to identification, from numerics to visualisation - in context of the simulation process.

SNE seeks to serve scientists, researchers, developers and users of the simulation process across a variety of theoretical and applied fields in pursuit of novel ideas in simulation and to enable the exchange of experience and knowledge through descriptions of specific applications. SNE follows the recent developments and trends of modelling and simulation in new and/or joining application areas, as complex systems and big data. SNE puts special emphasis on the overall view in simulation, and on comparative investigations, as benchmarks and comparisons in methodology and application. For this purpose, SNE documents the ARGESIM Benchmarks on *Modelling Approaches and Simulation Implementations* with publication of definitions, solutions and discussions. SNE welcomes also contributions in education in/for/with simulation.

A News Section in SNE provides information for EUROSIM Simulation Societies and Simulation Groups.

SNE, primarily an electronic journal, follows an open access strategy, with free download in basic layout. SNE is the official membership journal of EUROSIM, the *Federation of European Simulation Societies and Simulation Groups* – www.eurosim.info. Members of EUROSIM societies are entitled to download SNE in an elaborate and extended layout, and to access additional sources of benchmark publications, model sources, etc. Print SNE is available for specific groups of EUROSIM societies, and starting with Volume 27 (2017) as print-on-demand from TU Verlag, TU Wien. SNE is DOI indexed by CrossRef, identified by DOI prefix 10.11128, assigned to the SNE publisher ARGESIM (www.argesim.org).

Author's Info. Individual submissions of scientific papers are welcome, as well as post-conference publications of contributions from conferences of EUROSIM societies. SNE welcomes special issues, either dedicated to special areas and/or new developments, or on occasion of events as conferences and workshops with special emphasis.

Authors are invited to submit contributions which have not been published and have not being considered for publication elsewhere to the SNE Editorial Office.

SNE distinguishes different types of contributions (*Notes*), i.e.

- TN Technical Note, 6 – 10 p.
- PN Project Note 6 – 8 p.
- SW Software Note , 4 – 6 p.
- ON Overview Note – only upon invitation, up to 14 p.
- EN Education Note –6 – 8 p.
- SN Short Note, max. 6 p.
- BN Benchmark Note, 2 – 8 p.
- BNE Edu B.Note, 2 10 p
- STN Student Note, 4-8 p, inv.

Further info and templates (doc, tex) at SNE's website.

www.sne-journal.org

SNE Editorial Board

SNE - Simulation Notes Europe is advised and supervised by an international scientific editorial board. This (increasing) board is taking care on peer reviewing of submission to SNE:

- Felix Breitenecker, Felix.Breitenecker@tuwien.ac.at
TU Wien, Math. Modelling, Austria, Editor-in-chief
- David Al-Dabass, david.al-dabass@ntu.ac.uk,
Nottingham Trent University, UK
- Maja Atanasijevic-Kunc, maja.atanasijevic@fe.uni-lj.si
Univ. of Ljubljana, Lab. Modelling & Control, Slovenia
- Aleš Belič, ales.belic@sandoz.com
Sandoz / National Inst. f. Chemistry, Slovenia
- Peter Breedveld, P.C.Breedveld@el.utwente.nl
University of Twente, Netherlands
- Agostino Bruzzone, agostino@itim.unige.it
Universita degli Studi di Genova, Italy
- Francois Cellier, fcellier@inf.ethz.ch, ETH Zurich, Switzerland
- Vlatko Čerić, vceric@efzg.hr, Univ. Zagreb, Croatia
- Russell Cheng, rhc@maths.soton.ac.uk
University of Southampton, UK
- Roberto Cianci, cianci@dime.unige.it,
Math. Eng. and Simulation, Univ. Genova, Italy
- Eric Dahlquist, erik.dahlquist@mdh.se, Mälardalen Univ., Sweden
- Umut Durak, umut.durak@dlr.de
German Aerospace Center (DLR)Braunschweig , Germany
- Horst Ecker, Horst.Ecker@tuwien.ac.at
TU Wien, Inst. f. Mechanics, Austria
- Vadim Engelson, vadime@mathcore.com
MathCore Engineering, Linköping, Sweden
- Peter Groumpos, groumpos@ece.upatras.gr
Univ. of Patras, Greece
- Edmond Hajrizi, ehajrizi@ubt-uni.net
University for Business and Technology, Pristina, Kosovo
- Glenn Jenkins, GLJenkins@cardiffmet.ac.uk
Cardiff Metropolitan Univ., UK
- Emilio Jiménez, emilio.jimenez@unirioja.es
University of La Rioja, Spain
- Esko Juuso, esko.juuso@oulu.fi
Univ. Oulu, Dept. Process/Environmental Eng., Finland
- Kaj Juslin, kaj.juslin@enbuscon.com, Enbuscon Ltd, Finland
- Andreas Körner, andreas.koerner@tuwien.ac.at
TU Wien, Math. E-Learning Dept., Vienna, Austria
- Francesco Longo, f.longo@unical.it
Univ. of Calabria, Mechanical Department, Italy
- Yuri Merkurjev, merkur@itl.rtu.lv, Riga Technical Univ.
- David Murray-Smith, d.murray-smith@elec.gla.ac.uk
University of Glasgow, Fac. Electrical Engineering, UK
- Gasper Music, gasper.music@fe.uni-lj.si
Univ. of Ljubljana, Fac. Electrical Engineering, Slovenia
- Thorsten Pawletta, thorsten.pawletta@hs-wismar.de
Univ. Wismar, Dept. Comp. Engineering, Wismar, Germany
- Niki Popper, niki.popper@dwh.at, dwh Simulation Services, Austria
- Kozeta Sevrani, kozeta.sevrani@unitir.edu.al
Univ. Tirana, Inst.f. Statistics, Albania
- Thomas Schriber, schriber@umich.edu
University of Michigan, Business School, USA
- Yuri Senichenkov, sneyb@dcn.infos.ru
St. Petersburg Technical University, Russia
- Michal Štepanovský, stepami9@fit.cvut.cz
Technical Univ. Prague, Czech Republic
- Oliver Ullrich, oliver.ullrich@iais.fraunhofer.de
Fraunhofer IAIS, Germany
- Siegfried Wassertheurer, Siegfried.Wassertheurer@ait.ac.at
AIT Austrian Inst. of Technology, Vienna, Austria
- Sigrid Wenzel, S.Wenzel@uni-kassel.de
Univ. Kassel, Inst. f. Production Technique, Germany
- Grégory Zacharewicz, gregory.zacharewicz@mines-ales.fr
IMT École des Mines d'Alès, France

Modeling the Operating Behavior of an Industrial Diesel Engine used as an Electrical Power Generator

Daniel Jörss, Bert Henrik Herrmann, Christian Fink*

Department of Mechanical / Process and Environmental Engineering, Wismar University of Applied Sciences, Philipp-Müller-Str. 14, 23966 Wismar, Germany; **Christian.Fink@hs wismar.de*

SNE 32(2), 2022, 55-61, DOI: 10.11128/sne.32.tn.10601
 Received: 2021-07-10 (selected ASIM WS STS 2021 Postconf.
 Publication; Revised: 2021-12-14; Accepted: 2022-02-15
 SNE - Simulation Notes Europe, ARGESIM Publisher Vienna,
 ISSN Print 2305-9974, Online 2306-0271, www.sne-journal.org

Abstract. Within the research project SIDYN the operating behavior of an electric power generator in an isolated, dynamically loaded grid is to be described and predicted by using simulation approaches. The stage of development shown in this paper includes a coupled thermodynamic/mechanic engine model, which has to be extended by a mechanic/electrical generator-grid-model in the course of the project. For verification of the engine simulation, model measurements were carried out at the engine test bed at Wismar University. One of the key measures to enable simulations of different load scenarios and its impact on the system is the precise definition of subsystem interfaces. To do so, an approach described in [2] is implemented into MATLAB Simulink®. To characterize the controlling behavior of the industrial engine the interfaces between the transient torque and angular velocity of the drive train were observed. Considering the existing experimental setup, it can be concluded that good results could be achieved with the present model. The calculated and simulated cylinder pressure curves show a high level of agreement at various stationary operating points. However, to strive for the calculation of transient operation behaviors, the model as well as the engine test bed require further extension.

Introduction

To produce electrical energy in isolated grids GENSETS (combination of internal combustion engine and electric generator) are commonly used.

By doing so, the high energy density of fuels is converted into electrical energy. Already during the design process of the GENSET the main focus is put on the quantification of the interaction between system components and the identification of optimized system configuration and operational modes. The impact of dynamic grid load on the electric network and the reaction of the internal combustion engine has a direct impact on network frequency, when using GENSETS in isolated operating mode. Highly dynamic electric loads in isolated grids as they can be found in steel- and cement factories or on ships with hybrid drive trains will affect grid stability inducing the risk of negative repercussions on other connected electric components. Thus, a reliable and accurate prediction of the system behavior and occurring interactions are of great importance in the system design and configuration process. So far calculations like this were made by hand or using simulations that do not cover the whole system. Uncertainties may lead to oversized system components causing high procurement costs.

Basically, conventional simulations are based on engine speed-based models [7]. But the approach of this research project includes the assumption, that the development of an angle of rotation resolved calculation offers a more precise declaration of the whole system behavior. Due to that the plant can be optimized by many more parameters. As a result of this optimization process the systems economic efficiency can be raised while ensuring a high degree of stability and a minimum of network fluctuations.

Apart from a safe and good system performance, economic and ecologic aspects, such as efficiency and emissions can be defined as target values within the simulation model.

The simulation approach consists of two system models connected with an interface.

One of the systems is the thermodynamic/mechanic engine model and the second system covers up the mechanic/electrical generator-grid-model. As one of the first steps a 2.9-liter turbocharged diesel industrial engine and a generator working as an asynchronous machine are modelled, as they are installed at the engine laboratory at Wismar University. The interface is characterized by using the torque curve resolved versus time and angle of rotation in order to accurately describe the highly transient load pattern between the two machines. Both machines are connected with a damped, flexible coupling that is also part of the model.

In this document the current state of the internal combustion engine simulation model is presented. Furthermore, obtained simulation results are compared to engine measurements.

1 Simulation Environment

To simulate the diesel engine, state-of-the-art zero-dimensional models were considered. Although there are many commercial tools available, containing ready-to-run models of internal combustion engines, the decision was made to develop a stand-alone simulation tool to achieve the objectives of the research project. The reasons to do so are listed below:

- exact knowledge of the model structure
- specific adaptation of the models to the conditions of large engines and power generators in single and multi-engine system set-ups with mutual interaction
- free choice of model depth and application complexity of the submodels and the overall system
- interfaces can be easily added into the model e.g. implementation in a heating circuit using engines waste heat

Therefore, MATLAB[®] Simulink[®] was chosen as a flexible and performant simulation tool for the project. This platform allows for adjustable structures and existing modules can also be used as well as in-house developed program codes. By doing so, physical correlations can be programmed in a comprehensive and adaptable manner.

2 Modell Description

To simulate the internal combustion engine a zero-dimensional model is used, which is based on the first

principle of thermodynamics. Thus, the combustion chamber is considered as an unsteady and open system [1]. The energy balance equation 1 derived by crank angle φ in general is described by:

$$\frac{dU}{d\varphi} = -p \frac{dV}{d\varphi} + \frac{dQ_B}{d\varphi} - \frac{dQ_W}{d\varphi} + h_E \frac{dm_E}{d\varphi} - h_A \frac{dm_A}{d\varphi} \quad (1)$$

To solve this balance equation one variable has to be given by measurements, such as cylinder pressure over crank angle or an empirically determined combustion process (heat input due to combustion).

The inner energy inside the combustion chamber is calculated by using the caloric equation of state.

$$dU = m c_v dT \quad (2)$$

Based on [2], equation 2 is derived by time during the simulation which results in:

$$\Delta \dot{U} = m c_v \dot{T} \quad (3)$$

With this approach [2] the first principle of thermodynamics can be phrased as a differential equation of first order as shown below.

$$\dot{T} = \frac{-p \frac{dV(\varphi)}{dt} + \dot{Q}_B - \dot{Q}_W + \dot{H}_E - \dot{H}_A}{m c_v} \quad (4)$$

Polynomic equations depending on the calculated temperature for different air fuel ratios account for a realistic specific heat capacity c_v in order to obtain improved calculation accuracy. The computation of the cylinder pressure results from the ideal gas equation.

$$p = \frac{mRT}{V} \quad (5)$$

Aside from the determination of pressure and temperature it is important to calculate the heat flux \dot{Q}_B induced by the fuel combustion process. This is done by applying a Vibe function [8] [4]. To model a typical diesel-engine combustion process, a superposition of three vibe-functions is used.

With this approach three typical phases named as pre-mixed combustion, main combustion and post combustion can be depicted [4]. Figure 1 exemplary shows the three Vibe functions and the resulting superposition representing the rate of heat release.

As an input parameter for the simulation the combustion process (heat release rate) is generated separately and saved to a 1D Lookup-Table in Simulink[®].

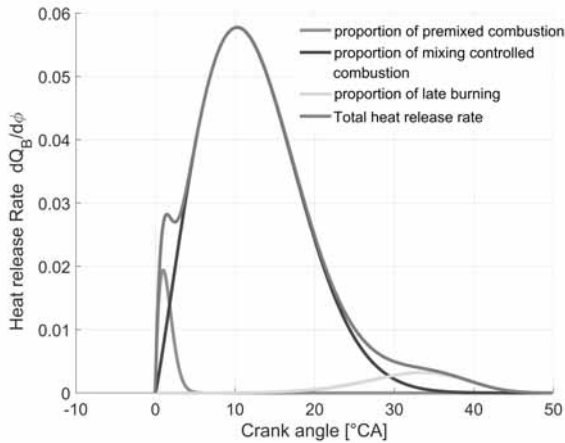


Figure 1: Modeling heat release rate.

By applying Newton's approach, the heat transfer \dot{Q}_W from the hot cylinder gas to the cylinder wall and piston can be estimated.

$$\dot{Q}_W = \alpha A(\varphi) (T_{Gas} - T_{Wall}) \quad (6)$$

In equation 6 $A(\varphi)$ refers to the heat transmitting area which is composed by the cylinder head area, piston head area and the crank angle dependent shell surface of the combustion chamber.

To compute the heat transfer coefficient α equation 7 according to Woschni-Huber [3] was used. This equation does not only account for the high-pressure phase (compression and expansion stroke) but also to the low-pressure part (exhaust and intake stroke).

$$\alpha = 130 d^{-0,2} p^{0,8} T^{-0,53} (C_1 v)^{0,8} \quad (7)$$

The dimensionless constant C_1 is specified by the following parameters:

$$C_1 = 2,28 + 0,308 \frac{v_u}{v_{KM}} \text{ during high-pressure phase}$$

$$C_1 = 6,18 + 0,417 \frac{v_u}{v_{KM}} \text{ during gas exchange}$$

The velocity term v is described in equation 8 according to [3].

$$v = v_{KM} \left[1 + 2 \left(\frac{V_C}{V} \right)^2 p_{mi}^{-0,2} \right] \quad (8)$$

p_{mi} refers to the mean indicated pressure, representing a specific engine load derived from the work performed from a single cycle related to cylinder displacement.

The enthalpy flux \dot{H}_E and \dot{H}_A linked to the gas mass flow through the intake and exhaust valves are calculated by [4]:

$$\dot{H}_E = \dot{m}_E (u_E + R_E T_E) \quad (9)$$

$$\dot{H}_A = \dot{m}_A (u_A + R_A T_A) \quad (10)$$

The index E indicates the condition just in front of the intake valve, whereas the index A characterizes the condition right behind the exhaust valve. The calculation of the specific inner energy is based on substance data out of [3], which are expressed by polynomial equations as a function of temperature for a particular air-fuel ratio. To simulate the mass flow through the valves the equations 11 and 12 are used [3].

$$\dot{m}_E = \mu A_{VE(\varphi)} \frac{p_E}{\sqrt{R T_E}} \sqrt{\frac{2\kappa}{\kappa-1} \left[\left(\frac{p_Z}{p_E} \right)^{\frac{2}{\kappa}} - \left(\frac{p_Z}{p_E} \right)^{\frac{\kappa+1}{\kappa}} \right]} \quad (11)$$

$$\dot{m}_A = \mu A_{VA(\varphi)} \frac{p_Z}{\sqrt{R T_Z}} \sqrt{\frac{2\kappa}{\kappa-1} \left[\left(\frac{p_A}{p_Z} \right)^{\frac{2}{\kappa}} - \left(\frac{p_A}{p_Z} \right)^{\frac{\kappa+1}{\kappa}} \right]} \quad (12)$$

The indication Z stands for conditions inside the cylinder whereas E stands for intake and A indicates the exhaust regarding to the conditions right in front of the in-take valve or right after the exhaust valve.

A_v describes the gap area of the intake or the exhaust valve which changes by time depending on valve lift curves. The flow coefficient μ accounts for the flow resistance inside the valve ducts. It is determined by experiments at cylinder head flow test benches or by CFD-analyses [4]. For the simulation presented in this paper the flow coefficients were adopted depending on relative valve lift from Maurer [1] and Merker & Schwarz [4]. Figure 2 shows the schematic Simulink® code to calculate the energy balance inside the combustion chamber. The simulation starts by specifying initial temperature, engine speed as well as air mass inside the combustion chamber. The piston starting position is at 0°CA (top death center = TDC). The block named "calculation cylinder pressure" calculates the cylinder pressure using equation 5. The current values for temperature and pressure are transferred to the particular subsystems. Integration of the rotational engine speed results in crank angle. Based hereon cylinder volume, valve lift and the gas mass flow are calculated in the subsystems.

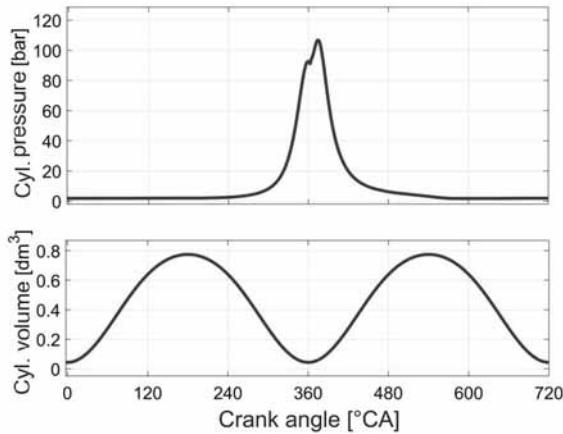


Figure 4: Top: Cylinder pressure curve over one cycle
Bottom: Cylinder volumen over one cycle.

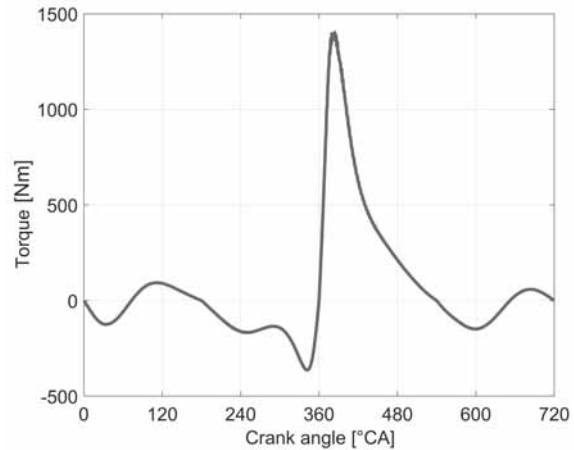


Figure 6: Simulated torque sequence.

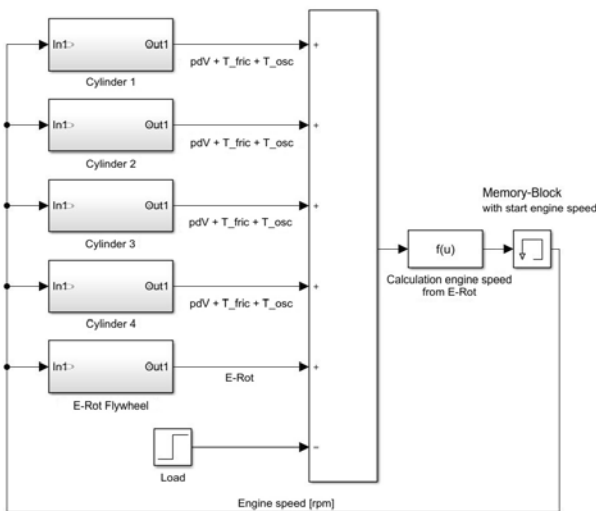


Figure 5: Schematic representation of four-cylinder model.

Subsystems “cylinder 1” to “cylinder 4” calculate the individual torque of each cylinder, considering the oscillating mass and friction losses. The load request (shaft power) of the system is defined by a variable, that can be applied as demanded. The energetic condition of the flywheel is described by using equation 13.

$$E_{Rot} = \frac{1}{2} J \omega^2 \quad (13)$$

Figure 6 shows the simulated torque sequence of a single cylinder during one cycle.

By merging all energy fluxes the rotational energy is attained for each time step. Rearranging equation 13

allows for the calculation of the corresponding engine speed variation.

$$n = \sqrt{\frac{E_{Rot\ new}}{2J\pi^2}} \quad (14)$$

Figure 7 shows the simulated engine speed for a single cycle according to equation 14 for a rated engine speed of 1500 min^{-1} . The engine speed variation of an internal combustion engine may have an impact on the behavior of a coupled electric machine. Due to that the characteristic of the coupling element has to be considered in the simulation. Two equations result from the basic laws of dynamics for rotational motion for each rotating mass (internal combustion engine and electric machine) [6].

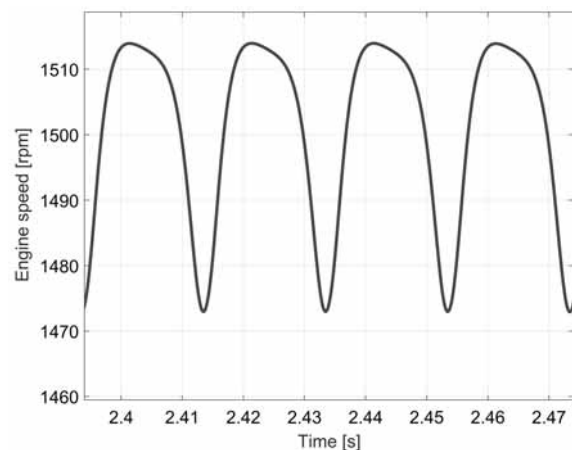


Figure 7: Simulated engine speed sequence of the four-cylinder setup during two engine revolutions.

$$-k_D(\varphi_M - \varphi_G) - d_D(\dot{\varphi}_M - \dot{\varphi}_G) + M = J_M \ddot{\varphi}_M \quad (15)$$

$$k_D(\varphi_M - \varphi_G) + d_D(\dot{\varphi}_M - \dot{\varphi}_G) = J_G \ddot{\varphi}_G \quad (16)$$

The damping torque is expressed by $d_D(\dot{\varphi}_M - \dot{\varphi}_G)$ and $k_D(\varphi_M - \varphi_G)$ represents the torque resulting from a twist of both rotating masses to each other. M stands for the excitation torque which is introduced by the internal combustion engine. Rearranged to the highest derivative, equation 17 is derived.

$$-k_D \left(\frac{1}{J_M} + \frac{1}{J_G} \right) (\varphi_M - \varphi_G) - d_D \left(\frac{1}{J_M} + \frac{1}{J_G} \right) (\dot{\varphi}_M - \dot{\varphi}_G) + \frac{M}{J_M} = (\ddot{\varphi}_M - \ddot{\varphi}_G) \quad (17)$$

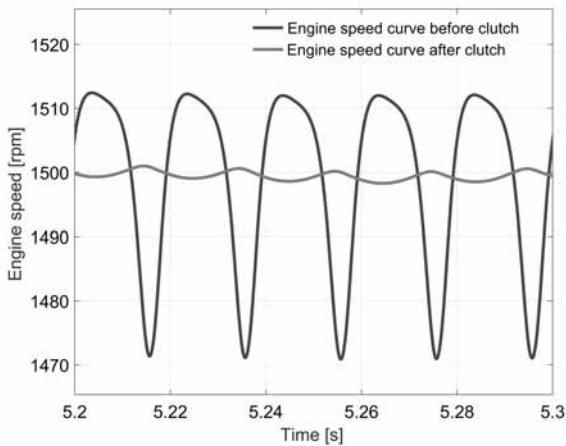


Figure 8: Simulated speed variation of engine and electric machine.

The simulated engine speed curves are shown in figure 8. The blue curve represents the rotational speed that goes into the elastic coupling element and the red curve shows the rotational speed of the electric machine. It can be seen that the engine speed variation of the internal combustion engine is reduced by the elastic coupling element, leading to considerably decreased amplitudes at the electric machine.

3 Model Validation

To verify the simulation model, the calculation results were compared to measurements obtained from the engine laboratory at Wismar University.

A comparison of the cylinder pressures over the course of one cycle at an engine speed of 2000 min^{-1}

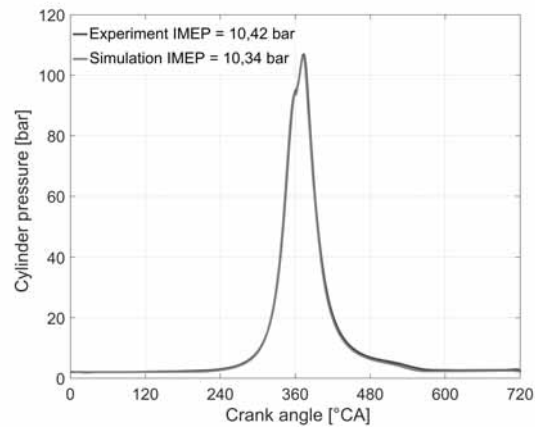


Figure 9: Comparison of measured and simulated cylinder pressure trace of one cylinder.

and a nominal torque of 200 Nm is presented in figure 9. The rate of heat release derived from measurements was used as an input parameter for the simulation. Comparing both pressure traces it can be seen that simulation and measurement agree very well. This fact is an important requirement for an exact description of the torque at the interface of the internal combustion engine and the connected electric generator. A comparison between the mean pressure as an integral value to quantify engine load shows a discrepancy between simulation and measurement below 1%. A similar quality of the simulation results was recognized also at other load points. Therefore, it can be stated that the applicability of the simulation approach is confirmed for stationary operating conditions.

4 Conclusion and Outlook

In the course of the research project SIDYN the operating behavior of an electric power generator in isolated grid mode with dynamic electrical loads is to be predicted based on a modular simulation model. The model should enable the possibility to vary engine and network configurations as well as different load scenarios.

Based on thermodynamic and mechanical relations and specifically developed component submodels for internal combustion engines, a complete model of a four-cylinder four-stroke diesel industrial engine was developed in Simulink®. A comparison between simulation and experiments in steady state load points indicate a very good correlation, which supports the applicability of the chosen simulation approach.

Due to the fact that highly dynamic operating conditions are in the focus of the project a further development of the models and the engine test bed is required. This includes the modelling and experimental observation of the transient behavior of the turbo charger. Furthermore, the influence of heat transfer processes in the intake and exhaust system, as well as the impact of the exhaust gas recirculation on the overall system are to be examined.

Acknowledgement

The results presented here were obtained within the framework of the publicly funded project SIDYN (FKZ: 13FH043PX8). The authors want to thank the BMBF as well as the project partner Caterpillar Motoren GmbH & Co. KG for the provided financial support and expertise.

Nomenclature

$\ddot{\phi}_G$	- angular acceleration, generator sided [rad/s ²]
$\ddot{\phi}_M$	- angular acceleration, engine sided [rad/s ²]
$\dot{\phi}_G$	- angular velocity, generator sided [rad/s]
$\dot{\phi}_M$	- angular velocity, engine sided [rad/s]
$\dot{H}_{E,A}$	- exhaust and intake enthalpy fluxes [J/s]
\dot{m}	- mass flux [kg/s]
\dot{Q}_B	- heat release rate of the combusted fuel [J/s]
\dot{Q}_W	- wall heat flux [W]
κ	- isentropic exponent [-]
μ	- flow coefficient [-]
ω	- angular velocity [s ⁻¹]
ϕ_G	- twist angle, generator sided [rad]
ϕ_M	- twist angle, engine sided [rad]
A	- heat transferring area [m ²]
A_v	- gap area [m ²]
c_v	- specific heat capacity [J/(kg K)]
d	- bore diameter [m]
d_D	- torsional spring stiffness [Nms/rad]
h	- specific enthalpy [J/kg]
J	- inertia moment [kg m ²]

J_G	- generator inertia moment [kg m ²]
J_M	- engine inertia moment [kg m ²]
k_D	- torsional spring stiffness [Nm/rad]
m	- mass [kg]
p	- pressure [Pa]
p_{mi}	- indicated medium pressure [bar]
R	- gas constant [J/(kg K)]
T	- temperature [K]
U	- inner energy [J]
u	- specific inner energy [J/kg]
V	- volume [m ³]
v_{KM}	- mean piston velocity [m/s]
v_u	- swirl velocity [m/s]

References

- [1] Maurer, T. *Einführung in die Realprozessrechnung von Verbrennungsmotoren*, Berlin: Springer-Verlag GmbH, 2020.
- [2] Scherf, H. *Modellbildung und Simulation dynamischer Systeme*, München: Oldenbourg Wissenschaftsverlag, 2010.
- [3] Pischinger, R., Klell, M., Sams, T. *Thermodynamik der Verbrennungskraftmaschine*, 3. Aufl., Wien, New York: Springer-Verlag, 2009.
- [4] Merker, G., Schwarz, C. *Grundlagen Verbrennungsmotor*, 4. Auflage, Wiesbaden: Vieweg + Teuber, 2009.
- [5] Chen, S., Flynn, P. *Development of a Single Cylinder Compression Ignition Research Engine* in SAE Technical Paper 650733, 1965.
- [6] Jäger, H., Mastel, R., Knaebel, M. *Technische Schwingungslehre*, 8. Aufl., Wiesbaden: Springer Vieweg, 2013.
- [7] Mrugowsky, H. *Drehstrommaschinen im Inselbetrieb*, 2. Aufl., Wiesbaden: Springer Vieweg, 2015.
- [8] Vibe, I. *Brennverlauf und Kreisprozess von Verbrennungsmotoren*, VEB Verlag Technik, Berlin, 1970.

Adapted Laboratory for Mobile Robotics Teaching and its Application to Coordinated Control of Robots

David Gallarta Sáenz*, Pablo Álvarez Benito, Javier Rico-Azagra,
Montserrat Gil-Martínez

Control Engineering Research Group, Department of Electrical Engineering, University of La Rioja, San José de Calasanz, 31, 26004 Logroño, Spain; *david.gallarta@unirioja.es

SNE 32(2), 2022, 63-68, DOI: 10.11128/sne.32.tn.10602
Received: 2021-02-10 (selected EUROSIM 2019 Postconf.
Publication; Revised: 2022-02-09; Accepted: 2022-02-15
SNE - Simulation Notes Europe, ARGESIM Publisher Vienna
ISSN Print 2305-9974, Online 2306-0271, www.sne-journal.org

Abstract. This paper presents a teaching laboratory especially suitable for practical work with mobile robotic systems. The laboratory is composed of a set of low-cost robots and a vision-based data capture system used to localise such robots with precision. All the generated information is centralised on a computer that acts as a link between the different elements. MATLAB-Simulink, a well-known programming environment, is used for information processing, and it also achieves maximum compatibility with the dynamic control tasks of the robots. To demonstrate the usefulness of the developed software and hardware infrastructure that comprise the laboratory, a coordinated control system involving several robots and using Lloyd's algorithm is presented.

Introduction

Nowadays, there is a growing interest in the use of robotic systems that replace, totally or partially, the intervention of human operators, which means that this type of technology has reached a high level of maturity. Traditionally, these solutions were focused on the use of fixed-base manipulators. However, in recent years there has been a fast growth of solutions based on the use of ground mobile robots, which introduce new challenges that future engineers must face.

The problems of estimation of attitude [1] and position [2, 3], the capture of information, the coordination of vehicles or the communication between fleets, represent technological challenges that will be essential for the professional development in the future.

Multi-robot systems [4-6] open a new field of study in mobile robotics, since they allow the optimization of multitude of applications and the development of new ones, helping to achieve objectives that are difficult to reach for a single robot. The control of multi-robot systems [7-9] is an area of science that has a great potential for development and that can involve important progress in mobile robotics in the coming years.

One of the main advantages of these systems is their versatility. A group of simple robots can carry out different types of more difficult tasks than a complex single robot could achieve. A multi-robot system presents great flexibility in terms of the number of robots that compose it and the different functions that each one can perform. This makes it possible to work in larger areas and allows to achieve the objectives in a more efficient way.

Another important attribute of these systems is redundancy: if a failure occurs in one of the agents, there is still a certain number of units that can continue carrying out the programmed tasks. There are mainly two types of coordinated control: formation control [10, 11] and coverage control [12]. In the first case, the goal is to make the robots position themselves in a certain way with respect to the others in order to accomplish a coordinated movement maintaining that formation. This allows the performance of different tasks at the same time. The second one consists in covering a certain area, distributing the space between several robots according to the requirements of each situation. This facilitates the possibility of covering large areas and reducing the necessary time to achieve the desired objectives.

In parallel with the arrival of these systems to our everyday life, the importance of teaching in this kind of technology has experienced a remarkable growth in recent years, increasing its relevance in the study programmes of the European Higher Education Area (EHEA).

As in other disciplines, laboratory practices are a fundamental element for acquiring the necessary competences. Nowadays, most of the practices about systems that use mobile robots in teaching are carried out through simulations, which does not imply a real contact for the student with situations that can be found beyond the classrooms. In addition, this type of tools generates a lower level of motivation in the student. The use of simulation tools instead of real systems is caused by the difficulty of having adapted and versatile laboratories, due to space limitations, economic issues or complexity in the implementation of solutions, which often exceeds the available time in a regular practice session.

In this paper, the development of a laboratory focused on the study of mobile robotic systems is described, together with its application to coordinated control of robots. The laboratory has the ideal requirements for the students to put their knowledge into practice in an environment that promotes learning through manipulation. It is a wide space, which has the necessary security conditions, as well as the functionalities of a 21st century technological context. This laboratory is designed to experiment and check the concepts used in robotic systems. Specifically, it can be used for practices focused on the modelling and control of aerial or ground robots, for the development of localisation and navigation systems, for the study of problems generated by odometry and for the coordinated control of flocks of mobile robots. Another advantage of this laboratory is that it can be built with a low budget and allows the possibility of working with MATLAB-Simulink, a familiar environment for the students, a fact that minimise their learning curve.

The paper is divided into four sections. The second one describes the laboratory, its elements and way of operation. The third section presents its application to coordinated control of mobile robots. Finally, the last one contains the conclusions.

1 Teaching Laboratory

The developed laboratory has mainly four elements: the working area, the vision-based data capture system [13], the used mobile robots and the software architecture that supports the system. These elements are described below.

1.1 Working Area and Vision-Based Data Capture System

The available working area has an approximate extension of $7\text{ m} \times 7\text{ m}$, enough space to carry out tests with ground robots and small multi-rotor UAVs (Unmanned Aerial

Vehicle) [14]. On the edge of this enclosure there are eight Flex 3 cameras (see Fig. 1), commercialised by OptiTrack. These cameras are attached to a metal tube of 1 m long and 5 cm diameter, with a square base fixed to the ceiling by four screws. The support is complemented with a plastic clamp that has a ball joint on which the camera is held. This clamp allows the adjustment of the orientation and height along the tube.

The main application for which the eight Flex 3 cameras are installed is the tracking of ground robots [15] and drones [16]. The cameras are located according to the scheme shown in Figure 1. Its strategic placement tries to cover the largest possible area, since it must be taken into account that a point must be seen by at least three cameras. Once configured and calibrated, the system works with errors of estimation of position and orientation lower than 0.2 mm and 0.1° . Following this configuration, a capture area of $5\text{ m} \times 5\text{ m}$ is available.

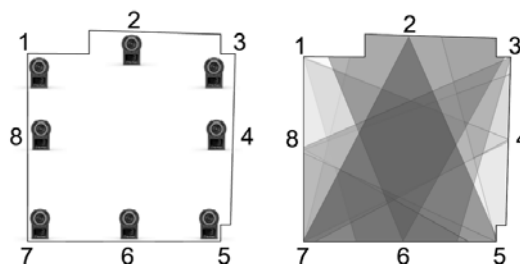


Figure 1: Layout of the cameras in the laboratory.

In order for the robots to be recognised by the cameras, they must have reflective markers, provided by OptiTrack, randomly distributed over their structure. Figure 2 shows the placement of markers in a LEGO Mindstorms EV3 and its representation as a rigid body in Motive, Software provided by OptiTrack, used to process data captured by the cameras.

Finally, it can be noticed that a gray carpet has been placed on the floor of the working area (see Fig. 2), which has several functions, such as reducing the reflectance of the floor, preventing slipping of the wheels of mobile robots and buffering the impact in the case that a UAV crashes into the floor.

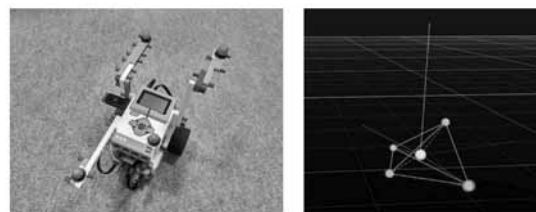


Figure 2: Markers in a LEGO EV3 robot and its representation in Motive.

1.2 Mobile Robots

In the laboratory, it can be used any type of mobile robot capable of communicating with Simulink. Mainly, multi-rotor UAVs are used, in which the installed flight controller belongs to the APM family [17], and ground mobile robots based on the LEGO Mindstorms EV3 platform [18, 19]. In this paper, the described application is for this last robot.

The LEGO Mindstorms EV3 is a kit focused on education, traditionally used in secondary education courses to get a first glimpse of robotics [20, 21]. However, the existence of a Simulink library of specific blocks for this family of robots, makes it possible to experiment with techniques used in industrial robots [22], so this robot is an exceptional work tool for students at university level. In addition, its low cost makes it accessible to schools and universities, where sometimes the available budget does not allow to obtain other types of useful robots for teaching due to their high price. An important feature of this robot is that, since it is assembled from scratch with different pieces, it permits to get different configurations according to the desired use. Thanks to the multiple included accessories (colour sensor, touch sensor, ultrasonic sensor...), it is possible to get to know techniques used on a larger scale in the industry. This versatility also means that there are not many difficulties when it comes to repairing the robot, since it is enough to replace the damaged part. This, added to the facility to find spare parts, makes maintenance easy.

Despite the advantages mentioned above, the LEGO Mindstorms EV3 platform is not defect-free. Its main problems are the low power of its motors and the low precision of the built-in sensors, which give rise to important errors when estimating the state of the vehicle using only odometry-based techniques. In this case, the use of the vision-based data capture system solves this problem.

1.3 Software Architecture and Communication System

The communication system used to send and receive information between the different elements that compose the system is shown in Figure 3. In this figure, it can be verified that all the elements are in a type C VLAN (Virtual Local Area Network) generated with a router. It connects the LEGO EV3 robots and the PC on which the tests are executed through Wi-Fi. It can be used an Ethernet link for the PC if desired.

It is recommended to connect only the elements used in the laboratory to the mentioned network, in order to reduce the data traffic and avoid packet losses. Note that the transmission of packets between the PC and the EV3 robots is carried out using the UDP protocol. As for the coding of the network, it can be open or it can be used a WPA encryption, the only one supported by the brick EV3.

As illustrated in Figure 3, the information from the cameras is received by the PC using two OptiHub hubs, each one of which includes four cameras connected via USB. At the same time, the hubs are connected to each other and to the PC for the synchronization of the captured data. The Motive software automatically manages the information and estimates the position of the bodies. The data generated by Motive is internally broadcasted using the VLAN. It can be noticed how the generated information is centralised in real time on the PC. In this way, the PC acts as a sender and as a receiver, transmitting the necessary information to each element of the system.

Regarding the programming of the different devices, there are multiple alternatives, depending on whether the system works with a single robot or with several robots and if a centralised or distributed architecture is desired. In the most general case, that uses several mobile robots, $n+1$ Simulink models must be developed, one for each of the n robots that work in the application and one last model that coordinates the information, which is executed on the PC.

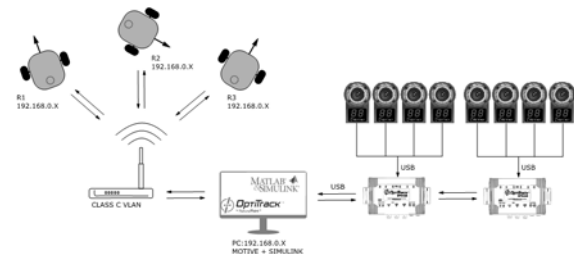


Figure 3: Communication between the different elements in the laboratory.

As previously mentioned, the Simulink model that is executed in each one of the robots exchanges data with the PC using the UDP protocol. For example, the positioning references can be sent from the PC to the robots as coordinates, indicating the point to which they should move, and the robots can send the data generated by their sensors to the PC to close the control loop. The Simulink model executed on the PC can also receive the data collected by Motive, which can be used in monitoring tasks or in the development of control strategies.

2 Application of the Laboratory to Coverage Control

In this section, a solution to the problem of coverage with three LEGO Mindstorms EV3 robots is presented. The main objective is to illustrate how the laboratory works, its possibilities and the results obtained.

2.1 Differential Drive Robot and its Control as an Elemental Unit

In this case, the EV3 robots are configured to work as differential drive robots, which means using two wheels located on a common axis and each one coupled to its own motor and controlled independently. This kind of robot is the most used in laboratories because of the simplicity of its design and its manoeuvrability. Despite its simplicity, this configuration allows to develop numerous tasks, which makes this robot a great tool for student learning.

In order to perform the control of the differential drive robot, it is necessary to implement a hierarchical control structure with several levels. In the lowest level, the speed control of each one of the wheels is placed. For this control, the student must carry out the experimental identification of the motor and close the feedback loop designing the appropriate controller. In a second hierarchical level, the control loop responsible for the movement of the robot is located. The aim of this control loop is to adjust the linear and angular speed applied to the robot so that it reaches the desired position. To achieve this, two control loops are combined: one of them includes the speed controller for the longitudinal dynamics and the other one contains the direction controller for the lateral dynamics. To close these control loops, odometry-based techniques or the information generated by the cameras of the OptiTrack system can be used. Figure 4 shows the Simulink diagram used in the proposed application, which runs on the three used robots.

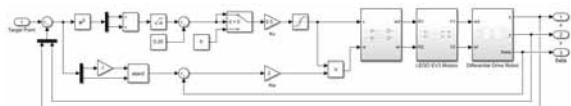


Figure 4: Simulink model implemented in the EV3 robots.

2.2 Coverage Control Algorithm

The implemented coverage control attempts to achieve that the three robots used in the experiment cover a certain area in an efficient manner. To that end, this area is divided into as many parts as robots are used, and the resultant regions are meant to have a similar size.

The used technique is based on Lloyd's algorithm [9], an iterative algorithm that seeks to find a centroidal Voronoi tessellation [23] for a set of points within a certain area. A centroidal Voronoi tessellation is a special type of Voronoi diagram in which the point that generates each one of the cells matches its centroid, obtaining a uniform distribution of the cells. During each iteration, Lloyd's algorithm generates the Voronoi diagram of the given set of points, calculates the centroid of each one of the resulting cells and moves each point towards the centroid of its corresponding cell to generate a new Voronoi diagram. The algorithm is repeated until reaching a centroidal Voronoi tessellation.

This algorithm presents an important feature that makes its implementation very simple: there is no possibility of collisions between robots. The reason for this situation is that the reference point that each robot has to reach is always within its own cell, so that the trajectories of the robots do not bump into each other at any time.

The presented algorithm is implemented in Simulink, taking as input points the positions of each robot. The output points are the coordinates to which each robot must move.

2.3 Results

The obtained results are illustrated below. The initial and final positions of the robots are shown in Figure 5, both in reality and in the reconstruction created by Motive.

In the first experiment, the internal control loop of each one of the robots is closed using the information generated by their encoders. This experiment is carried out in order to illustrate the problems related to the encoders, since they are not a reliable positioning system, in contrast to the vision-based data capture system available in the laboratory.

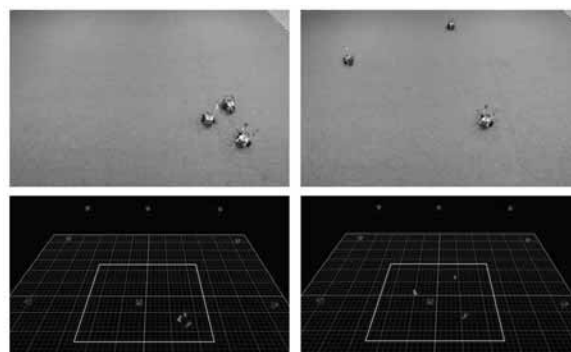


Figure 5: Initial (left) and final (right) position of the robots.

As it is shown in Figure 6, each one of the robots has moved in search of its consecutive reference points (black colour), assigned by the coverage control algorithm. If a thorough analysis is not carried out, it may seem that the robots have achieved their objective. However, the distortion produced by an erroneous estimation of the position of the robots due to the low accuracy of their encoders, which is evident in the curves (see Figure 6 down), leads to an inappropriate coverage.

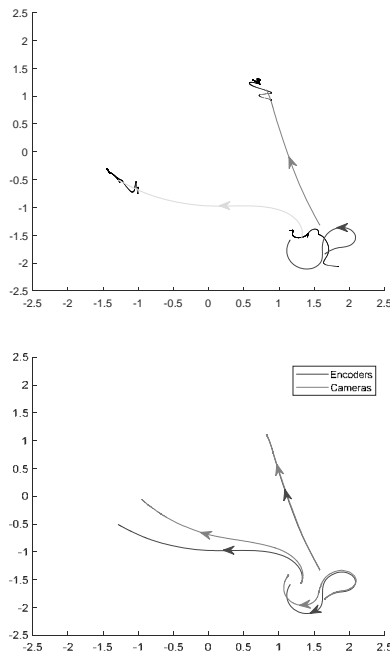


Figure 6: Described trajectory by each robot until reaching its final position (up). Comparison between the trajectories estimated by the encoders and the real trajectories captured by the cameras (down).

As it can be seen in Figure 7 (right), the cells assigned to each robot have different sizes. The best example is the cell occupied by the robot in the lower right corner (blue colour), that is significantly smaller than the rest.

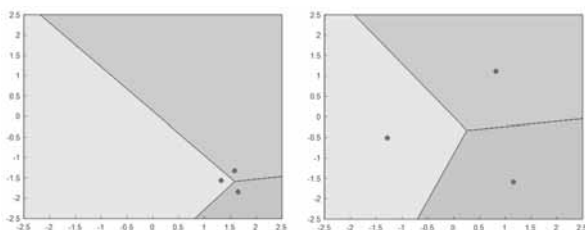


Figure 7: Initial and final distribution of the cells for each robot.

In the second experiment, the test described above is repeated, but in this case, using as feedback the current positions obtained with the vision-based data capture system. At the end of the test, a greater uniformity in the size of the cells can be appreciated (see Figure 8), since the coverage algorithm works more accurately. This experiment shows the importance of using a system that allows to determine with precision the position of the mobile robots. This problem would be more serious if the accumulation of errors in the estimation of the position of the robots involves collisions between them.

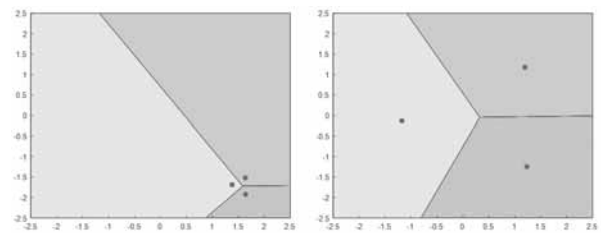


Figure 8: Initial and final distribution of the cells for each robot when the information captured by the cameras is used for the feedback.

Although the areas of the cells in the final situation of this second experiment are more compensated than in the first one, the space is not perfectly distributed. This is because the robots maintain a safety distance of 25 cm to the target point to ensure a better behaviour, so they never reach that point. This situation exists in both the first and the second experiment. It can be observed in Fig. 6 (left) that none of the robots finishes its trajectory at the end of the black line (reference points). In the case of the robot located on the left, that distance would reduce the size of its cell to the benefit of the other two. As the working area is only 5 m × 5 m, the difference between the final size of the cells is quite noticeable. However, considering that this type of systems is usually used in large areas, this difference would be insignificant.

3 Conclusions

It has been presented a laboratory that may be of interest for teaching systems that use mobile robotics. Its main advantages are its simplicity, low cost and reduced learning curve. Having all the information generated by the system in a single software (MATLAB-Simulink) brings numerous benefits for the student, who does not have to face a new development environment.

The proposed application example shows the advantages of the teaching laboratory.

In the implemented application, a coverage control is carried out with three differential drive robots built with the LEGO Mindstorms EV3 platform. This experiment evidences the problems generated when the control loops of the robots are closed using techniques based on odometry. In addition, it is illustrated how these problems can be solved using the vision-based data capture system built in the laboratory.

Acknowledgements

The authors are grateful for the assistance provided by the Government of La Rioja through the I+D ADER 2017-I-DD-00035 project and by the University of La Rioja through the Help to Research Groups REGI 2018/42.

References

- [1] Rico-Azagra J, Gil-Martínez M, Rico-Azagra R, Maisterra P. Low-cost attitude estimation for a ground vehicle. *Robot 2015: Second Iberian Robotics Conference, Advances in Intelligent Systems and Computing*, 121-132 (2016).
- [2] Gonzalez J, Stentz, A, Ollero A: A Mobile Robot Iconic Position Estimator using a Radial Laser Scanner. *Intelligent & Robotic Systems* 13, 161-179 (1995).
- [3] González J, Ollero A. Estimación de la Posición de un Robot Móvil. *Informática y automática: revista de la Asociación Española de Informática y Automática* 29(4), 3-18 (1996).
- [4] Badran M, Khan R, Fauziah S, Zainal Z. Collaboration in multi-robot systems. *ARPN Journal of Engineering and Applied Sciences* 10(22), 17225-17231 (2015).
- [5] Parker L.E. Current Research in Multi-Robot Systems. *Journal of Artificial Life and Robotics* 7(1-2), 1-5(2003).
- [6] Gautam A, Mohan S. A Review of Research in Multi-Robot Systems. *IEEE 7th International Conference on Industrial and Information Systems*, (2012).
- [7] Yan Z, Jouandeau N, Ali Cherif A. A Survey and Analysis of Multi-Robot Coordination. *International Journal of Advanced Robotic Systems* 10(399), 1-18, (2013).
- [8] Bullo F, Cortés J, Martínez S. Chapter 5: Deployment. In: Princeton University Press, Princeton and Oxford. *Distributed Control of Robotic Networks, A Mathematical Approach to Motion Coordination Algorithms*, pp. 214–242 (2009).
- [9] Cortés J, Egerstedt M. Coordinated Control of Multi-Robot Systems: A Survey. *SICE Journal of Control, Measurement, and System Integration* 10(6), 495–503 (2017).
- [10] Mastellone S, Stipanović D, Spong M. Remote Formation Control and Collision Avoidance for Multi-Agent Non-holonomic Systems. *Proc. of the IEEE International Conference on Robotics and Automation*, pp. 1062-1067. Roma, Italy, April 2007.
- [11] Balch T, Arkin R. Behavior-based Formation Control for Multi-robot Teams. *IEEE Transactions on robotics and automation* 14(8), (2001).
- [12] Ranjbar-Sahraei B, Weiss G, Nakisaei A. A Multi-Robot Coverage Approach based on Stigmergic Communication. *German Conference on Multiagent System Technologies* 7598, 126-138 (2012).
- [13] Atiya S, Hager G. D.: Real-Time Vision-Based Robot Localization. *IEEE Transactions on Robotics and Automation* 9(6), (1993).
- [14] Gallarta D, Rico-Azagra J, Nájera S, Gil-Martínez M. Laboratorio para el desarrollo de sistemas de navegación y control para UAVs multirrotor. *Proceedings of the XXXIX Jornadas de Automática*, pp. 613-620. Badajoz, Spain, September 2018.
- [15] Vincze M, Prenninger JP, Gander H. A Laser Tracking System to Measure Position and Orientation of Robot End Effectors Under Motion. *The International Journal of Robotics Research* 13(4), 305-314 (1994).
- [16] Mueller M, Smith N, Ghanem B. A Benchmark and Simulator for UAV Tracking. *Proceedings of the 14th European Conference on Computer Vision*, pp. 445-461. Amsterdam, The Netherlands, October 2016.
- [17] MathWorks Website, www.mathworks.com/matlabcentral/fileexchange/39037-apm2-simulink-blockset, last accessed 2019/06/11.
- [18] Korkmaz Ö. The Effect of Scratch- and Lego Mindstorms Ev3-Based Programming Activities on Academic Achievement, Problem-Solving Skills and Logical-Mathematical Thinking Skills of Students. *Malaysian Online Journal of Educational Sciences* 4(3), 73-88 (2016).
- [19] Danahy E, Wang E, Brockman J, Carberry A, Shapiro A, Rogers C. LEGO-based Robotics in Higher Education: 15 Years of Student Creativity. *International Journal of Advanced Robotic Systems* 11(27), (2014).
- [20] Cerezo F, Sastrón F. Laboratorios Virtuales y Docencia de la Automática en la Formación Tecnológica de Base de Alumnos Preuniversitarios. *Revista Iberoamericana de Automática e Informática industrial* 12, 419–431 (2015).
- [21] Ospennikova E, Ershov M, Iljin I. Educational Robotics as an Innovative Educational Technology. *Procedia - Social and Behavioral Sciences* 214, 18–26 (2015).
- [22] Koc AB, Liu B. Demonstrating Tractor Rollover Stability Using Lego Mindstorms and Smartphones. *Journal of Agricultural Systems, Technology, and Management* 24, 1-11 (2013).
- [23] Du Q, Faber V, Gunzburger M. Centroidal Voronoi Tessellations: Applications and Algorithms. *SIAM Review* 41(4), 637-676 (1999).

Pulse Wave Analysis by Quantified Reconstructed Attractors

Carina Hörandtner^{1,2}, Martin Bachler¹, Siegfried Wassertheurer¹, Felix Breitenecker², Christopher C. Mayer^{1*}

¹Biomedical Systems, Center for Health & Bioresources, AIT Austrian Institute of Technology, Giefinggasse 4, 1210 Vienna, Austria; *christopher.mayer@ait.ac.at

²Institute of Analysis and Scientific Computing, Vienna University of Technology, Wiedner Hauptstraße 8–10, 1040 Vienna, Austria

SNE 32(2), 2022, 69-78, DOI: 10.11128/sne.32.tn.10603
Received: 2021-07-21, Revised: 2021-10-10;
Accepted: 2021-12-15
SNE - Simulation Notes Europe, ARGESIM Publisher Vienna,
ISSN Print 2305-9974, Online 2306-0271, www.sne-journal.org

Abstract. Direct time domain analysis is a classical method for pulse wave analysis. Attractor reconstruction is a new and alternative way to analyse the morphology of a pulse wave. The novel approach plots the pulse wave data as overlapping loops in the three-dimensional phase space and, subsequently, projects the trajectories onto a plane generating two-dimensional attractors. This paper presents methods that automatically quantify these attractors. At first, a short overview of the attractor reconstruction technique is provided. After pre-processing of the pulse waveform data, the attractor is generated and edited by a median filter to remove remaining artefacts that can distort the quantification process. The developed algorithm is based on image processing and extracts attractor features such as the angle of rotation, the angle between the arm fragments, shape, height, lengths and width of the attractor. Finally, visual examination evaluates the performance of the feature extraction technique revealing that the majority of the generated attractors are correctly quantified. However, it also shows that remaining outliers and metrological discrepancies have a negative impact on the results.

Introduction

Pulse waveform analysis (PWA) plays an important role in detection and prevention of cardiovascular diseases [1, 2, 3]. Although many approaches of current pulse

waveform analysis have proven to be useful tools in early risk assessment, some downsides are worth mentioning. The first issue of PWA is that not all available data is used [4]. Proper inspection and interpretation of a large quantity of data points is an almost impossible or costly task; thus, only average values such as the average interval length or the average maximum and minimum peak values (systolic and diastolic pressure) are examined, which, however, might ignore useful information on the pulse wave's shape. Furthermore, it is difficult to detect any changes in shape and variability of the pulse waveform when it is plotted against a time axis and viewed over a long period of time [4]. Consequently, the pulse waveform can only be quantified appropriately if a short time window is selected which again just focuses on a small number of sampled data. Another issue is baseline wander and noise which can interfere with the signal and may prevent proper quantification [4]. Therefore, baseline wander is removed in some studies [5]. However, editing the original signal might exclude important information from the data.

To overcome these issues, Nandi et al. [4] and Aston et al. [6] developed a new way to visualize and quantify cardiovascular waveform data. The introduced attractor reconstruction method uses every single data point of the sampled waveform, neglects baseline wander and represents pulse waveform signals in a compact three-dimensional phase space which may provide deeper understanding of physiological changes within the cardiovascular system.

In this paper, the method of reconstructing attractors from pulse waveform data is used and further developed [4, 6]. The goal is to present a newly implemented algorithm for the automatic quantification of these attractors.

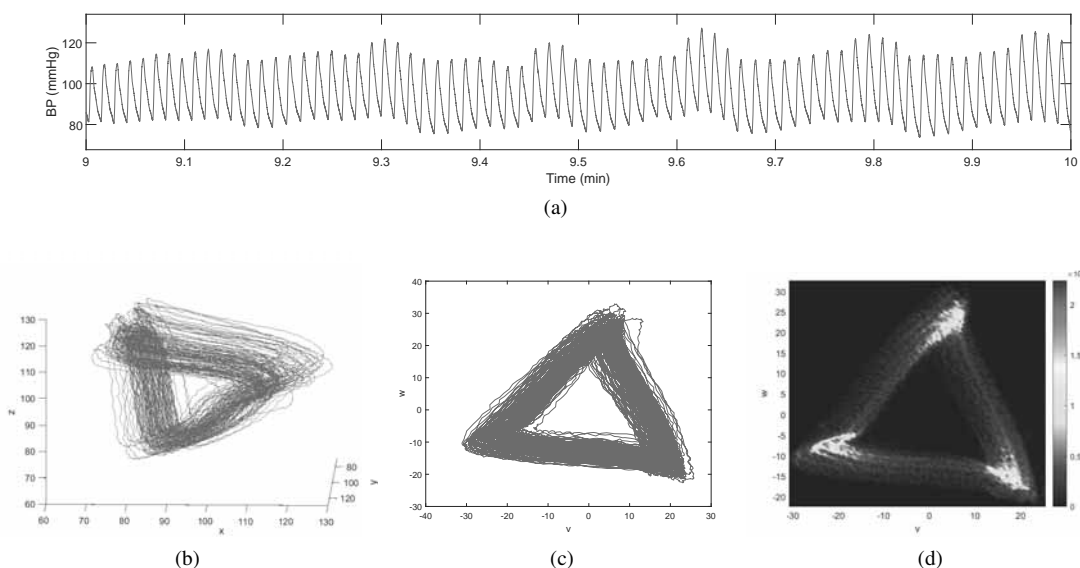


Figure 1: Attractor reconstruction using delay coordinates. (a) 60 second sample of pulse waveform data, (b) reconstructed attractor in the three dimensional phase space, (c) projection of the attractor onto a plane orthogonal to the vector (1, 1, 1), (d) density plot of the two dimensional attractor.

1 Attractor Reconstruction

The attractor reconstruction method [4, 6] uses Takens’ delay coordinates [7] to reconstruct all data points of a cardiovascular waveform (see figure 1a) as a compact object in the three-dimensional phase space. The time delay $\tau > 0$ is chosen to be one third of the average cycle length [6]. Let $x(t)$ be the given signal. Then the two other coordinates are calculated as

$$y(t) = x(t - \tau), \quad z(t) = x(t - 2\tau). \quad (1)$$

The data can then be plotted in the three-dimensional phase space as $(x(t), y(t), z(t))$ for all t in a given time window, resulting in numerous overlapping loops, the so-called attractor (see figure 1b). In order to remove the effect of baseline wander, the three-dimensional attractor is projected onto a plane orthogonal to the vector (1, 1, 1). The resulting new set of coordinates (u, v, w) is defined as

$$u = \frac{1}{3}(x+y+z), \quad v = \frac{1}{\sqrt{6}}(x+y-2z), \quad z = \frac{1}{\sqrt{2}}(x-y). \quad (2)$$

The two-dimensional attractor in the (v, w) plane (see figure 1c) consists of many overlapping lines with little detail visible. To provide more information on the

attractor and to enable the quantification and extraction of attractor features, a density is constructed (see figure 1d).

2 Methodology and Implementation

In order to detect changes in shape and variability of a cardiovascular waveform, the attractors have to be quantified in an automatic manner. In this paper, a method based on pulse waveform data acquired through photoplethysmography at the fingertip is presented. The data sets originate from a pilot study [8] that investigates the impact of device-guided breathing on thirty patients with treated hypertension. Each data set is fifteen minutes long. To generate a sound attractor which provides as much information as necessary, signal segments of 100 seconds are chosen [4]. All parameters and thresholds used in the described algorithms are empirically chosen for the data set at hand, if not stated otherwise. All implementations are done in MATLAB 2019b (The MathWorks, Inc, Natick, MA).

2.1 Preprocessing and Filtering

Preprocessing. Since the attractor reconstruction method uses every single data point, hardly any data

preprocessing is needed, which makes it more resistant to bias introduction [4]. Nevertheless, non-physiological artefacts should be removed because outliers can possibly distort the extraction of attractor features. In this paper, non-physiological outliers are detected in sections with a length of four seconds. To detect possible artefacts, the minima and maxima and their differences are determined and the built-in MATLAB function *isoutlier* is used to discover outliers in the set of the maximum-to-minimum differences. An outlier is characterized by an element that is more than three scaled Median Absolute Deviation (MAD) defined as

$$\text{MAD} = -\frac{1}{\sqrt{2} \cdot \text{erfcinv}(\frac{3}{2})} \cdot \text{median}(|x - \text{median}(x)|), \quad (3)$$

from the median [9]. Here x denotes the vector of the maximum-to-minimum differences and *erfcinv* is the inverse complementary error function. Afterwards, all segments containing artefacts are removed.

Attractor Reconstruction. After removing outliers from the signal, the attractor is generated according to the steps explained in section 1. The density is constructed by using a square grid of 100×100 boxes and the volume is normalized to be one, generating a 100×100 density matrix N .

Median Filter. In order to remove remaining noise which might distort later calculations, a two-dimensional median filter is applied to the density plot of the attractor [10]. For each pixel in the 100×100 density plot a 3×3 neighbourhood is chosen which proves to be suitable for the data used in this paper. The pixel located in the center of the neighbourhood is set to the median value of the pixels within the kernel frame

$$N'(x,y) = \text{median}(N(x+i,y+j), (i,j) \in \{-1,0,1\}). \quad (4)$$

Entries that are smaller than half the size of the median filter kernel value are removed by the filter [10]. In order to eliminate artefacts (see figure 2a) but still preserve the basic structure of the attractor, all values of N , which have not been removed by the median filter, stay the same and the others are set to zero:

$$N(x,y) = \begin{cases} 0, & \text{if } N'(x,y) = 0, \\ N(x,y), & \text{if } N'(x,y) \neq 0. \end{cases} \quad (5)$$

Figure 2b shows an attractor after applying the two-dimensional median filter.

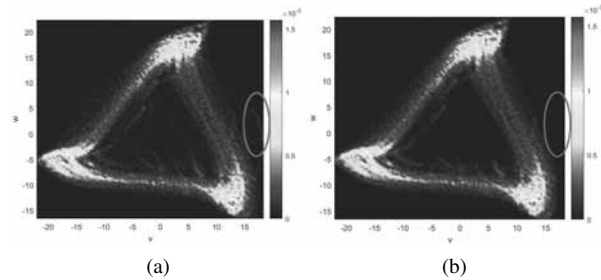


Figure 2: Application of a two-dimensional median filter with a 3×3 neighbourhood. (a) Unfiltered attractor with artefacts characterized by chaotic lines in the middle and on the right side (exemplarily circled in red), (b) filtered attractor.

2.2 Rotation of the Attractor

After reconstruction and filtering, the attractor has to be rotated. This provides information on the downstroke of the attractor [4, 6] and simplifies further calculations. Figure 3a depicts an attractor in its original form with blurred edges which makes feasible computation more difficult. To overcome this issue and properly detect edges and eventually straight lines, the density matrix N is converted into a binary image using techniques from image processing. In the following, the used MATLAB functions are provided:

```
N = double(N >= (m * max(N(:)))) ;
BW = edge(N, 'Prewitt', 'horizontal') ;
[H, T, R] = hough(BW) ;
P = houghpeaks(H, 2, 'threshold', ...
ceil(0.3 * max(H(:)))) ;
lines = houghlines(BW, T, R, P, ...
'FillGap', 15, 'MinLength', len) ;
```

In order to neglect remaining outliers, all entries of the density matrix N that are greater than $m = 1\%$ of its maximum entry are set to 1 and all others are set to 0. The built-in MATLAB function *edge* finds edges in the binary image that are approximately horizontal (see figure 3b). To detect lines and their position and angle in the image, Hough transform [11] is

used. The function *hough* is designed to detect lines in a binary image BW , where the parameter representation $\rho = x \cos(\theta) + y \sin(\theta)$ of a line is used. Here ρ denotes the perpendicular distance from the origin to the line and θ the angle between the x-axis and this perpendicular vector. The function also returns the parameter space matrix H , whose rows and columns correspond to ρ and θ values, respectively [12]. Any point within the image is mapped to a sinusoidal curve in the Hough space and if two points are located on the same line segment, the two generated curves in the Hough space overlap [13]. The function *houghpeaks* locates peaks, i.e. overlapping sinusoidal curves, in the Hough transform matrix H and returns the column coordinates of the peaks. In this paper, a maximum of two line segments in the image space are considered and the minimum value recognized as a peak is 30% of the maximum value of H . The function *houghlines* extracts the line segments in the image BW (see figure 3c) and returns their angle and position, whereas only lines with a minimum length of $len = 30$ pixels and an angle of 15 degrees above or below the horizontal line are considered. This ensures that only the lower and thus longer edge of the attractor arm is approximated. If no line matches these conditions, the angle of rotation θ is set to NaN , otherwise θ is defined as the mean value of the feasible angles. Afterwards the attractor is rotated in an anticlockwise direction by $\theta \neq NaN$ in the (v, w) plane (see figure 3d):

$$\begin{bmatrix} v_{rot} \\ w_{rot} \end{bmatrix} = \mathbf{R} \cdot \begin{bmatrix} v \\ w \end{bmatrix}, \quad \mathbf{R} = \begin{bmatrix} \cos(\theta) & -\sin(\theta) \\ \sin(\theta) & \cos(\theta) \end{bmatrix} \quad (6)$$

2.3 Angle between Attractor Arms

Depending on the used signal, attractors can vary in shape. In this study, some attractors have noticeable bent sides, so the next features to be calculated are the angles between the attractor arms β (see figure 4). Because only the shape of the attractor and not the density of different regions is of relevance, the density matrix N is converted into a binary matrix using only values that are greater than 5% of its maximum value; others are set to 0. Investigations of the generated attractors have shown that the bend of the arm is usually located in the south east quarter of the attractor. Therefore, a search window is set to this area of the density matrix. The angle β is defined as $\beta = 180^\circ - \alpha$, thus, the an-

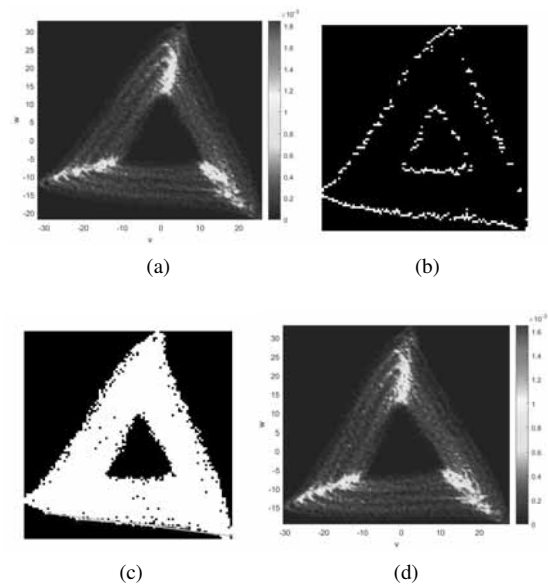


Figure 3: Rotation of the attractor. (a) Original attractor, (b) edge detection in binary image, (c) line detection via Hough transform, (d) rotated attractor.

gle α has to be determined first. For this purpose, the attractor is gradually rotated in an anticlockwise direction (see formular 6). In this study, an angle between 0 and 60 degrees and a step size of about $\frac{\pi}{300}$ degrees are used. After each step of the rotation the row sum within the search window and the difference between adjacent values of this row sum vector are calculated. The more horizontal the right fragment of the lower attractor arm gets, the higher is the negative difference in the row sum vector. In each step the minimum value of the vector is determined and stored. After the rotation is completed, i.e. 60 degrees are reached, the minimum value in the vector of minima and its index i^* are calculated. This yields the sought angle $\alpha^* = \alpha(i^*)$ and, consequently, $\beta = 180^\circ - \alpha^*$. Due to the choice of the time delay τ , the attractor has arbitrary 3-fold rotational symmetry [6]. Thus, the angles between the arm fragments of the two remaining sides are calculated similarly after rotating the attractor by 120 and 240 degrees, respectively, to improve accuracy.

The developed algorithm automatically categorizes the attractors in two different shapes: triangular attractors (see figure 5a) and attractors with bent sides (see figure 5b). An attractor is said to be triangular in shape, if at least two of the three angles between the attractor arms are greater than or equal to 165 degrees. Other-

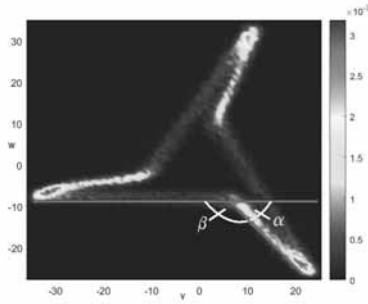


Figure 4: Angle between attractor arm fragments.

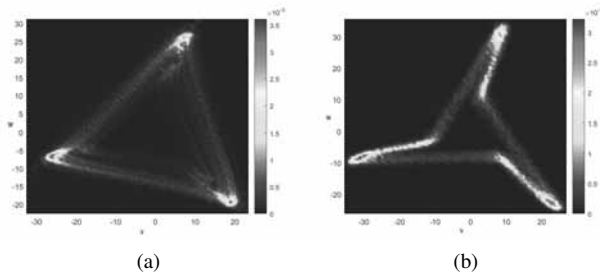


Figure 5: Different shapes. (a) Triangular attractor, (b) attractor with bent sides.

wise, its shape is understood as bent. This classification is necessary to prevent falsely calculated measurements in the further feature extraction process.

2.4 Lengths and Heights of the Attractor

As opposed to triangular attractors, bent attractor arms consist of two parts, whereas the more horizontal edge is referred to as length a and the other one as length b (see figure 6a). In order to determine these lengths and the heights of the attractors, first the column sum of the density matrix N is calculated. To neglect remaining outliers, only entries greater than or equal to 5% of the column sum vector are considered. The first feasible entry denotes the v -coordinate of the leftmost point and the last entry denotes the v -coordinate of the rightmost point of the attractor. Then, the row sum of the density matrix N is calculated and again only entries greater than or equal to 5% of the vector's maximum value are considered as feasible. The position of the first entry denotes the w -coordinate of the highest point of the attractor. Since the lowest point of the attractor is usually located in the south east quarter of the density plot, only columns right of center are considered. The position of

the last entry of the row sum vector of the adjusted matrix labels the w -coordinate of the lowest point. In order to detect the position of the approximately horizontal edge of the attractor, the density plot is converted into a binary image and Hough transform is applied. To find a feasible representative, only lines of 12 degrees above or below the horizontal line are considered as suitable. If two lines fulfil this condition, the lower one is chosen. The horizontal line through the w -coordinate of the middle point of the extracted line represents the lower edge of the attractor. Then, the height h of the attractor is defined as

$$h = \begin{cases} h_{p_w} - l_{p_w}, & \text{if } l_{p_w} < h_{line}, \\ h_{p_w} - h_{line}, & \text{otherwise,} \end{cases} \quad (7)$$

where h_{p_w} and l_{p_w} label the w -coordinates of the highest and lowest point, respectively, and h_{line} denotes the vertical position of the horizontal line. If the considered attractor is triangular in shape, the length of the lower edge a is calculated as

$$a = rm_{p_v} - lm_{p_v}, \quad (8)$$

where rm_{p_v} and lm_{p_v} denote the rightmost and leftmost point, respectively. In case of triangular attractors, the length b is set to zero (see figure 6b). If the attractor has bent arms, the length b is determined by

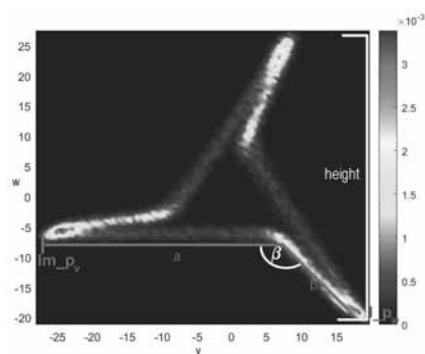
$$b = \frac{|l_{p_w} - h_{line}|}{\sin(\alpha)}. \quad (9)$$

The maximum value in the row of the density matrix corresponding to the w -coordinate of the lowest point denotes its v -coordinate. The edge of the attractor with length b is approximated by a straight line with the following parameters:

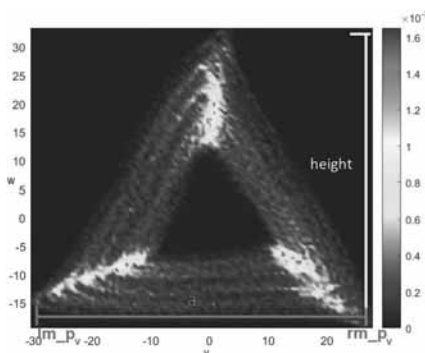
$$k = \tan(-\alpha), \quad d = l_{p_w} - l_{p_v} \cdot k. \quad (10)$$

The length a of the bent attractor is calculated by the difference between the leftmost point and the intersection between the horizontal line and the straight line representing the edge with length b (see figure 6a).

To compare different attractors, the ratio $\frac{b}{a}$ is built. Due to 3-fold rotational symmetry, the process can be repeated after rotating the attractor by 120 and 240 degrees to improve accuracy.



(a)



(b)

Figure 6: Lengths and heights of the attractor. (a) Measurements of a bent attractor, (b) measurements of a triangular attractor.

2.5 Width of the Attractor

The width of the attractor arm measures the variability of a waveform [4, 6]. In order to properly determine the width of one side, a search window is placed on the density plot (see figure 7). In case of triangular attractors, which are approximately symmetrical about the w -axis, the search area is located in the middle of the lower arm. Bent attractors tend to have a smaller gap between the attractor arms, especially on the left side. Thus, 75% of the search window is placed right of the center which has proven to be suitable for the given data set. The other two arms should not affect the calculations; therefore, the size of the window is chosen as slim as possible to cover a significant area but to guarantee no distortion because of the two other sides. In this paper, 10% of length a has granted the best results for the given data set. The width of the attractor arm is determined by a combination of two methods. The first method detects large density differences in the density plot and the second method uses triangular interpola-

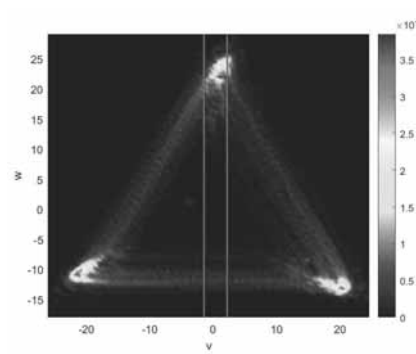


Figure 7: Triangular attractor with placed search window to determine the width of the attractor arm.

tion similar to the Triangular Interpolation of the NN Interval Histogram (TINN) [14].

1st Method. The first method focuses on the largest density differences within the search window and returns the upper and lower limit of the attractor band. For that purpose, the row sum vector of the density matrix within the search area is calculated. In order to find the beginning and the ending of the attractor arm, all entries, which are greater than or equal to 1% of the vector's maximum value, and their positions are determined. The index differences of the determined entries highlight possible density gaps within the window, i.e. jumps from high to very low density regions near zero and jumps back to high density regions. In this study, a gap of at least 3 indices is considered as sufficient for the given data set. The position of the upper limit of the attractor band is marked by the end of the gap, whereas the position of the lower limit is presented by the position of the last entry of the row sum vector.

2nd Method. The second method uses the ideas introduced in [14] and determines the upper and lower limit of the attractor arm by fitting a triangle to the density function in a least square sense. The triangular interpolation is depicted in figure 8, where A denotes the lower limit and B the upper limit of the arm. $D(i)$ represents the values of the row sum vector of the density matrix limited to the search window. In order to guarantee that only the lower attractor band is considered, the method only focuses on the lower 40% of the attractor, which has proven to be suitable for the given data set. To calculate the edges of the triangle, a piecewise linear function $t(w)$ is used:

$$t(w) = \begin{cases} 0, & w \leq A, \\ t_1, & A \leq w \leq D_{max}, \\ t_2, & D_{max} \leq w \leq B, \\ 0, & B \leq w \leq L. \end{cases} \quad (11)$$

D_{max} denotes the position of the highest density value and L marks the limit of the lower 40% of the attractor. In order to determine the limits A and B , the integral over the squared difference $(D(w) - t(w))^2$ has to be minimized, i.e.

$$\int_{-\infty}^L (D(w) - t(w))^2 dw \rightarrow 0. \quad (12)$$

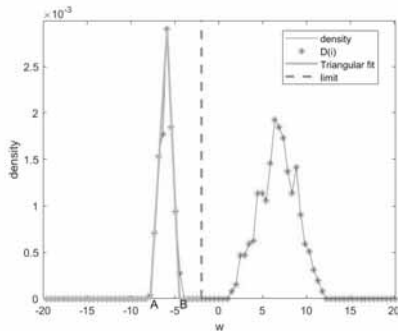


Figure 8: Triangular interpolation of the density function to get the upper limit B and the lower limit A . The width of the attractor arm is defined as $B - A$.

The performance of both methods varies in success depending on the given data set. Therefore, a combination of the two methods is applied to guarantee a proper calculation of the width of the attractor arm (see figure 9). Usually the highest upper boundary and the lowest lower boundary are used with a few exceptions, which have proven to be necessary for the given data set:

- If the upper limit of the first method is higher than $B + 1.5 \cdot (B - A)$, the upper limit is set to B . This constraint ensures that remaining outliers located in the middle of the attractor do not distort the upper boundary.
- Sometimes the second method determines boundaries too generously. If B is higher than the upper limit of the first method but there are no attractor lines between those two values within the search window, the upper boundary of the first method is used.

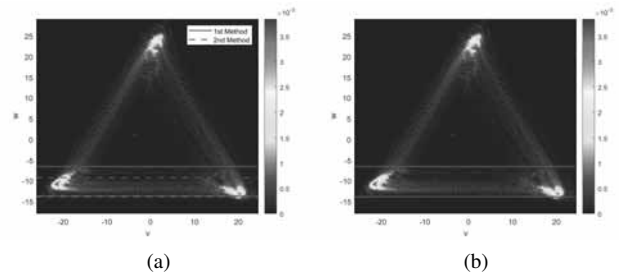


Figure 9: Width of the attractor arm. (a) Upper and lower limits calculated by both methods, (b) combination of the two methods.

- If the lower limit is lower than $A - 0.8 \cdot (B - A)$, the lower boundary is set to A . Again, this ensures that possible outliers have no negative impact on the lower limit.
- If A is lower than the lower limit of the first method but there are no attractor lines between those two values within the search window, the lower boundary of the first method is used to guarantee that the attractor arm is as narrow as possible.

After determining the upper and lower boundary, the width of the attractor arm is defined as the difference between the upper and lower limit. Due to the 3-fold rotational symmetry of the attractor, the procedure can be repeated after rotating the attractor by 120 and 240 degrees to improve accuracy.

3 Results

In order to evaluate the feature extraction method, 90 (three per subject) pulse wave signals chosen at the beginning, after 10 minutes and at the ending of the recording and the corresponding attractors are visually examined. Most of the generated triangular and bent attractors are correctly rotated, as illustrated in figure 10a–10b and figure 11a–11b. The quality of the given data set is crucial for proper quantification of the attractors as remaining outliers lead to chaotic behaviour of the attractors and, as a consequence, to a miscalculation of the angle of rotation θ . Remaining artefacts have a negative impact on two of the 90 attractors and their rotation, as depicted in figure 12a–12b. Further calculations, i.e. the determination of the angle between the attractor arm fragments β and the lengths and widths of the arms, are dependent on the correct rotation. 14 (16%) attractors are triangular in shape and lengths and

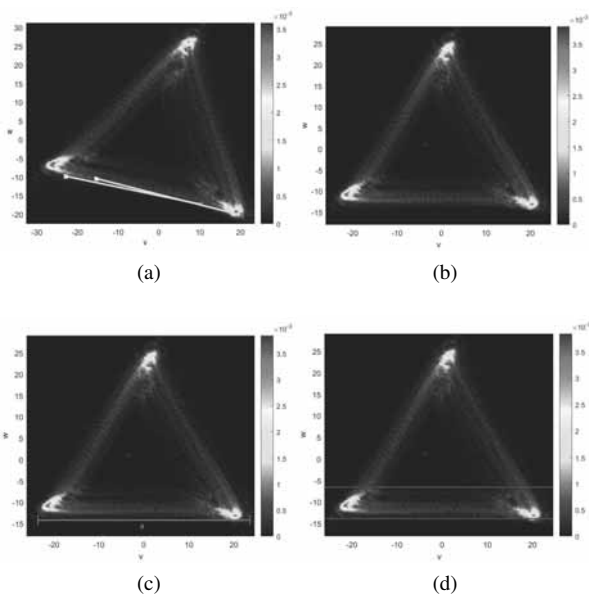


Figure 10: Triangular attractor with correctly extracted features. (a) Attractor with properly detected lower edge, (b) rotated attractor, (c) length of the attractor arm, (d) width of the attractor arm.

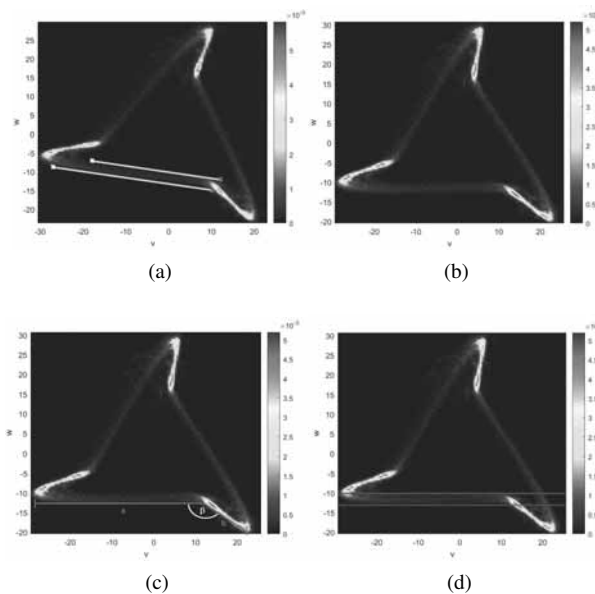


Figure 11: Bent attractor with correctly extracted features. (a) Attractor with properly detected lower edge, (b) rotated attractor, (c) lengths of the attractor arm, (d) width of the attractor arm.

widths of the attractor arms are determined accurately (see figure 10c–10d). The magnitude of the bent attractors are correctly quantified as well, as depicted in figure 11c–11d. However, due to outliers and miscalculations of the angle of rotation θ , the quantification of four attractors is inaccurate. Figure 12c and figure 12d illustrate the wrongly calculated angle between the attractor arm fragments β and, consequently, the incorrectly determined lengths and widths of the attractor arms.

Visual examination also shows that three (3%) attractors are divided into two parts: a smaller attractor with a high density and a larger attractor consisting of only a few lines (see figure 13a). This partitioning is thought to be caused by metrological effects, like varying pressure on the recording device, which lead to a rapid increase in the signal’s amplitude and cannot be detected by the preprocessing method or median filtering. Although the two attractor parts seem to have some similar features, like the angle or rotation and the angle between the arm fragments, the attractor cannot be quantified satisfactorily. The lengths and heights of the attractor refer to the larger attractor part (see figure 13c), whereas the arms widths are extracted from the smaller part with a higher density (see figure 13d).

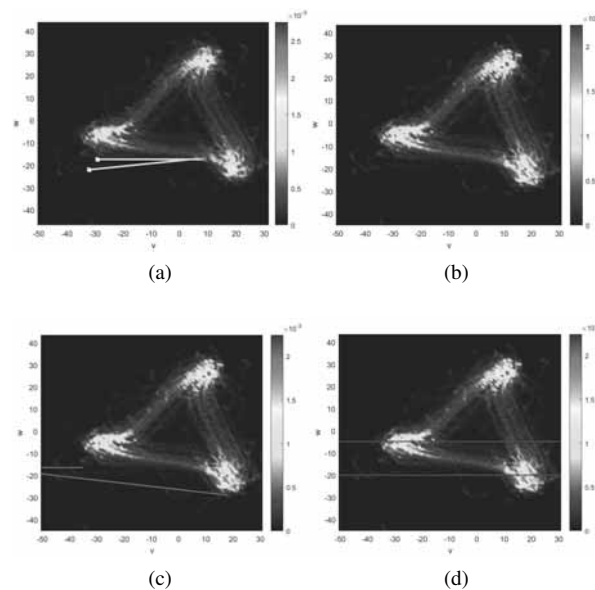


Figure 12: Incorrectly quantified attractor. (a) Attractors with a lot of outliers, (b) incorrectly rotated attractor, (c) incorrect extraction of the attractor arm length represented in red, (d) incorrect determination of the attractor arm width.

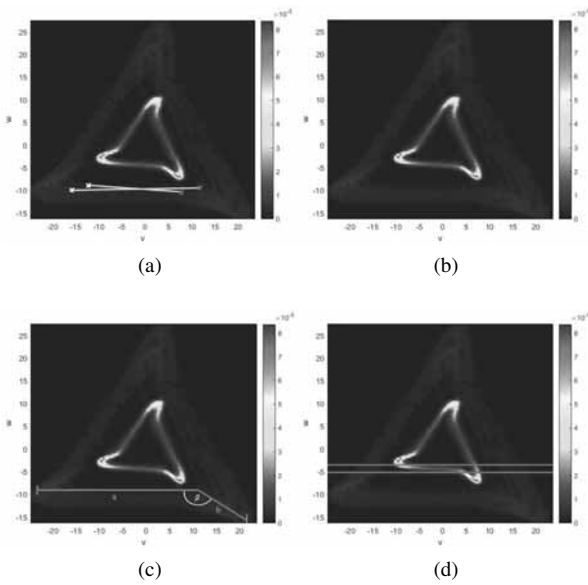


Figure 13: Incorrectly quantified attractor. (a) Attractor consisting of a small attractor with high density and a large attractor with low density, (b) incorrectly rotated attractor, (c) determination of the attractor arm lengths. The applied algorithm focuses on the larger part of the attractor. (d) Calculation of the arm width with a focus on the smaller part of the attractor with high density.

The developed method classifies the attractors into two different shapes: triangular and bent attractors. However, visual examination reveals that three attractors differ in shape and have overlapping arms (see figure 14a). Because of the distinct loops, the attractors cannot be assigned accurately to one of the predefined shapes which complicates further calculations. The overlapping arms distort the angle of rotation (see figure 14a–14b) and determine an incorrect angle between the attractor arm fragments (see figure 14c). Furthermore, the widths of the attractor arms cannot be calculated satisfactorily. Due to the loops, there is no gap in the middle of the attractor, which is an essential condition for determination of the arm width as explained in section 2.5. The missing gap leads to a much broader arm width, as seen in figure 14d.

4 Conclusion and Outlook

In this paper, an algorithm for the automatic quantification of attractors reconstructed from pulse waveform data is presented. The feature extraction technique

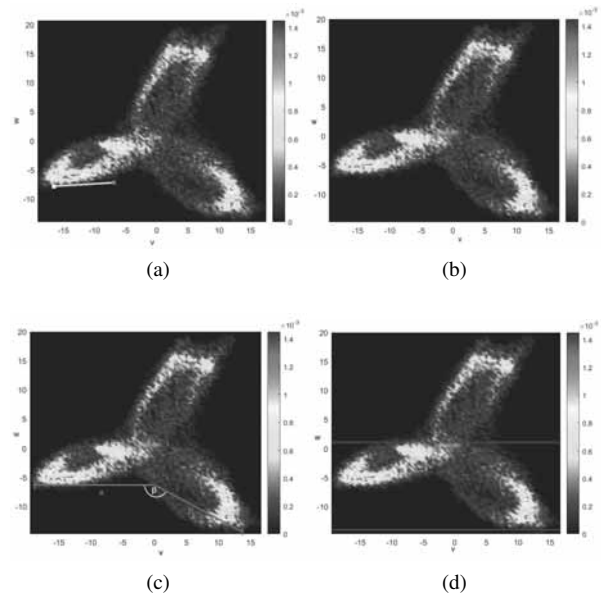


Figure 14: Incorrectly quantified attractor due to its shape. (a) Attractor with overlapping arms, (b) incorrectly rotated attractor, (c) inaccurate extraction of the angle between the attractor arms and the lengths of the attractor, (d) incorrect determination of the attractor arm width.

mainly focuses on a combination of image processing together with the usage of the 100×100 density matrix. Visual examination of the quantified attractors reveals high accuracy of the algorithm in most cases. However, remaining outliers or metrological effects, such as varying pressure on the recording device, have a negative impact on the correct quantification of the attractors. Additionally, the developed algorithm can only distinguish between triangular and bent attractors but is not able to correctly detect attractors with overlapping sides.

Thus, further improvements of the feature extraction technique that ensure a more stable outcome and classify more attractor shapes would be of advantage. Furthermore, the method has been developed to analyse pulse wave data acquired through photoplethysmography at the fingertip. However, it is not assured that the algorithm works equally precise on pulse wave signals recorded with an occlusive cuff, electrocardiogram (ECG) signals [15, 16] or other almost periodic signals. Thus, it would be interesting to apply the developed method on these signals as well and, if necessary, adapt the feature extraction technique accordingly.

Acknowledgement

Part of this research was funded by the State of Lower Austria with co-financing from the European Regional Development Fund (ERDF / EFRE) – Project "smart-PWA" / WST3-F-5030665/002-2017.

References

- [1] Hametner B. and Wassertheurer S. Pulse Waveform Analysis: Is It Ready for Prime Time? *Curr Hypertens Rep.* 2017 Aug 11;19(9):73. doi: 10.1007/s11906-017-0769-3. PMID: 28801878.
- [2] O'Rourke MF., Pauca A., Jiang XJ. Pulse wave analysis. *British journal of clinical pharmacology.* 2001; 51(6):507-522. doi: 10.1046/j.0306-5251.2001.01400.x.
- [3] Wilkinson IB., Cockcroft JR., Webb DJ. Pulse wave analysis and arterial stiffness. *J Cardiovasc Pharmacol.* 1998; 32 Suppl 3:S33-7. PMID: 9883745.
- [4] Nandi M., Venton J. and Aston P. A novel method to quantify arterial pulse waveform morphology: attractor reconstruction for physiologists and clinicians. *Physiol. Meas.* 2018; 39(10):104008. doi: 10.1088/1361-6579/aae46a.
- [5] Fedotov AA. and Akulova AS. Adaptive filter for eliminating baseline wander of pulse wave signals. *World Congress on Medical Physics and Biomedical Engineering.* June 7-12, 2015, Toronto, Canada. pp 1018-1021.
- [6] Aston P., Christie M., Huang Y. and Nandi M. Beyond HRV: attractor reconstruction using the entire cardiovascular waveform data for novel feature extraction. *Physiol.Meas.* 2018; 39(2):024001. doi: 10.1088/1361-6579/aaa93d.
- [7] Takens F. Detecting strange attractors in turbulence. In: Rand D., Young LS. editors. *Dynamical Systems and Turbulence.* Springer Berlin Heidelberg. 1981. pp 366-381.
- [8] Bachler M., Sehnert W., Mikisek I., Wassertheurer S., and Mengden T. Non-invasive quantification of the effect of device-guided slow breathing with direct feedback to the patient to reduce blood pressure. *Physiol Meas.* 2020; 41(10):104002. doi: 10.1088/1361-6579/abb320.
- [9] MathWorksI 2021. MATLAB Function Reference (2021a). Retrieved from https://de.mathworks.com/help/pdf_doc/matlab/matlab_ref.pdf [visited on 20/06/2021].
- [10] Paranjape R.B. Chapter 1 - fundamental enhancement techniques. In: ISAAC N. BANKMAN editors. *Handbook of Medical Image Processing and Analysis.* 2nd edition, Academic Press, Burlington. 2009. pp 3-18.
- [11] Duda R. and Hart P. Use of the hough transformation to detect lines and curves in pictures. *Commun. ACM.* Jan. 1972; 15(1):11-15. doi: 10.1145/361237.361242.
- [12] MathWorks, 2020. Image Processing Toolbox User's Guide (R2020a). Retrieved from https://de.mathworks.com/help/pdf_doc/images/images_ug.pdf. [visited on 06/15/2020].
- [13] Elsalamony H. Chapter 30 - Detecting distorted and benign blood cells using the Hough transform based on neural networks and decision trees. *Emerging Trends in Image Processing, Computer Vision and Pattern Recognition.* Morgan Kaufmann. 2015. pp 457-473.
- [14] Task Force of the European Society of Cardiology the North American Society of Pacing Electrophysiology. Heart Rate Variability: Standards of Measurement, Physiological Interpretation, and Clinical Use. *Circulation.* 1996; 93(5):1043-1065. doi: 10.1161/01.CIR.93.5.1043.
- [15] Lyle JV. et al. Beyond HRV: Analysis of ECG signals using attractor reconstruction. *Computing in Cardiology (CinC).* 2017, pp. 1-4, doi: 10.22489/CinC.2017.091-096.
- [16] Aston P. et al. Deep Learning Applied to Attractor Images Derived from ECG Signals for Detection of Genetic Mutation. *Computing in Cardiology (CinC).* 2019, pp. 1-4, doi: 10.23919/CinC49843.2019.9005823.

Model Order Reduction of Deterministic Microscopic Models - A Case Study

Matthias Rößler^{1*}, Niki Popper^{1,2}

¹dwh GmbH, dwh simulation services, Neustiftgasse 57-59, 1070 Vienna, *matthias.roessler@dwh.at

²DEXHELPP Society of Decision Support for Health Policy and Planning, Neustiftgasse 57-59, 1070 Vienna, Austria

SNE 32(2), 2022, 79-84, DOI: 10.11128/sne.32.tn.10604
 Received: 2020-11-10 (selected ASIM SST 2020 Postconf.
 Publication; Revised: 2021-06-09; Accepted: 2021-06-30
 SNE - Simulation Notes Europe, ARGESIM Publisher Vienna,
 ISSN Print 2305-9974, Online 2306-0271, www.sne-journal.org

Abstract. In this paper we present a method for model order reduction of microscopic models, i.e. models that consist of a high number of entities that can interact and cooperate with each other. Due to this high numbers of entities such models are often highly computationally expensive. But classic model order reduction techniques often use the equations the models are based on to simplify the model and make it more performant. These approaches are not applicable for microscopic models. We present a data-based approach for model order reduction using radial basis functions and analyze the specifics and opportunities of model reduction for microscopic models. As a case study Conway's Game Of Life is used.

Introduction

Microscopic models are typically comprised of a high number of entities that interact with each other in a certain way. In contrast to macroscopic models where the global behavior of the system is described, the dynamics of a microscopic model emerge through the definition of the single entities and their interaction. On the one hand the high number of entities results in computationally expensive simulations on the other hand this usually leads to a high number of parameters that define the behavior of the model. Different modeling approaches lead to microscopic models, for example cellular automata (CA) or agent based modeling approaches (ABM). For this paper we chose to study CAs, specifically Conway's Game of Life.

Parametrized model order reduction (PMOR) aims at reducing the computation time of a parametrized

models. Application fields include control theory, optimization or statistical analysis. There are many different approaches that use the underlying model equations (for example see [1], [2], or [3]), which is not suitable for microscopic models as the underlying equations are not available directly. The most promising approaches that are based on interpolation and are independent of the availability of model equations are techniques that use radial basis functions (RBF) [4]. This approach is based on already available simulation results at other parameter constellations and uses interpolation to approximate the simulation result at a given parameter set.

In this paper the different possibilities of applying RBF interpolation on data generated from microscopic models is investigated. Conway's game of life is used as a stand-in for a population model. The analysis focuses on different possibilities to use the generated simulation results in order to create a suitable interpolant and the results are compared to each other.

1 RBF Interpolation

A closer view of the theory of radial basis functions can be found in [5] or [6]. We summarise some important results.

A function $\psi : \mathbb{R}^d \rightarrow \mathbb{R}$ is called radial, if there exists a univariate function $\varphi : \mathbb{R} \rightarrow \mathbb{R}$ with

$$\psi(x) = \varphi(\|x\|) \quad \forall x \in \mathbb{R}^d \quad (1)$$

where $\|\cdot\|$ is a norm on \mathbb{R}^d , usually the euclidian norm.

An interpolation problem using radial basis functions can be formulated as follows:

Given a set of points $\{x_1, \dots, x_n\}$ (called centers) and a function $f : \mathbb{R}^d \rightarrow \mathbb{R}$, for which the function evaluations $f(x_k)$, $k = 1, \dots, n$ at the centers are known, an

interpolant s_f of f is given by

$$s_f(x) := \sum_{k=1}^n a_k \cdot \varphi(\|x - x_k\|). \quad (2)$$

s_f must fulfill the interpolation conditions $s_f(x_k) = f(x_k), k = 1, \dots, n$

The problem leads to a linear system for a_k :

$$A_\varphi \cdot \begin{pmatrix} a_1 \\ \vdots \\ a_n \end{pmatrix} = \begin{pmatrix} f(x_1) \\ \vdots \\ f(x_n) \end{pmatrix} \quad (3)$$

with

$$A_\varphi := \begin{pmatrix} \varphi(\|x_1 - x_1\|) & \cdots & \varphi(\|x_1 - x_n\|) \\ \vdots & \ddots & \vdots \\ \varphi(\|x_n - x_1\|) & \cdots & \varphi(\|x_n - x_n\|) \end{pmatrix} \quad (4)$$

Obviously A_φ is symmetric. It can be shown that the matrix is positive definite for arbitrary, distinct $x_1, \dots, x_n \in \mathbb{R}^d$ for a certain group of functions. These functions are called (conditionally) positive definite, examples include:

- Linear:

$$\varphi(\|x\|) = \|x\| \quad (5)$$

- Gaussian:

$$\varphi(\|x\|) = e^{-\frac{\|x\|^2}{\varepsilon^2}} \quad (6)$$

- Multiquadric:

$$\varphi(\|x\|) = \sqrt{1 - \frac{\|x\|^2}{\varepsilon^2}} \quad (7)$$

While gaussian functions are positive definite i.e.

$$c^\top A_\varphi c > 0 \quad (8)$$

for arbitrary $c \neq 0 \in \mathbb{R}^n$, linear and multiquadric functions are conditionally positive definite of order 1. This means that c has to additionally fulfill

$$\sum_{k=1}^n c_k = 0. \quad (9)$$

This can be directly incorporated in (3) by adding an

extra equation, which leads to

$$\begin{pmatrix} A_\varphi & 1_{n \times 1} \\ 1_{1 \times n} & 0 \end{pmatrix} \cdot \begin{pmatrix} a_1 \\ \vdots \\ a_n \\ d \end{pmatrix} = \begin{pmatrix} f(x_1) \\ \vdots \\ f(x_n) \\ 0 \end{pmatrix} \quad (10)$$

The shape parameter ε for the gaussian and multiquadric functions has to be chosen carefully, because the quality of the approximation is highly dependent on this parameter.

2 Case Study

Conway's Game of Life [7] is one of the most famous cellular automata. It is defined on a rectangular grid with 2 possible states $\{dead, alive\}$. The update rules are defined as follows:

- A cell that is *alive* stays alive if 2 or 3 neighboring cells are alive otherwise it dies.
- A cell that is *dead* is brought to life if there are exactly 3 living cells in its neighborhood. Otherwise it stays dead.

As neighborhood the Moore-neighborhood (8 neighboring cells, the 4 directly adjacent and the 4 diagonal adjacent cells) is used. The behavior of the model is dependent on the initial states of the cells and it could be called very chaotic as a change of the initial state in a single cell can lead to huge differences after several time steps.

Typically the results of the game of life model are analysed based on the spatial distribution of the living cells over time. But the model can also be viewed as a population model, where the number of living entities is of interest. So the analysis of simulation results can be performed on an aggregated level by counting the living cells in every time step, a similar look at the game of life was done in [8]. For the experiments the game of life is simulated on a 50×50 grid. The time evolution is observed over 50 time steps. For the initial conditions each cell is given a probability of 0.3 to be alive at $t = 0$, an overview is given in Table 1.

Figure 1 depicts the time evolution of the number of living cells for various simulation runs using the parameters given in Table 1. While the chaotic behavior of the game of life is evident in the evolution as well, it can be seen that the basic behavior of the evolution is

grid ($m \times n$)	50×50
time steps (t_{end})	50
init. prob. living (p)	0.3

Table 1: Basic parameters for game of life.

similar for most runs. Throughout the paper the evolution (pop) will be given as relative frequency of living cells against the number of total cells in the cellular automaton ($m \cdot n = 2500$). It can be seen as timeseries with 51 entries corresponding to times $t = 0, \dots, 50$.

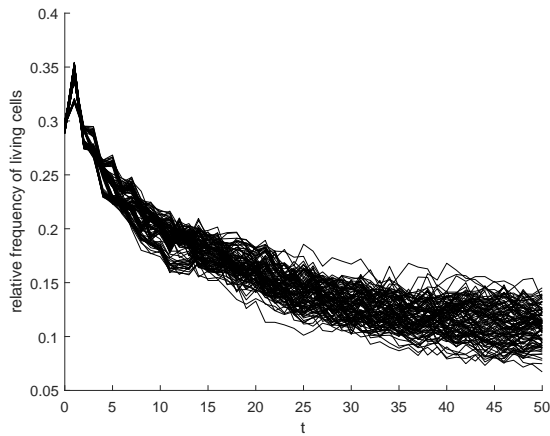


Figure 1: Time evolution of living cells for various simulation runs.

As a measure for the distance between simulation runs s_1, s_2 the Frobenius norm is used:

$$d(s_1, s_2) = \|IC_1 - IC_2\|_F \quad (11)$$

where $IC_1, IC_2 \in \{0, 1\}^{50 \times 50}$ are the initial condition matrices of the respective simulation runs.

3 Experiments

During the experiments two aspects were investigated:

- influence of number of used interpolation points
- influence of minimal distance between an evaluation point and an interpolation point.

A single experiment was built the following way:

1. Fix the minimal distance between an evaluation point and an interpolation point ($d_{min} \in \{1, \dots, 20\}$).

2. Randomly create 10 evaluation points (ep_i) and the evolution of the number of living cells $pop_i(t)$ as reference.
3. Create an interpolation point ($ip_{i,j}$) for each ep_i and add them, as well as their corresponding evolutions $pop_{i,j}(t)$, to the set of interpolation points.
4. Perform the interpolation on the current set of interpolation points and calculate the errors between the interpolated population evolution ($\overline{pop}_i(t)$) and its reference $pop_i(t)$.
5. Repeat steps 1-4 20 times.

The presented experiment setup results in a sequence of interpolations that use more and more simulation results as interpolation points (10 in the first iteration and 200 in the last one). Additionally, it is ensured that for each evaluation point exactly one simulation result with the given distance is added at every iteration.

The error at an evaluation point is calculated as

$$err_i = \frac{\sum_{t=0}^{t_{end}} \|pop_i(t) - \overline{pop}_i(t)\|_2}{t_{end} + 1} \quad (12)$$

and the error of an iteration of the experiment is given as the mean error over all evaluation points.

3.1 Direct Interpolation

For direct interpolation, i.e. directly calculating the resulting evolutions at the given evaluation points, 2 approaches can be distinguished:

- The first idea is to directly interpolate the population evolutions. This means to directly take the initial conditions of the simulation runs as input of the interpolation and the evolutions as the output.

$$s_f : \{0, 1\}^{50 \times 50} \rightarrow \mathbb{R}^{51} \quad (13)$$

- The second idea is to take the initial conditions and the points in time as input for the interpolation and getting the population size (number of living cells) at a specific point in time as an output.

$$s_f : \{0, 1\}^{50 \times 50} \times \mathbb{N} \rightarrow \mathbb{R} \quad (14)$$

For the direct interpolation the use of linear functions and multiquadric functions yielded the best results. So they are presented here. For the multiquadric function $\varepsilon = 1$ was chosen.

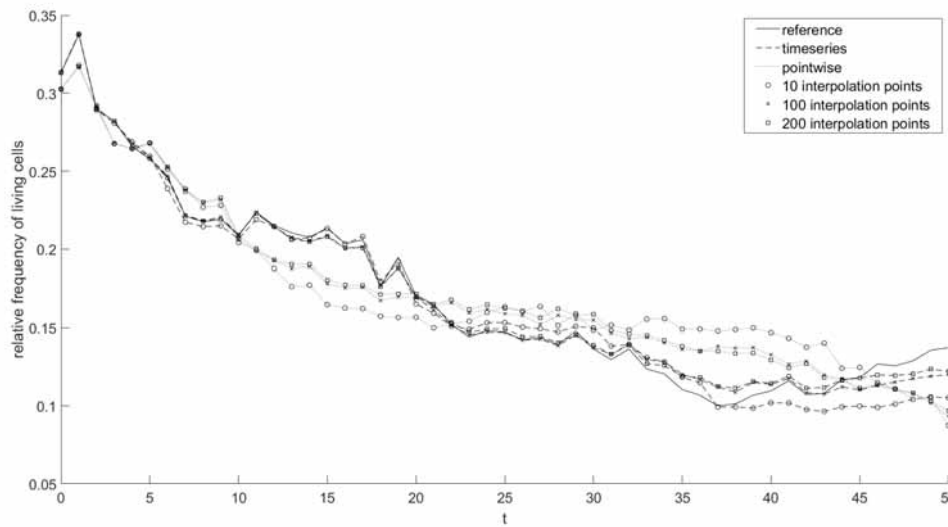


Figure 2: Interpolated time series of a single evaluation point using interpolation data with $d_{min} = 1$ and linear function.

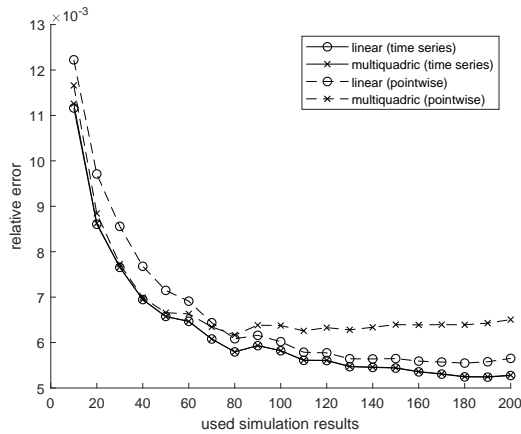


Figure 3: Error of interpolation over used simulation results for $d_{min} = 1$.

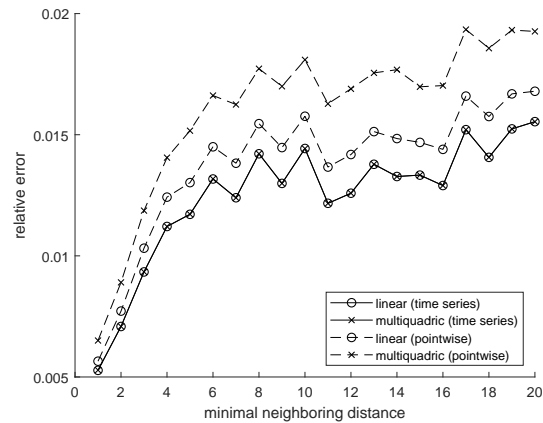


Figure 4: Error of interpolation over minimal neighboring distance for 200 used interpolation points.

Figures 3 and 4 show the errors of the presented approaches using linear and multiquadric RBF-functions. While the errors for the time series approach are basically the same for the different used functions, the errors for the multiquadric pointwise approach are higher than for the linear pointwise approach. It is also more dependent on the minimal distance to the next interpolation point. In order to gain a closer look at the emergence of the errors Figure 2 shows the results of a single interpolation using the linear function. Additionally, the results of using different numbers of interpolation points are depicted, as the minimal neighboring distance $d_{min} = 1$, i.e. the best possible data, was used. It can be seen that the time series interpolation follows the chaotic behavior of the underlying evolution much

more closely than the pointwise interpolation. One possible explanation is that if all points in time are used as interpolation points separately they have a much higher impact on the interpolation result, especially if the distance to the other data points is relatively high.

It is to note, that the pointwise approach results in much more interpolation points as input data. This leads to a significantly bigger interpolation matrix A_φ for which the solution of (3) and (10), respectively, are much more computationally expensive. So even in the case where the pointwise interpolation results in better approximations than the time series approach it has to be assessed if the higher accuracy outweighs the significantly higher computational costs.

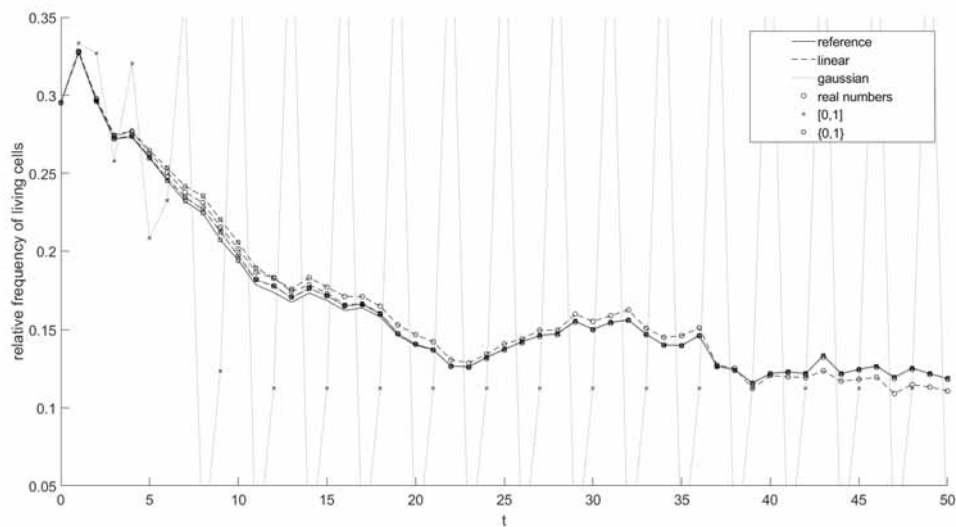


Figure 5: Iteratively interpolated time series of a single evaluation point using interpolation data with $d_{min} = 1$.

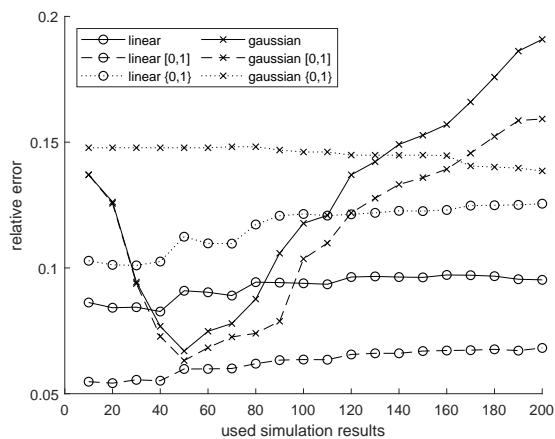


Figure 6: Error of iterative interpolation over used simulation results for $d_{min} = 1$.

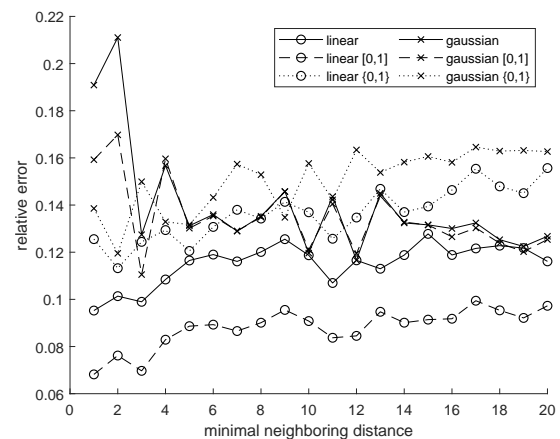


Figure 7: Error of iterative interpolation over minimal neighboring distance for 200 used interpolation points.

3.2 Iterative Interpolation

Another possible ansatz is to not directly interpolate the time evolution of the living cells, but to interpolate a single time step of the game of life, i.e. interpolate every single resulting state on the grid separately:

$$s_f : \{0, 1\}^{50 \times 50} \rightarrow \{0, 1\}^{50 \times 50} \quad (15)$$

The time evolution results from the repeated evaluation of the interpolation at the result of the previous inter-

polation and adding up the states of the resulting state matrix. Again it can be differentiated between different approaches. $x(t) \in \{0, 1\}^{50 \times 50}$ is used as the state matrix at time $t = 1, \dots, 50$

- Using the output of the interpolation directly.

$$x(t) = s_f(x(t-1)) \quad (16)$$

- Projecting the result to the interval $[0, 1]$.

$$x(t) = \max\{\min\{s_f(x(t-1)), 1\}, 0\} \quad (17)$$

- Rounding the result to 0 or 1. ($[\cdot]$ stands for the rounding operator)

$$x(t) = [\max\{\min\{s_f(x(t-1)), 1\}, 0\}] \quad (18)$$

For the iterative interpolation the use of linear functions and gaussian functions yielded the best results. For the gaussian function $\varepsilon = 5$ was chosen.

Figures 6 and 7 show the error curves for the presented approaches. The graphs show that there is no convergent behavior for the error. Even worse especially the use of more simulation results for the interpolation can lead to worse results. There are two explanations for this. First RBF-interpolation often leads to ill-conditioned problems, and second the present interpolation is very sensitive to single data points. This results, in addition to the previously mentioned chaotic behavior of the game of life, to the observed behavior of the error. Generally the magnitude of error is about 2 orders higher than the error of the direct interpolation.

Despite these discouraging results, Figure 5 shows that the gaussian results that are projected to $[0, 1]$ are oscillating and don't predict the population evolution of the game of life. The rest of the results, on the other hand, can indeed approximate the trajectory of the simulation result.

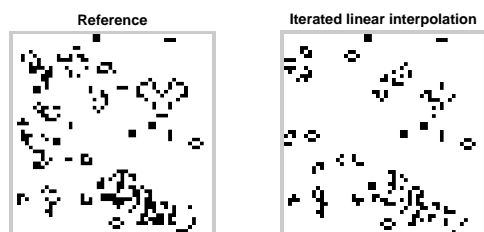


Figure 8: Spatial distribution of living cells at $t = 50$ for the reference simulation (left) and the linear interpolation with rounding (right).

Another characteristic of this approach is, that the spatial distribution of the living cells is approximately preserved during interpolation as can be seen in Figure 8. This characteristic could lead to new ways how microscopic models could be analysed.

4 Conclusion

We presented different approaches to interpolate simulation results of microscopic population models. As a test case Conway's Game of Life was used. The results show, that each of the presented approaches has its own perks and problems, but the overall conclusion is that the methods lead to promising results that should be further investigated.

Especially the iterative approach, that interpolates every state separately, seems promising as it not only approximates the time evolution of the population but can also approximate the spatial distribution within the model.

Future work will focus on error prediction and on ways to automatically adjust the shape parameter ε .

References

- [1] Benner P, Gugercin S, Willcox K. A survey of projection-based model reduction methods for parametric dynamical systems. *SIAM review*. 2015; 57(4): 483–531. doi: 10.1137/130932715
- [2] Ionita AC, and Antoulas AC. Data-Driven Parametrized Model Reduction in the Loewner Framework. *SIAM Journal on Scientific Computing*. 2014; 36(3): 984—1007. doi: 10.1137/130914619
- [3] Constantine P, Wang Q. Residual Minimizing Model Interpolation for Parameterized Nonlinear Dynamical Systems. *SIAM Journal on Scientific Computing* 2012; 34(4): 2118–2144. doi: 10.1137/100816717.
- [4] Haasdonk B, Santin G. Greedy Kernel Approximation for Sparse Surrogate Modeling. In: Keiper W, Milde A, Volkwein S, editors. *Reduced-Order Modeling (ROM) for Simulation and Optimization*. Cham: Springer; 2018. p 21–46
- [5] Wendland H. *Scattered Data Approximation*. (Cambridge Monographs on Applied and Computational Mathematics). Cambridge university press, 2004. doi: 10.1017/CBO9780511617539
- [6] Fasshauer, GE. *Meshfree Approximation Methods with MATLAB*. World Scientific, 2007.
- [7] Berlekamp ER. *Winning ways for your mathematical plays*. 2nd Edition. Natick, Mass: A.K. Peters Ltd; 2001.
- [8] Bicher M, Popper N. Spatial Effects in Stochastic Microscopic Models - Case Study and Analysis. *IFAC-PapersOnLine*. 2015; 48(1): 153—158

Procedure Model to Estimate Bundled Energy Demand for Energy-oriented Simulation Studies

Benjamin Jacobsen^{1*}, Maximilian Stange², Marc Münnich², Tom Schwarting²

¹ Chair of Energy and High Voltage Engineering, Chemnitz University of Technology, Reichenhainer Straße 70, 09126 Chemnitz, Germany, *benjamin.jacobsen@etit.tu-chemnitz

² Fraunhofer Institute for Machine Tools and Forming Technology IWU, Reichenhainer Straße 88, 09131 Chemnitz, Germany

SNE 32(2), 2022, 85-92, DOI: 10.11128/sne.32.tn.10605
 Received: 2020-11-10 (selected ASIM SST 2020 Postconf.
 Publication; Revised: 2022-04-29; Accepted: 2022-04-30
 SNE - Simulation Notes Europe, ARGESIM Publisher Vienna
 ISSN Print 2305-9974, Online 2306-0271, www.sne-journal.org

Abstract. Industrial parks are the backbone of every developed industry. They exist in various forms, differing in the composition of resident companies, their size and their underlying energy infrastructure. In the ERDF-funded research project “GRIDS - Green Energy for Industrial Networks” the potentials and improvement possibilities of innovative energy supply concepts in commercial and industrial parks were investigated. An elementary challenge is the prediction of the (bundled) energy demand, which is necessary for the ecologically and economically sustainable long-term design of energy supply concepts. The data available to planners and researchers for such projects is usually incomplete and undetailed or simply non-existent. Therefore, this paper presents an approach that uses statistical methods to provide better estimates of the bundled energy demand of business parks. This method supports the efficient planning of sustainable energy concepts.

Introduction

For an initial assessment of sustainable and cost-effective energy concepts in industrial parks, direct data collection and measurement is usually too costly and time-consuming. Analyzing comparable energy consumers alone is also unable to provide comprehensive information about the situation at the planning site. Because it cannot be assumed that even companies of identical industry, size and structure have the same load profile. Another barrier is that energy data is often not made available because it is frequently considered sensitive data in manufacturing companies.

In addition, particularly smaller companies lack transparency with regard to their energy data. These are usually very undetailed e.g., based solely on monthly invoices from the energy supplier. The result is that in many projects there is only an insufficient data basis for the reliable planning of energy networks.

However, knowledge about the temporal course of the energy and power demand is a basic prerequisite for a sustainable design of the energy supply system with the aim of increasing the share of renewable energies and the integration of energy storage options. In this context, the integration of hydrogen-based energy systems is attracting increasing interest in science and practice, which will be discussed in more detail in the application section. Only with the right and accurate information is it possible to plan operating resources efficiently, which is important given the often enormous amounts of investment involved, the long-term nature of the largely irreversible investments and lock-in effect of greenhouse gas emissions associated with the energy infrastructure in use [1, 2].

Based on this, a methodology was developed that provides a process model for estimating the energy demand of bundled supply concepts. By using the of the proposed method to estimate the energy demand of (heterogeneous) energy consumer groups, as they are represented by companies in business parks, the simulation and the design of the energy systems can be improved, thus the network planning based on empirical values can be supported by a target-oriented method [3].

The aim is not to establish new standard load profiles, but to apply the established ones in such a way that they can be used at the company and business park level. For that purpose, the paper presents a brief overview of the state of the art of energy data collection, followed by a short introduction of the the proposed procedure model.

Based on this, results of the methodology are presented and illustrated by an application example for the integration of hydrogen into an industrial park. This paper is an extended and adapted version of the original paper by Jacobsen and Stange presented in 2020 [4].

1 State of the Art

The identification of internal optimisation potentials and the requirements of external stakeholders (e.g., energy suppliers, customers etc.) make energy data collection necessary and helpful for many companies. Examples of external drivers are:

- In Germany companies with an annual requirement of $\geq 100,000 \frac{kWh}{a}$ must record their actual load profile (according to §12 StromNZV).
- Introduction of an energy management system according to DIN EN ISO 50001 in order to receive refunds on electricity tax (according to §10 StromStG).
- Energy data as a basis for calculating company-wide carbon emissions in order to achieve carbon neutrality for example in accordance with BSI PAS 2060 [5]. This results from growing demands from customers regarding sustainability.

In general, a distinction can be made between three types of energy data collection [6].

1.1 Calculation

The calculation of energy values requires a comprehensive basis of technical and organizational data, which is not always readily available. For example, an annual energy requirement can be estimated with the help of the performance data of a machine and its operating times. The advantage of this method is that no measuring equipment or intervention in the running operation is necessary. A disadvantage is the complexity of the calculations, e.g. to calculate the total energy demand of a building. It can be assumed that smaller companies in particular do not have the necessary knowledge to carry out these calculations [7].

1.2 Temporary measurement

With the help of temporary measurements, the data basis for the calculations of energy data can be improved. The costs are higher than for a simple calculation, but the data basis and the calculation results can be validated. In addition, the costs are lower than those of permanently installed measuring devices [7].

1.3 Permanently installed measuring device

This type of energy data collection is particularly suitable for in-depth analyses and offers automation options for the collection of energy-related data. On the other hand, however, the acquisition costs are high and the data volumes require a great deal of evaluation [7].

Any type of energy simulation, be it simulations for the design of supply grids, an energy-oriented material flow simulation to investigate the effects of energy flexibility measures or the simulation of technical building services in a factory, require a suitable database to create energy models [8]. The underlying approaches to energy data collection for the simulation are based primarily on temporary energy measurements [8]. Such approaches can still be justified on the scale of a production system or factory, but for the energy analysis of an entire commercial or industrial park, the effort is too high in most cases.

In order to generate energy data for commercial and industrial parks without much measurement effort, standard load profiles could theoretically be used. Standard load profiles are representations of a load curve over a defined period of time. The German Association of Energy and Water Industries (BDEW) has created such profiles for the commercial and household sectors [9]. Reliable standard load profiles do not exist for industrial companies, as the load profiles exhibit very different patterns [10]. In order to nevertheless generate standard load profiles from a few measurements, Emde et al. developed a method for energy-intensive industry [10]. One of the advantages is a faster simulation of energy efficiency measures.

In the aforementioned project GRIDS it was also confirmed that the known standard load profiles should not be used to simulate the electrical energy demand of modern industrial enterprises without some adjustments. Contrary to the approach presented by Emde et al. [10] a bundled load profile is aggregated in the present paper through the synthesis of different standard load profiles of the BDEW [9].

2 Methodology

The procedure model is based on the use of standard load profiles. When using standard load profiles, general statements on the consumption behaviour of electrical energy can only be created for certain user groups [9]. Accordingly, it is necessary that the energy consumers grouped together are regarded as homogeneous.

Only in this way can an estimation of the energy demand of an entire area be realised in the necessary quality. However, project results have shown that such assumptions cannot be made [11]. For this reason, the procedure model for the improved estimation of bundled energy demand was developed. This model can form the basis for the demand planning of the electrical power supply network. The aim is to select the appropriate standard load profiles in such a way that the security of supply of the networks is maintained and supported. Oversizing, as is the case with the classic application of standard load profiles, is thus to be avoided. The basic procedure for network planning with the help of standard load profiles is shown in Figure 1.

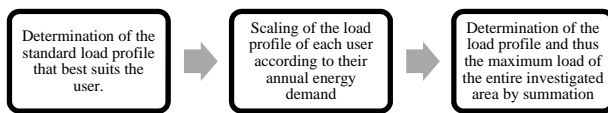


Figure 1: Procedure for determining the load profile and the maximum loads when standard load profiles are used.

With the help of stochastic methods, such as correlations and further significance analyses, connections of the individual actual and summarised load profiles to known standard load profiles are investigated [12].

The correlation coefficient (r) describes the correlation between two variables [13]. This coefficient has a range of values between -1 and 1 ($W_r = [-1; 1]$). The more it approaches 1, the more pronounced the correlation between the two variables, whereby a positive correlation coefficient ($r > 0$) indicates an equally positive correlation; if one variable increases, the other also increases. In general, a correlation coefficient greater than 0.5 ($|r| > 0,5$), is considered a high correlation [14]. Various methods can be used to calculate the correlation. Many variables examined and simulated in practice are normally distributed, so Pearson's method is usually used. However, in many cases it becomes apparent that a test of the type of distribution should be carried out before the method is selected [15]. The presence of a normal distribution can be checked by determining skewness and kurtosis. For normally distributed variables, both values should be close to 0. The following table shows a significant deviation of the standard load profiles from this criterion.

	G0	G1	G2	G3
Skew	6,14	11,28	-0,09	1,14
Kurtosis	-6,63	-3,06	-7,12	-8,38

Table 1: Skewness and kurtosis of the standard load profiles G0 to G3.

The standard load profiles (SLP) G0 to G3 describe the load profiles usually used as a basis, differentiated by trade type, whereby G0 describes general trades (formed from the mean value of the SLP G0 to G6), G1 describes trades with working hours from 8 a.m. to 6 p.m. on weekdays, G2 describes trades with a predominant energy demand in the evening hours and G3 describes passing trades [12].

Due to the distribution type of the data, the calculation of the correlation coefficients according to Spearman is used here. The test for standard normal distribution according to skewness and kurtosis has shown that the examined load profiles and standard load profiles are not normally distributed quantities. Therefore, no parametric methods can be applied to the examined variables and the use of Spearman correlation is preferable to Pearson correlation [16].

In the case of a mere mathematical analysis of the correlations, however, errors can occur in the application even with the correct choice of method; these are often described in the literature by so-called spurious correlations. These are mathematically correctly calculated correlations which, however, only allow insufficient conclusions to be drawn about the real dependency when viewed causally [17]. When investigating the correlation between standard load profiles and the actual load profile, a spurious correlation must be ruled out.

The load profiles were created on the basis of a representative sample. The sample results from surveys conducted as part of a research project. Real load profiles of medium-sized companies located in an industrial park in Saxony were collected and evaluated. Consequently, as it was expected there was a correlation between the examined real load profiles and the standard load profiles. After all, energy requirements of commercial customers were investigated and the standard load profiles are intended to reflect the requirements of this very customer group. Nevertheless, an additional graphical application of the maximum likelihood method takes place. The necessity of the additional graphical evaluation becomes clear in Figure 2.

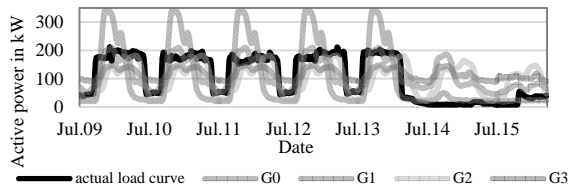


Figure 2: Comparison of the standard load profiles with an examined actual load profile within one week.

It becomes apparent that, in addition to purely mathematical methods, graphical methods should also be used to determine the best fit in order to evaluate the deviation of the actual power demand. This is because the use of correlations only examines the formal correlation of the different load profiles; it does not ensure the actual deviation of the (normalised) energy demand. This additional step enables an improvement of the estimation of energy demands and must be automated in the future by suitable procedures. The improvement is mainly achieved by separating the load profiles by time of day as well as by day of the week. Finally, an adapted synthetic load profile is composed in such a way that a best fit can be ensured according to visual progression (whereby correlation, energy quantity and peak load are equally represented) for day and night as well as for weekdays and weekends combined. After adjusted synthetic load profiles (load profiles for night - working day; day - working day; weekend) are formed for the prediction of the bundled energy demand and combined into a load profile, they are scaled on the basis of the expected total energy demand. The scaling in this case is done with the aim of equality of the expected annual energy demand and the integral of the modelled adjusted synthetic load profile.

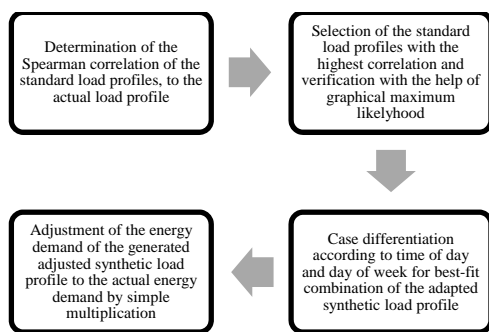


Figure 3: Procedure for determining the load profile and the maximum loads when using adapted synthetic load profiles.

The advantage of the method comes into play when a sufficiently large database is available due to continuous application. It is thus possible that only the industry, as well as the shift model and the expected annual energy demand and the expected maximum load are required as input parameters for later simulations. The initial implementation of the method presented here has shown that it is able to reproduce load profiles more accurately than with the help of the established standard load profiles. A possible extension of the method is the comparison of the results with reality and an adjustment of the used parameters.

3 Results

The procedure model leads to an improvement of the technical design of supply networks and thus supports the ecological and economic optimisation in planning and simulation. The formation of adapted combined synthetic load profiles enables an efficient estimation of the energy and power demand of user groups of electrical energy. The lack of a normal distribution of the energy demand leads to the use of Spearman correlations and thus to deviating results compared to the generally accepted use of Pearson correlations [18, 19]. However, it could be shown that a normal distribution cannot be spoken of for (standard) load profiles. In order to be able to apply the generally used Pearson method correctly, the (normalised) skewness and kurtosis would have to be within limits close to zero [20].

Nevertheless, the results showed a clear deviation of the parameters from a normal distribution. To illustrate the importance of choosing the correct method for determining correlation, the results according to Pearson and Spearman for the sample studied are shown in the following table.

	Spearman	Pearson
G0	0.43	0.44
G1	0.51	0.29
G2	0.31	0.33
G3	0.37	0.66

Table 2: Comparison of the correlation coefficients according to Spearman and Pearson.

Choosing an unsuitable method is particularly critical, as this can lead to an incorrect selection of the standard load profiles to be used, as Table 2 shows. Nevertheless, this imprecision would not lead to unusable results through the use of graphical methods (maximum likelihood) and the division of the standard load profiles according to time periods. Yet, it has been shown that the quality of the result of the method for creating the adjusted synthetic load profiles depends significantly on the correct correlation analysis. In the example shown, it can be clearly seen that if the standard load profile G3 (highest correlation according to Pearson's method - compare Table 2) was chosen, a standard load profile would be chosen whose assumptions do not correspond to the actual mode of operation of the companies investigated (G3 applies to throughput businesses, but the local companies usually work in one-shift operation, at most in two-shift operation). Thus, the combination of the standard load profiles G0 to G3 forms a much better estimation of the actual conditions.

At this point it should be pointed out again that the application of the wrong correlation analysis with the right conclusions (choice of SLP G3) already leads to a considerable improvement compared to the conventional approach. According to the approach shown in Figure 1, standard load profile G1 would be used for the industrial park to predict the load profile with its peak load. However, Figure 2 shows that the actual peak load is only about 60 % of the peak load of G1. In current network planning, however, planning is done according to the standard load profiles (so that G1 is usually used as a basis for planning). Thus, a contribution to the optimisation of network planning can be made simply by applying a correlation analysis and deriving correct conclusions. The full potential of the method presented is only exploited by applying the correlation analysis according to Spearman to create adapted synthetic load profiles. Only the combination of the standard load profiles with the highest correlation (only these are shown in Table 1) provides the basis for an improved estimation of the bundled energy demand.

By combining these standard load profiles, not only the load but also the load profile can be predicted very accurately. Finally, overcapacities of the energy grid can be avoided by the presented method. In the example studied, the installed grid capacity can be reduced by 30 % during planning. Nevertheless, an installed transmission capacity of 125 % of the actual maximum load remains, so that no capacity bottlenecks are to be expected.

The method presented also succeeds very well in reproducing the actual load profile. There is an improvement in the average deviation of the predicted from the actual energy consumption of 50 %. This parameter is particularly important for the planning and simulation of possible flexibility measures and their control.

4 Application

Data acquisition is an indispensable phase in any simulation project, as described, for example, in the procedure model by Rabe et al. [21]. It strongly influences the quality of the simulation study. On the other hand, in most simulation projects there are temporal restrictions that prevent or at least limit the collection of primary data. Obtaining meaningful energy data is particularly problematic.

With the help of the procedure presented here, more accurate input data for simulation models can be generated more quickly. This may reduce the time and quality of simulation projects in the area of energy efficiency and energy flexibility measures in commercial and industrial parks significantly and improves the quality and validity of planning measures. The presented method can be applied in the planning of the energy demand of industrial and commercial networks. It is no longer necessary to use the simple standard load profiles, which, from the current point of view, are not applicable for the detailed planning of the supply concept of industrial (and commercial) companies, neither with regards to the peak load nor the load profile. The consequences would usually be overcapacities in network planning and poorly adapted schedules for the supply of electrical energy. The presented method thus makes a decisive contribution to the simulation of energy flows in industrial parks.

Through the increasing adoption of renewable energy sources the energy supply system is being transformed from a central to a more decentralized approach. The grid supply is extended by decentralized energy sources such as photovoltaic and wind energy as well as new energy carriers such as hydrogen. Additionally, cogeneration plants may also supply electricity as well as heat and are a beneficial add-on for renewable energies due to their independence from actual weather.

The share of companies that invest in on-premise energy supply systems is rising constantly mainly to cope with high energy prices and to decrease overall carbon emissions.

Furthermore, storage technologies are established to compensate the fluctuating character of renewable energies and smoothen energy load levels. This may be battery, heat, or even hydrogen storages. Especially green hydrogen is a promising energy carrier to raise self-supply level and store energy for future industrial applications. In combination with fuel cells and cogeneration plants, another decentral supply technology can be established to decarbonize industrial processes.

Thus, the energy supply structures are getting more complex in green- and brownfield planning but also operations. Still, some of these technologies are cost-intensive and many companies do not provide the prerequisites to utilize these technologies in the most cost-efficient way. To address this shortcoming, one solution may be the shared usage of decentralized supply and storage technologies within industrial parks of several companies. According to individual load levels and overall energy demands a shared supply and storage infrastructure can be established which focuses on a high usage of energy from various sources. In this regard, Wei et al. provide an overview of previous publications that consider water electrolysis and the use of hydrogen as one component of the decarbonization of industrial parks [22]. In their publication, they also argue that in the future such hydrogen-based energy supply systems in industrial parks will represent the most economical form of decarbonization [22].

By using the load profiles one can estimate the energy surplus coming from the renewable energy sources. This electrical energy can be used in an electrolyzer to generate green hydrogen. Hydrogen can be used in a fuel cell to cogenerate heat and electrical energy in times of little renewable energy yield. The dimension of those cogeneration units and the combined storage technologies needs to be planned carefully, since the prices for those units are high. An oversized system will never reach its peak performance and leads to unnecessary high investment costs, whereas an undersized unit will not be able to power the grid. For factories, which are in most cases the most common users of industrial parks, there are several more possible applications of hydrogen. The most promising applications are high grade heat generation, the refuelling of fuel cell powered utility vehicles or as feedstock for certain chemical processes [23]. Fig. 4 illustrates a scenario which includes both, centralized and decentralized energy supply and storages for electrical energy as well as hydrogen.

The scenario was modelled for the project H2Wind. Aim of the project is the development of a novel, compact water electrolyzer that operates efficiently and quasi-autonomously in harsh conditions at sea in order to provide green hydrogen for industrial applications, either by pipeline or other means of transport. A simulation can support the investigation of the economical and ecological sustainability of using off-shore green hydrogen in a medium sized industrial park. Users of this industrial park located near the shorelines of the North Sea include a factory for machine tools, a textile factory, a logistics facility and some offices.

The theoretical potentials of these operational scenarios require integrated planning approaches. Especially energetic data of all relevant energy consumers, in this case the companies itself, need to be transparent. Here, the introduced approach can be used to determine the load levels of all the companies and generate an overall load profile to scale the storages and the supply with hydrogen, the cogeneration plant and the physical energy supply infrastructure accordingly. Furthermore, common load profiles can be matched with typical data of solar gains to scale photovoltaic systems and estimate dimensions of battery storages as well.

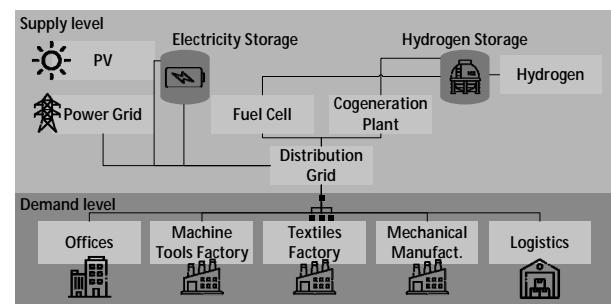


Figure 4: Application of energy supply and storage technologies.

5 Discussion

The procedure model is able to reliably generate energy demands based on the expected total annual energy demand and the assumed peak load. There is an enormous improvement compared to the conventional use of standard load profiles. A disadvantage of the method is the graphical control decision for the choice of the corresponding standard load profile within the individual time periods.

The quality of the control decision again depends on experience and subjective feeling. This procedure is optimised in the course of the further development of the methodology towards an automatic selection, which ensures an objective selection. It has been shown that this additional graphical control or selection of the composition of the adjusted synthetic load profiles limits the effects of a possibly incorrect choice of method for determining the correlations. The finding, which indicates that (standard) load profiles are not normally distributed quantities, shows that data series should always be examined with regard to their distribution type and, if necessary (if no distribution type can be determined), non-parametric methods must be used. It should also be noted that the need to predict energy demand as accurately as possible with the help of synthetic load profiles exists only for electrical energy. When resorting to gas (here in the form of green hydrogen), the pipeline and storage network provides a buffer. However, load profiles must be used again to scale resources for sector coupling (gas to power). This is the only way to efficiently deploy hydrogen fuel cells for system service provision as described by Jacobsen in 2022 [24].

In summary, the presented method contributes to a better simulation of energy demands of industrial companies and industrial and commercial associations. The method itself thus simulates the load profile of companies.

Acknowledgment

This research is supported by the European Regional Development Fund and is co-financed by tax funds on the basis of the budget adopted by the Saxony's state parliament through the project GRIDS – Green Energy in Industrial Networks.



European Union

Europe funds Saxony.



European Regional
Development Fund

The authors also gratefully acknowledge the financial support of the Hydrogen-Lead projekt H2MARE with its sub-project H2Wind (03HY301E) by the Federal Ministry of Education and Research (BMBF) and the project supervision by the project management organization Projektträger Jülich (PtJ).

References

- [1] Sauer M. Das Recht der Vergabe von Strom- und Gas-Konzessionsverträgen im EnWG: Legitimität und Anwendung eines Wettbewerbsinstruments im Kontext des Unions- und deutschen Verfassungsrechts. 1st ed. Baden-Baden: Nomos, 2012.
- [2] Guo Y, Tian J, Chen L. Managing energy infrastructure to decarbonize industrial parks in China. *Nature communications*, vol. 11, no. 1, p. 981, 2020,. doi: 10.1038/s41467-020-14805-z.
- [3] Werth T. *Netzberechnung mit Erzeugungsprofilen: Grundlagen, Berechnung, Anwendung*. Wiesbaden: Springer Vieweg, 2016. [Online]. Available: <https://ebookcentral.proquest.com/lib/gbv/detail.action?docID=4504392>
- [4] Jacobsen B, Stange M. Vorgehensmodell zur Simulation von gebündeltem Energiebedarf. In *Proceedings ASIM SST 2020: 25. ASIM Symposium Simulations technik : 14.10.-15.10.2020 : Online-Tagung, 2020*, pp. 295–301.
- [5] Specification for the demonstration of carbon neutrality. PAS 2060:2014, The British Standards Institution, Apr. 2014.
- [6] Geilhausen M, Bränzel J, Engelmann D, Schulze O. *Energiemanagement: Für Fachkräfte, Beauftragte und Manager*. Wiesbaden: Springer Vieweg, 2015. [Online]. Available: <http://gbv.ebib.com/patron/FullRecord.aspx?p=3567708>
- [7] Wenzel S, Peter T. *Simulation in Produktion und Logistik 201*, Kassel. Kassel University Press GmbH, 2017. [Online]. Available: <https://ebookcentral.proquest.com/lib/gbv/detail.action?docID=5091317>
- [8] G. Posselt G. *Towards Energy Transparent Factories*. 1st ed. s.l.: Springer-Verlag, 2016. [Online]. Available: http://ebooks.ciando.com/book/index.cfm/bok_id/1960675
- [9] Vereinigung Deutscher Elektrizitätswerke - VDEW, "Umsetzung der Analytischen Lastprofilverfahren - Step-by-step," Frankfurt am Main, 2000.
- [10] [Emde A, Zimmermann F, Feil M, A. Sauer A. Erstellung und Validierung von Lastprofilen für die energieintensive Industrie, *ZWF*, vol. 113, no. 9, pp. 545–549, 2018, doi: 10.3139/104.111977.
- [11] Stange M, Jacobsen B, Schubert S, Richter M, Wolf T, Meynerts L. *Leitfaden Green Energy Parks*, 2021.
- [12] Bundesverband der Energie- und Wasserwirtschaft e.V. - BDEW, *Standardlastprofile Strom*.
- [13] Held U. Tücken von Korrelationen: die Korrelationskoeffizienten von Pearson und Spearman. *Swiss Medical Forum*, vol. 10, no. 38, 652-653-653, 2010. [Online]. Available: <https://www.zora.uzh.ch/id/eprint/46199/>

- [14] Cohen J. *Statistical Power Analysis for the Behavioral Sciences*. 2nd ed. Hoboken: Taylor and Francis, 2013. [Online]. Available: <http://gbv.ebib.com/patron/FullRecord.aspx?p=1192162>
- [15] Sedlmeier P. *Jenseits des Signifikanztest-Rituals: Ergänzungen und Alternativen*. [Online]. <https://www.dgps.de/fachgruppen/methoden/mpr-online/issue1/art3/article.html> (accessed: Sep. 14 2020).
- [16] Schober P, Boer C, Schwart LA. Correlation Coefficients: Appropriate Use and Interpretation. *Anesthesia and analgesia*, vol. 126, no. 5, pp. 1763–1768, 2018. doi: 10.1213/ANE.0000000000002864.
- [17] Schäfer A, T. Schöttker-Königer T. *Statistik und quantitative Methoden für Gesundheitsfachberufe*. 1st ed. Berlin: Springer, 2015. [Online]. Available: <http://search.ebscohost.com/login.aspx?direct=true&scope=site&db=nlebk&AN=1078892>
- [18] Myers L, Sirois MJ. Spearman Correlation Coefficients, Differences between. in *Encyclopedia of statistical sciences*, Kotz S, Read CB, Balakrishnan N, Vidakovic B, Johnson NL, Eds., 2nd ed., [Hoboken, N.J.]: Wiley, 2010.
- [19] de Winter JCF, Gosling SD, Potter J. Comparing the Pearson and Spearman correlation coefficients across distributions and sample sizes: A tutorial using simulations and empirical data. *Psychological methods*, vol. 21, no. 3, pp. 273–290, 2016. doi: 10.1037/met0000079
- [20] Field A. *Discovering statistics using SPSS: (and sex and drugs and rock 'n' roll)*. 3rd ed. Los Angeles, Calif.: Sage, 2011. [Online]. Available: <http://www.uk.sagepub.com/field3e/main.htm>
- [21] Rabe M, Spiekermann S, Wenzel S. *Verifikation und Validierung für die Simulation in Produktion und Logistik: Vorgehensmodelle und Techniken*. Berlin, Heidelberg: Springer, 2008. [Online]. Available: <http://nbn-resolving.de/urn:nbn:de:1111-2008093035>
- [22] Wei X *et al.* Roadmap to carbon emissions neutral industrial parks: Energy, economic and environmental analysis. *Energy*, vol. 238, p. 121732, 2022. doi: 10.1016/j.energy.2021.121732
- [23] Imdahl C, Blume C, Blume S, Zellmer S, Gensicke M, Herrmann C. Potentials of Hydrogen Technologies for Sustainable Factory Systems. *Procedia CIRP*, vol. 98, pp. 583–588, 2021. doi: 10.1016/j.procir.2021.01.158
- [24] Jacobsen B. Green flexibility Market – Platform development for system services using fuel cells. *Procedia CIRP*, vol. 105, pp. 158–163, 2022. doi: 10.1016/j.procir.2022.02.027

Model Reduction of Highly Viscous, Non-isothermal Fluids with Free Surface Using Perturbation Theory

Edmond Skeli, Dirk Weidemann, Klaus Panreck,

Institut für Systemdynamik und Mechatronik, FH Bielefeld, Interaktion 1, 33619 Bielefeld
 {edmond.skeli,dirk.weidemann,klaus.panreck}@fh-bielefeld.de

SNE 32(2), 2022, 93-101, DOI: 10.11128/sne.32.tn.10606
 Received: 2020-11-10 (selected ASIM SST 2020 Postconf.
 Publication; Revised: 2022-05-02; Accepted: 2022-05-15
 SNE - Simulation Notes Europe, ARGESIM Publisher Vienna,
 ISSN Print 2305-9974, Online 2306-0271, www.sne-journal.org

Abstract. To improve energy efficiency, the process engineering industry is increasingly tending towards an application of model-based control and diagnosis approaches. Consequently, mathematical models are required that, on the one hand, describe the technical process with sufficient accuracy, but on the other hand do not require too much computational effort. In this regard, the reduction of a model describing the behaviour of a highly viscous, non-isothermal fluid with a free surface is considered. The fluid is modelled by a system of partial differential equations. This system includes both the Navier-Stokes equations and the thermal energy equation describing the temperature behaviour. Using perturbation theory it is shown that the velocities and the temperature of the fluid can be modelled by two reduced models, denoted as submodels. The first submodel is used to calculate the flow dynamics, while the second submodel determines the thermal behaviour.

Introduction

In this paper, the inflow of a highly viscous, non-isothermal fluid into the gap between two counter-rotating cylinders is considered. Note that two conditions have to be taken into account. First, the gap is initially empty and only fills with the fluid over time, so that the inflow of the fluid is a transient process modelled by a system of partial differential equations. This system includes both the time-dependant, incompressible Navier-Stokes equations and the thermal energy equation

describing the temperature behaviour. Second, a bulge forms in front of the gap during filling, the size of which changes over time until a steady state is reached. Since the temporal change of the bulge is not known in advance, the numerical solution of the system of partial differential equations simultaneously requires the determination of the fluid boundary. In the following, the fluid boundary, i.e. the surface of the fluid adjacent to the surrounding air, is also referred to as free surface.

A suitable approach to solve time-dependant, incompressible Navier-Stokes equations with a free surface is the Marker and Cell (MAC) method introduced by Harlow and Welch in [1]. Amsden and Harlow simplified the MAC method in [2] by decoupling the velocity and pressure calculations. Furthermore, in [3, 4] the MAC method is adapted for three spatial dimensions. Using the MAC method an approach to determine the free surface of a highly viscous, non-isothermal fluid entering the gap between two counter-rotating cylinders is proposed in [5]. However, it is not possible to apply it for model-based control or diagnostic approaches due to the high computational effort involved.

In order to decrease the computational effort, it is reasonable to reduce the mathematical model appropriately. Normalising the partial differential equations yields two individual time constants. These time constants allow a qualitative assessment of the transient behaviour of the velocities and the temperature, cf. [6, 7]. Using perturbation theory (cf. [8, 9]), it can be shown that the velocities and temperature of the fluid evolve on different time scales, suggesting that two reduced models, i.e. a fast and a slow submodel, can be used. The fast submodel is applied to calculate the velocities of the fluid, assuming that the fluid temperature does not change during this calculation. In contrast, the slow submodel is used to calculate the temperature, with the steady-state velocity values being determined from a system of algebraic equations.

In section 1, the mathematical model of the fluid, i.e. the system of partial differential equations consisting of Navier-Stokes equations and the thermal energy equation, is converted into a normalised form so that two individual time constants can be determined. Each of the two time constants can be used as normalisation parameter, resulting in either a fast or a slow submodel using perturbation theory, cf. Section 2. A brief presentation of the spatial discretisation and the marker and cell (MAC) method is given in Section 3 and Section 4, respectively. The solution procedure is outlined in Section 5. Finally, the numerical simulation results calculated using the reduced model are presented and compared with the results of the full model in Section 6.

1 Normalising the Model Equations

The spatio-temporal evolution of the velocities as well as the pressure of the highly-viscous, non-isothermal fluid is modelled by incompressible Navier-Stokes equations

$$\frac{\partial u}{\partial t} + u \frac{\partial u}{\partial x} + v \frac{\partial u}{\partial y} = -\frac{1}{\rho} \frac{\partial p}{\partial x} + \frac{\eta}{\rho} \left(\frac{\partial^2 u}{\partial x^2} + \frac{\partial^2 u}{\partial y^2} \right), \quad (1)$$

$$\frac{\partial v}{\partial t} + u \frac{\partial v}{\partial x} + v \frac{\partial v}{\partial y} = -\frac{1}{\rho} \frac{\partial p}{\partial y} + \frac{\eta}{\rho} \left(\frac{\partial^2 v}{\partial x^2} + \frac{\partial^2 v}{\partial y^2} \right), \quad (2)$$

$$0 = \frac{\partial u}{\partial x} + \frac{\partial v}{\partial y} \quad (3)$$

with initial and boundary conditions

$$\mathbf{u}(\zeta, 0) = \mathbf{u}_0(\zeta) \quad \forall \zeta \in \Gamma, \quad (4)$$

$$\mathbf{u}(\zeta, t) = \mathbf{h}(\zeta, t) \quad \forall (\zeta, t) \in \partial\Gamma \times [0, t_e], \quad (5)$$

where u, v represent the velocities in x -, y -direction, respectively.

In the following, $\mathbf{u} = (u, v)^T : \Gamma \times \mathbb{R}_{(+)} \rightarrow \mathbb{R}^2$ denotes the vector of fluid velocities, $\mathbf{u}_0(\zeta) \in \mathbb{R}^2$ the initial conditions and $\mathbf{h} : \partial\Gamma \times \mathbb{R}_{(+)} \rightarrow \mathbb{R}^2$ the boundary conditions, where $\Gamma \subset \mathbb{R}^2$ is the domain and $\partial\Gamma$ the boundary of the domain. Furthermore, $p : \Gamma \times \mathbb{R}_{(+)} \rightarrow \mathbb{R}$ is the pressure, $\rho \in \mathbb{R}$ the density, and $\eta(T) \in \mathbb{R}$ the viscosity.

The spatio-temporal evolution of the temperature is given by

$$\rho C_p \left(\frac{\partial T}{\partial t} + u \frac{\partial T}{\partial x} + v \frac{\partial T}{\partial y} \right) = \lambda \left(\frac{\partial^2 T}{\partial x^2} + \frac{\partial^2 T}{\partial y^2} \right) + 2\eta \left(\frac{\partial u}{\partial x} \right)^2 + \eta \left(\frac{\partial u}{\partial y} + \frac{\partial v}{\partial x} \right)^2 + 2\eta \left(\frac{\partial v}{\partial y} \right)^2, \quad (6)$$

where $T : \Gamma \times \mathbb{R}_{(+)} \rightarrow \mathbb{R}$ represents the temperature and $C_p, \lambda \in \mathbb{R}$ are the specific heat capacity and the thermal conductivity. Let the corresponding initial and boundary conditions be given by

$$T(\zeta, 0) = T_0(\zeta) \quad \forall \zeta \in \Gamma, \quad (7)$$

$$T(\zeta, t) = d(\zeta, t) \quad \forall (\zeta, t) \in \partial\Gamma \times [0, t_e] \quad (8)$$

with $T_0(\zeta), d(\zeta, t) \in \mathbb{R}$.

Normalisation of the variables results in

$$\begin{aligned} u_n &= \frac{u}{\bar{u}}, & v_n &= \frac{v}{\bar{v}}, & \Pi_{px} &= \frac{h^2}{\bar{u}\bar{\eta}} \frac{\partial p}{\partial x}, \\ \Pi_{py} &= \frac{h^2}{\bar{u}\bar{\eta}} \frac{\partial p}{\partial y}, & x_n &= \frac{x}{L}, & y_n &= \frac{y}{h}, \\ t_n &= \frac{t}{\bar{t}}, & T_n &= \frac{T}{\bar{T}}, & \eta_n &= \frac{\eta}{\bar{\eta}}, \end{aligned} \quad (9)$$

where $u_n, v_n, \Pi_{nx}, \Pi_{ny}, x_n, y_n$ represent the normalised velocities, gradients of the pressure, coordinates and t_n, T_n, η_n represent the normalised time, temperature, and viscosity.

Using the normalised variables from (9), the system of partial differential equations, which includes both the Navier-Stokes equations and the thermal energy equation, can be converted to

$$\frac{t_n}{\bar{t}} \frac{\partial u_n}{\partial t_n} = h_1(t_n, \mathbf{r}_n, \mathbf{u}_n, p, T_n), \quad (10)$$

$$\frac{t_n}{\bar{t}} \frac{\partial v_n}{\partial t_n} = h_2(t_n, \mathbf{r}_n, \mathbf{u}_n, p, T_n), \quad (11)$$

$$0 = h_\nabla(\mathbf{r}_n, \mathbf{u}_n), \quad (12)$$

$$\frac{t_n}{\bar{t}} \frac{\partial T_n}{\partial t_n} = h_3(t_n, \mathbf{r}_n, \mathbf{u}_n, p, T_n) \quad (13)$$

with $\mathbf{r}_n = [x_n, y_n]^T$, $\mathbf{u}_n = [u_n, v_n]^T$ and

$$\begin{aligned} h_1(t_n, \mathbf{r}_n, \mathbf{u}_n, p, T_n) &= -Re \left(\frac{h}{L} u_n \frac{\partial u_n}{\partial x_n} + v_n \frac{\partial u_n}{\partial y_n} \right) \\ &\quad - \Pi_{px} + \eta_n \left(\left(\frac{h}{L} \right)^2 \frac{\partial^2 u_n}{\partial x_n^2} + \frac{\partial^2 u_n}{\partial y_n^2} \right), \end{aligned} \quad (14)$$

$$\begin{aligned} h_2(t_n, \mathbf{r}_n, \mathbf{u}_n, p, T_n) &= -Re \left(\frac{h}{L} u_n \frac{\partial v_n}{\partial x_n} + v_n \frac{\partial v_n}{\partial y_n} \right) \\ &\quad - \Pi_{py} + \eta_n \left(\left(\frac{h}{L} \right)^2 \frac{\partial^2 v_n}{\partial x_n^2} + \frac{\partial^2 v_n}{\partial y_n^2} \right) \\ h_\nabla(\mathbf{r}_n, \mathbf{u}_n) &= \frac{\bar{u}}{h} \left(\frac{h}{L} \frac{\partial u_n}{\partial x_n} + \frac{\partial v_n}{\partial y_n} \right), \end{aligned} \quad (15)$$

$$\begin{aligned}
 h_3(t_n, \mathbf{r}_n, \mathbf{u}_n, p, T_n) = & -Gr \left(u_n \frac{\partial T_n}{\partial x_n} + v_n \frac{L}{h} \frac{\partial T_n}{\partial y_n} \right) \\
 & + \left(\left(\frac{h}{L} \right)^2 \frac{\partial^2 T_n}{\partial x_n^2} + \frac{\partial^2 T_n}{\partial y_n^2} \right) + 2\eta_n Br \left(\frac{h}{L} \right)^2 \left(\frac{\partial u_n}{\partial x_n} \right)^2 \\
 & + \eta_n Br \left(\frac{\partial u_n}{\partial y_n} + \frac{h}{L} \frac{\partial v_n}{\partial x_n} \right)^2 + 2\eta_n Br \left(\frac{\partial v_n}{\partial y_n} \right)^2.
 \end{aligned} \quad (16)$$

Here

$$Re = \frac{\rho h \bar{u}}{\bar{\eta}}, \quad Br = \frac{\bar{\eta} \bar{u}^2}{\lambda \bar{T}}, \quad Gr = \frac{\bar{u} h^2}{aL} \quad (17)$$

denote the Reynolds, Brinkmann and Graetz numbers and

$$t_\eta = \frac{\rho h^2}{\bar{\eta}}, \quad \tau_\lambda = \frac{h^2 \rho C_p}{\lambda} \quad (18)$$

the viscous relaxation time and the conductive thermal equilibrium time, respectively.

2 Model Reduction using Perturbation Theory

In the following, the relation between the two time constants given in (18) will be considered in more detail, as these provide information about the transient behaviour of the velocities and temperature. Dividing the viscous relaxation time by the conductive thermal equilibrium time yields

$$\frac{t_\eta}{\tau_\lambda} = \frac{\frac{\rho h^2}{\bar{\eta}}}{\frac{h^2 \rho C_p}{\lambda}} = \frac{\lambda}{\bar{\eta} C_p}. \quad (19)$$

and shows that

$$\tau_\lambda \gg t_\eta \quad (20)$$

holds due to the high viscosity of the fluid. Speaking in physical terms, the relation (20) indicates that the dynamics of the velocities is much faster than the dynamics of the temperature.

Optionally, either $\bar{t} = t_\eta$ or $\bar{t} = \tau_\lambda$ can be used as the normalisation constant. The following two subsections discuss how the equations (10)-(13) change when $\bar{t} = t_\eta$ or $\bar{t} = \tau_\lambda$ is chosen.

2.1 Viscous Relaxation Time as Normalisation Constant

If t_η is chosen as the normalisation constant, $t_\eta/\bar{t} = t_\eta/t_\eta = 1$ and $\tau_\lambda/\bar{t} = \tau_\lambda/t_\eta$ follow for the factors on the left-hand side of (10), (11), and (13) such that the normalised Navier-Stokes equations are of the form

$$\frac{\partial u_n}{\partial t_n} = h_1(t_n, \mathbf{r}_n, \mathbf{u}_n, p, T_n), \quad (21)$$

$$\frac{\partial v_n}{\partial t_n} = h_2(t_n, \mathbf{r}_n, \mathbf{u}_n, p, T_n), \quad (22)$$

$$0 = h_\nabla(\mathbf{r}_n, \mathbf{u}_n). \quad (23)$$

Furthermore, choosing $t_\eta/\tau_\lambda = \varepsilon$ with $\varepsilon \ll 1$ as perturbation parameter and multiplying the thermal energy equation (13) by ε results in

$$\frac{\partial T_n}{\partial t_n} = \varepsilon h_3(t_n, \mathbf{r}_n, \mathbf{u}_n, p, T_n) = 0. \quad (24)$$

The model given by (21)-(23) is referred to as fast sub-model. It will be applied to compute the velocities when a change in momentum occur. Since the temperature does not change significantly over t_η , the partial differential equation (13) does not have to be solved. Rather, as indicated by (24), the temperature can be regarded as being approximately constant.

2.2 Conductive thermal Equalization Time as Normalisation Constant

In contrast to Section 2.1, the choice of τ_λ as normalization constant leads to a system of singularly perturbed partial differential equations

$$\varepsilon \frac{\partial u_n}{\partial t_n} = h_1(t_n, \mathbf{r}_n, \mathbf{u}_n, p, T_n), \quad (25)$$

$$\varepsilon \frac{\partial v_n}{\partial t_n} = h_2(t_n, \mathbf{r}_n, \mathbf{u}_n, p, T_n), \quad (26)$$

$$0 = h_\nabla(\mathbf{r}_n, \mathbf{u}_n), \quad (27)$$

$$\frac{\partial T_n}{\partial t_n} = h_3(t_n, \mathbf{r}_n, \mathbf{u}_n, p, T_n), \quad (28)$$

where ε is defined as described above. Assuming $\varepsilon \rightarrow 0$ the Navier-Stokes equations simplify to

$$0 = h_1(t_n, \mathbf{r}_n, \mathbf{u}_n, p, T_n), \quad (29)$$

$$0 = h_2(t_n, \mathbf{r}_n, \mathbf{u}_n, p, T_n), \quad (30)$$

$$0 = h_\nabla(\mathbf{r}_n, \mathbf{u}_n). \quad (31)$$

The model given by (28)-(31) is referred to as slow submodel and is used to calculate the fluid temperature. When calculating the temperature, the velocities are not to be interpreted as differential, but as algebraic states that have to be adjusted so that the algebraic conditions (29)-(31) are satisfied.

2.3 Hybrid Model

In contrast to the approach in [5], which calculates the inflow of the fluid into the gap using the full model, i.e. the partial differential equations (1)-(6), the approach presented in this paper uses the reduced model equations (21)-(23) and (28)-(31). It can be shown that the computation time decreases significantly by employing the reduced models.

The slow submodel is used as long as no momentum changes act on the fluid. Whereas the fast submodel is used until the velocities of the fluid are stationary. Interpreting an momentum change as event e_{mc} and the occurrence of the stationary velocities as event e_{sv} , the fluid can be modelled by the hybrid automaton shown in figure 1.

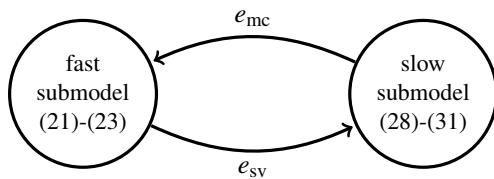


Figure 1: Reduced model as hybrid automaton.

3 Spatial Discretisation

Regarding the use of a numerical method to solve the partial differential equations, a suitable spatial discretisation is required. As depicted in figure 2 the velocities are calculated at the middle of the vertical and horizontal edges of the discretisation grid, whereas the pressure and the temperature are calculated at the centre of a cell. This grid, referred to as staggered grid, is chosen since it allows for the solution to have a tight coupling between the pressure and the velocity.

The partial derivatives of first order can be approximated by

$$D^x f_{i,j} = \frac{f_{i,j+1} - f_{i,j-1}}{2\Delta x}, \quad (32)$$

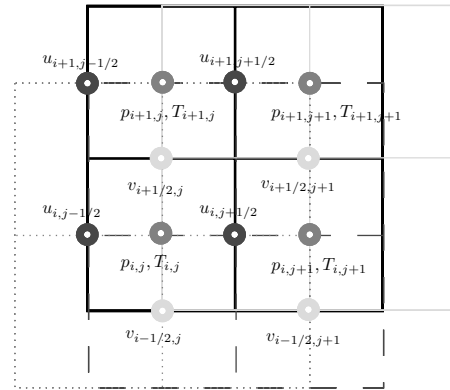


Figure 2: Staggered grid and calculation nodes.

$$D^-_x f_{i,j} = \frac{f_{i,j} - f_{i,j-1}}{\Delta x}, \quad (33)$$

$$D^+_x f_{i,j} = \frac{f_{i,j+1} - f_{i,j}}{\Delta x}, \quad (34)$$

and partial derivatives of second order by

$$K^x f_{i,j} = \frac{f_{i,j+1} - 2f_{i,j} + f_{i,j-1}}{(\Delta x)^2}, \quad (35)$$

where f represents either u , v , p or T , $n_1, n_2 \in \mathbb{R}$ denote the number of discretisation lines in x - and y -direction, $i = 1, 2, \dots, n_1$ and $j = 1, 2, \dots, n_2$ are the indices of the cells, and Δx is the discretisation step in x -direction. The operators D^y, D^-_y, D^+_y and K^y are defined analogously with $\Delta y = f_{\Delta y}(x)$ being the varying step size in y -direction of the curvilinear discretisation grid depicted in figure 3.

The curvilinear discretisation grid has the advantage over a rectangular grid that all points are within the domain Γ . Thus, leading to less computational effort. However, a meaningful use of the curvilinear grid is only possible with sufficiently large radii, as there is a risk of inaccurate calculation with small radii. Note that even with the curvilinear discretisation grid, the velocities are still computed at the middle of the cell edge, while pressure and temperature are computed at the centre of the cell, with the cell contour shown in 3.

Choosing this discretisation the fast system (21)-(23) can be formulated as

$$I\dot{\mathbf{u}}(t) = K(\mathbf{u})\mathbf{u}(t) - Bp(t) + \mathbf{f}(\mathbf{u}(t), p(t)), \quad (36)$$

$$0 = B^T \mathbf{u}(t) \quad (37)$$

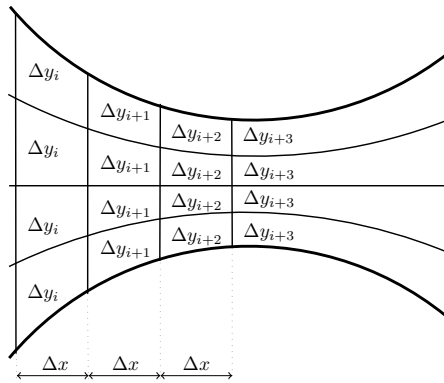


Figure 3: Curvilinear grid.

and the slow system (28)-(31) as

$$0 = K(\mathbf{u})\mathbf{u}(t) - Bp(t) + \mathbf{f}(\mathbf{u}(t), p(t)), \quad (38)$$

$$0 = B^T \mathbf{u}(t), \quad (39)$$

$$I\dot{T}(t) = K_T(\mathbf{u})T(t) + D(\mathbf{u}) + g(T(t)), \quad (40)$$

with I being the identity matrix and $B = [D_+^x, D_+^y]^T$ the discrete divergence operator,

$$K(\mathbf{u}) = \begin{bmatrix} K_1 + N_1(\mathbf{u}) & 0 \\ 0 & K_2 + N_1(\mathbf{u}) \end{bmatrix}$$

with $K_1 = K_2 = K^x + K^y$ representing the linear (diffusion) and

$$N(\mathbf{u}) = \begin{bmatrix} N_1(\mathbf{u}) \\ N_2(\mathbf{u}) \end{bmatrix} = \begin{bmatrix} u_{i,j+1/2} D^x + v_{i,j+1/2}^* D^y \\ u_{i+1/2,j}^* D^x + v_{i+1/2,j} D^y \end{bmatrix}$$

the non-linear (convection) terms. The velocities $u_{i+1/2,j}^*$ and $v_{i,j+1/2}^*$ are averaged velocities defined by

$$u_{i+1/2,j}^* = \frac{1}{4} (u_{i,j-1/2} + u_{i,j+1/2} + u_{i+1,j+1/2} + u_{i+1,j-1/2}),$$

$$v_{i,j+1/2}^* = \frac{1}{4} (v_{i-1/2,j} + v_{i+1/2,j} + v_{i+1/2,j+1} + v_{i-1/2,j+1}).$$

Moreover, $\mathbf{f}(\mathbf{u}(t), p(t))$ and $g(T(t))$ depend on the boundary conditions such that these functions have to be adapted according to the modification of the free-surface, cf. Section 4. Finally, the operators for the temperature

calculation are given by

$$D(\mathbf{u}) = 2\eta((D_+^x u)^2 + \frac{1}{\eta}(D_+^y u + D_+^x v)^2 + (D_+^y v)^2)$$

and $K_T(\mathbf{u}) = (K_1 + N_T(\mathbf{u}))$ with

$$N_T(\mathbf{u}) = \frac{u_{i,j-1/2} + u_{i,j+1/2}}{2} D^x + \frac{v_{i-1/2,j} + v_{i+1/2,j}}{2} D^y.$$

4 Determination of the free Surface

The MAC method which was introduced by Harlow and Welch in [1] is implemented to determine the free surface of the fluid. According to the MAC method, massless particles are used to mark the fluid cells, i.e. each cell of the discretisation grid that includes at least one massless particle is part of the area containing the fluid. Thus, the massless particles are referred to as markers. If one or more empty cells of the discretisation grid are adjacent to a cell filled with fluid, the free surface passes through the fluid cell. Such constellations are shown in figure 4 and figure 5, respectively.

Note that normal and tangential stresses on a free surface of an incompressible fluid are equal to zero (cf. [10, 11]). Thus, the boundary values of the velocities and the pressure on the free surface have to satisfy

$$\frac{p}{\rho} = 2\frac{\eta}{\rho} \left[n_x n_x \frac{\partial u}{\partial x} + n_x n_y \left(\frac{\partial u}{\partial y} + \frac{\partial v}{\partial x} \right) + n_y n_y \frac{\partial v}{\partial y} \right], \quad (41)$$

$$\left[2n_x m_x \frac{\partial u}{\partial x} + 2n_y m_y \frac{\partial v}{\partial y} \right] = - (n_x m_y + n_y m_x) \left(\frac{\partial u}{\partial y} + \frac{\partial v}{\partial x} \right), \quad (42)$$

where $\mathbf{n} = (n_x, n_y)$ is the normal and $\mathbf{m} = (m_x, m_y) = (n_y, -n_x)$ is the tangential vector.

The following two examples serve as an explanation for determining the boundary conditions. In figure 4 the marked cell at the bottom left is only adjacent to a single free cell above it. Consequently, the normal component n_x is zero or at least very small, such that (41), (42) simplify to

$$p_{i,j} - 2\eta(D_+^y v) = 0, \quad (43)$$

$$D_+^y u = -D_+^x v. \tag{44}$$

The pressure $p_{i,j}$ and the velocity $v_{i+1/2,j}$ are calculated with (43) and (44), respectively.

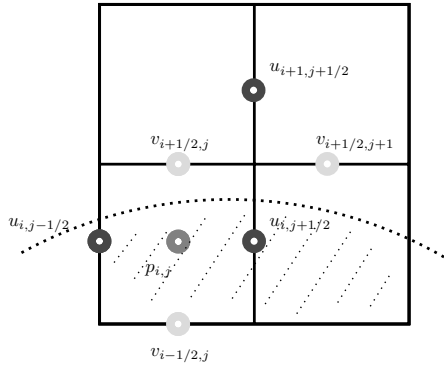


Figure 4: Marked cell with a free adjacent cell.

In figure 5, two empty cells are adjacent to the marked cell, in such a scenario it is assumed that the normal vector has an angle of 45 degrees, i.e., points upwards to the right. In this case, (41), (42) simplify to

$$p_{i,j} - \eta(D_+^y u + D_+^x v) = 0 \tag{45}$$

and

$$D_+^x u - D_+^y v = 0. \tag{46}$$

The pressure $p_{i,j}$ is calculated based on (45), whereas the velocities are set to $u_{i,j+1/2} = u_{i,j-1/2}$ and $v_{i+1/2,j} = v_{i-1/2,j}$ such that (46) is met. Further scenarios can be

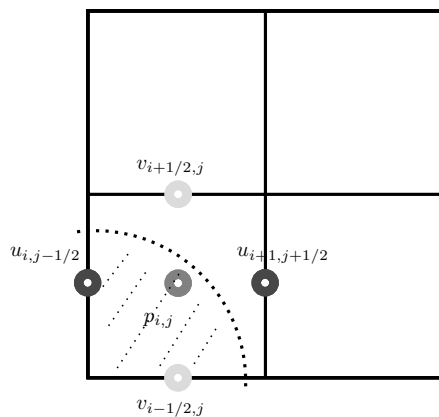


Figure 5: Marked cell with two free adjacent cells.

found in [2].

5 Solution Procedure

The solution procedure includes both the calculation of the two submodels and the switching between the submodels.

5.1 Fast Submodel

Regarding the calculation of the fast submodel (36)-(37), the projection method of Chorin is implemented according to the algorithm proposed in [12]. Note that the temperature values are kept constant such that $T^k = T^{k-1}$ holds. The algorithm contains:

- Perform a semi-implicit time discretisation of (36)-(37) resulting in

$$\frac{\mathbf{u}^k - \mathbf{u}^{k-1}}{\Delta t} = K(\mathbf{u}^{k-1})\mathbf{u}^{k-1} - Bp^k + \mathbf{f}^k, \tag{47}$$

$$0 = B^T \mathbf{u}^k \tag{48}$$

with Δt being the step size and k the current time instant.

- Decouple the pressure from the momentum equation (47) and calculate the pseudo velocities $\tilde{\mathbf{u}}$ by solving

$$\frac{\tilde{\mathbf{u}} - \mathbf{u}^{k-1}}{\Delta t} = K(\mathbf{u}^{k-1})\mathbf{u}^{k-1} + \mathbf{f}^k. \tag{49}$$

for $\tilde{\mathbf{u}}$.

- Calculate the pressure by solving

$$\Delta t B^T B p^k = B^T \tilde{\mathbf{u}} \tag{50}$$

for p^k and calculate the corrected velocities according to

$$\mathbf{u}^k = \tilde{\mathbf{u}} - \Delta t B p^k. \tag{51}$$

5.2 Slow Submodel

The calculation of the slow subsystem (38)-(40) is done according to the following steps:

- Perform a semi-implicit time discretisation of (40) resulting in

$$\frac{T^k - T^{k-1}}{\Delta t} = K_T(\mathbf{u}^{k-1})T(t) + D(\mathbf{u}^{k-1}) + g(T^{k-1}) \tag{52}$$

and calculate the temperature by solving (52) for T^k .

- Decouple the velocities from the pressure and calculate the pseudo-velocities $\tilde{\mathbf{u}}$ by solving the non-linear system of steady, spatially discretised Navier-Stokes equations given by

$$\mathbf{0} = K(\tilde{\mathbf{u}})\tilde{\mathbf{u}} + \mathbf{f}^k. \quad (53)$$

- Determine the pressure by solving

$$\Delta t B^T B p^k = B^T \tilde{\mathbf{u}} \quad (54)$$

for p^k .

- Correct the velocities according to

$$\mathbf{u}^k = \tilde{\mathbf{u}} - \Delta t B p^k. \quad (55)$$

5.3 Switching Submodels

As long as there are no momentum changes, the slow submodel is used. A change in momentum, indicated by event e_{mc} (see figure 1), is assumed to take place when the fluid enters a cell of the discretisation grid at time t that was previously at time $t - 1$ not filled with fluid. Such a scenario is shown in figure 6, where the left plot shows the cell occupancy at time $t - 1$ and the right plot shows the occupancy at time t .

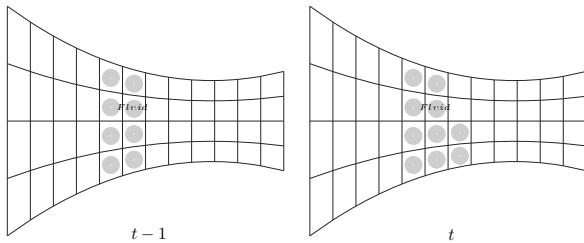


Figure 6: Cell occupancy at $t - 1$ and t .

As soon as the occupied cells do not change and the velocity of the fluid in these cells is stationary, indicated by event e_{sv} , the slow submodel is used. The plot on the left side of figure 7 implies that with constant cell occupancy, the velocities differ at times $t - 1$ and t . In this case, it is imperative to continue using the fast submodel. In contrast, stationary velocities are present in the plot on the right-hand side, so that a submodel switch takes place.

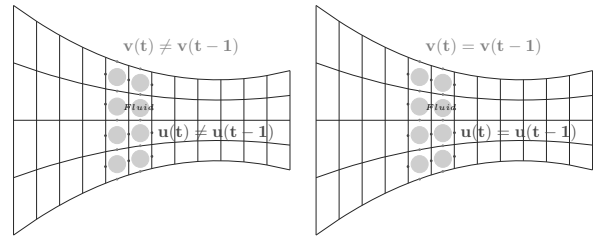


Figure 7: Stationary vs. transient velocities with constant cell occupancy.

6 Simulation Results

Though the complete evolution of all quantities, i.e. velocities, the pressure, and temperature over time have been calculated, in the following only the temperature and the velocity in x -direction at the time t_{ss} are presented, where t_{ss} indicates the time at which the steady state is reached. Note the the computations takes about 10 hours for the full model but only approx. 10 min. for the reduced model.

The initial temperature field in a cross-section located in the middle of the cylinders is depicted in figure 8. As can be seen in figure 8 the initial temperature of the fluid is 425K while the ambient temperature is 400K and the temperature of the cylinders is 433K.

Figure 9 shows the calculated temperature field of the fluid in a cross-section using the full model. In contrast, the temperature field calculated with the reduced model is shown in figure 10. Although there are differences between the temperature field determined by the full model and the temperature field calculated using the reduced model, the reduced model shows a behaviour similar to that of the full model in terms of quality and quantity. Comparing the initial temperature field with either figure 9 or 10, one can see from the temperature change which place the fluid has occupied in the steady state.

For the velocity in the x -direction, a similar characteristic can be seen as for the temperature, with the initial velocity field being shown in figure 13. Only minor differences exist between the results of the full model, shown in Figure 12, and those calculated with the reduced model (see Figure 13). Note that some negative velocities occur in the gap. These negative values result from the high pressure gradient which occurs when the fluid enters the gap, so that the pressure gradient counteracts the flow, resulting in a backflow of the fluid such that a limited bulging occurs in front of the gap. In addition,

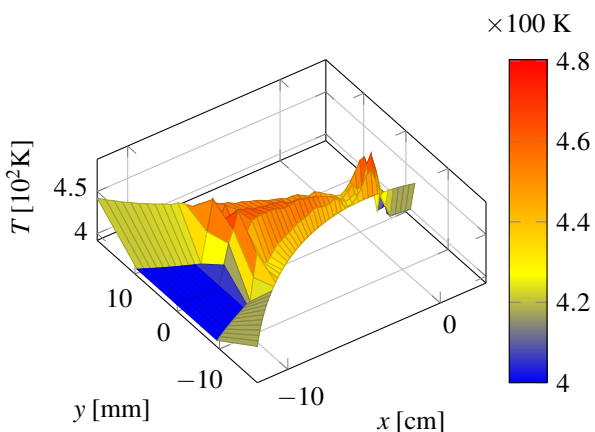


Figure 9: Temperature field in a cross-section (full model).

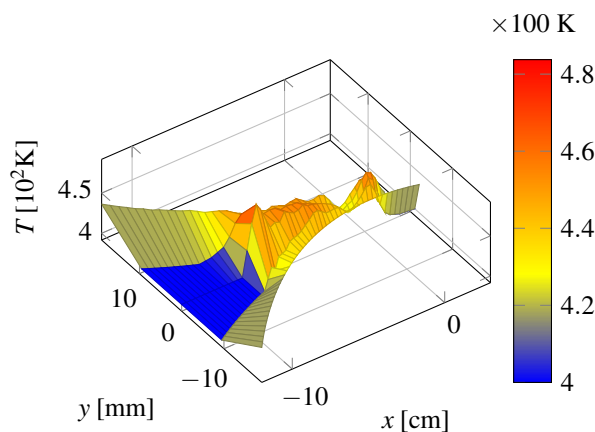


Figure 10: Temperature field in a cross-section (reduced model).

the pressure in some gap sections decreases continuously. In these sections, the pressure gradient acts in positive x -direction, which leads to increased velocities as can be seen in figure 12 as well as in figure 13.

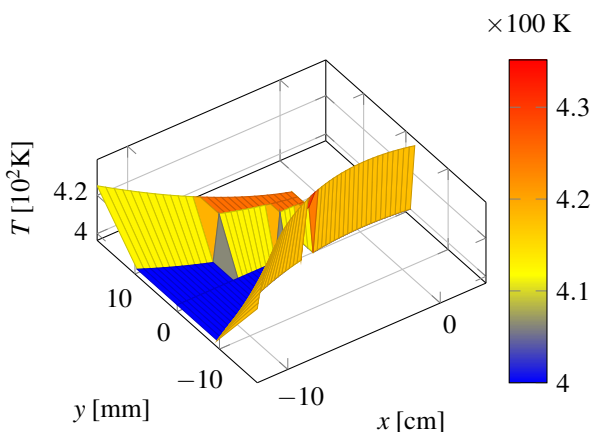


Figure 8: Initial temperature field in a cross-section.

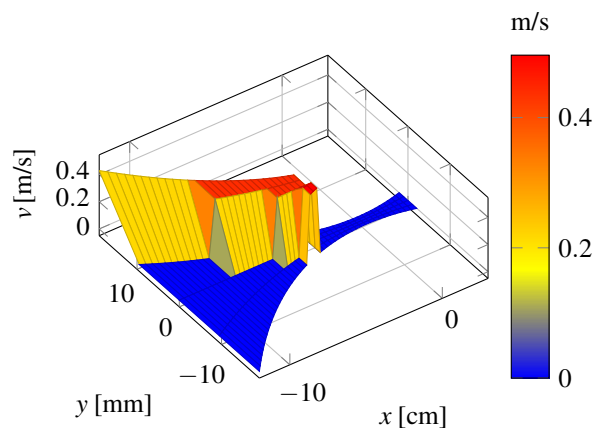


Figure 11: Initial velocity in x -direction in a cross-section.

7 Conclusion

The simulation of models describing the behaviour of highly viscous, non-isothermal fluids is usually associated with a high computational effort. Thus, such models are neither used for model-based control methods nor for model-based diagnosis. Using perturbation theory, however, it can be shown that the velocities and the temper-

ature of the fluid evolve on different time scales, which indicates that two reduced models, i.e. a fast and a slow submodel, can be applied. As long as the fast submodel is used, the velocities are calculated assuming a constant temperature field, since the latter quantity evolves on a lesser time scale. In contrast to the fast submodel, the slow submodel calculates the temperature assuming steady-state velocities evolving on a faster time scale. A comparison of the results calculated with the different models (full model vs. reduced model) shows a high level of agreement. Although the difference in computational effort is significantly (approx. 10 hours for the full model vs. approx. 10 minutes for the reduced model), further model reduction is necessary in order to use the

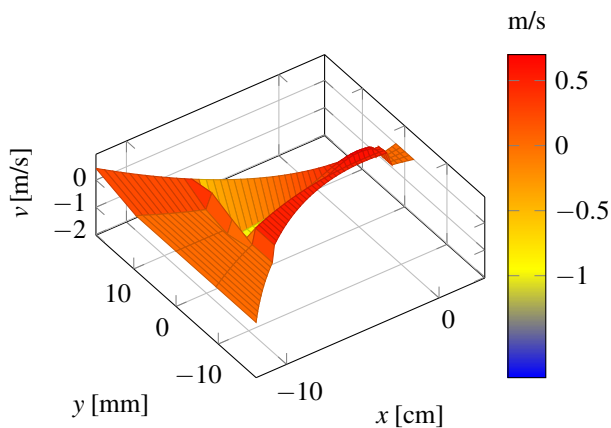


Figure 12: Velocity in x -direction in a cross-section (full model).

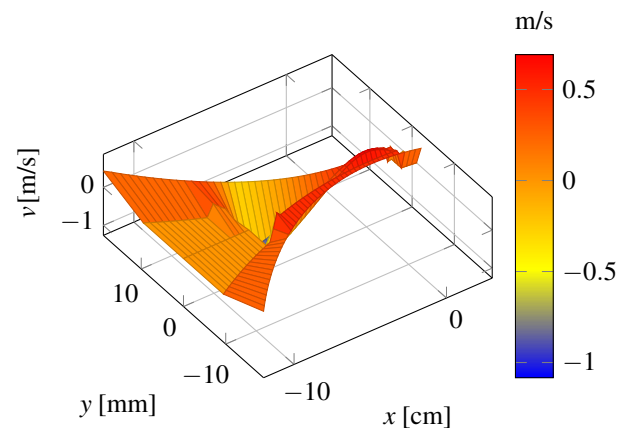


Figure 13: Velocity in x -direction in a cross-section (reduced model).

model reasonably for model-based control and diagnosis approaches.

Acknowledgement

The authors would like to thank the European Union and the federal state of North Rhine-Westphalia, Germany, for the financial support.

References

- [1] Harlow, F. H., Welch J. E., *Numerical calculation of time-dependent viscous incompressible flow of fluid with free surface*, The Physics of Fluids, vol. 8, no. 12, pp. 2182–2189, 1965.
- [2] Amsden, A. A., Harlow, F. H., *The smac method: A numerical technique for calculation incompressible fluid flows*, Los Alamos Scientific Laboratory, University of California, Tech. Rep., 1970.
- [3] Tome, M., Filho, A., Cuminato, J. A., Mangiacavchi, N., Mc-Kee, S., *Gensmac3d: a numerical method for solving unsteady three-dimensional free surface flows*, International Journal for Numerical Methods in Fluids, vol. 37, no. 7, pp. 747–796, 2001.
- [4] McKee, S., Tome, M., Ferreira, V., Cuminato, J., Castelo, A., Sousa, F., Mangiacavchi, N., *The mac method*, Computer & Fluids, vol. 37, no. 8, pp. 907–930, 2008.
- [5] Harder, D., Skeli, E., Weidemann, D., *Modelling and simulation of high-viscosity, non iso-thermal fluids with a free surface*, in Proc. of the 15th Conference on Informatics, Automation, and Robotics (ICINCO), pp. 557–563, 2018.
- [6] Lichte, B., *Verlässliche und effiziente Simulation physikalisch-technischer Systeme durch Nutzung von Fachwissen*, Shaker Verlag, 2006.
- [7] Panreck, K., *Verkopplungsorientierte Modellbildung und Simulation instationärer Extrusionsprozesse*, Dissertation, Univ. Paderborn, 1995.
- [8] Kokotovic, P. V., *Singular perturbation techniques in control theory*, in Singular Perturbations and Asymptotic Analysis in Control Systems, Kokotovic, P. V., Bensoussan, A., Blankenship, G. L. (Editoren), pp. 1–55, Springer, 1987.
- [9] Verhulst, F., *Methods and applications of singular perturbations - Boundary layers and multiple timescale dynamics*, Springer, 2005.
- [10] Hirt, C. W., Shannon, J. P., *Free-surface stress conditions for incompressible-flow calculations*, Journal of Computational Physics, vol. 2, no. 4, pp. 403–411, 1968.
- [11] Nichols, B. D., Hirt, C. W., *Improved free surface boundary conditions for numerical incompressible-flow calculations*, Journal of Computational Physics, vol. 8, no. 3, pp. 434–448, 1971.
- [12] Weickert, J., *Applications of the theory of differential-algebraic equations to partial differential equations of fluid dynamics*, Dissertation, TU Chemnitz, 1997.

A Bi-Modal Simulation Model to Increase the Resilience of Public Transit Networks

Oliver Ullrich, Daniel Lückerath

Fraunhofer Institute for Intelligent Analysis and Information Systems IAIS, Schloss Birlinghoven,
53757 Sankt Augustin, Germany; *oliver.ullrich@iais.fraunhofer.de*; *daniel.lueckerath@iais.fraunhofer.de*

SNE 32(2), 2022, 103-112, DOI: 10.11128/sne.32.tn.10607
Received: 2021-07-21, Revised: 2021-10-10;
Accepted: 2021-12-15
SNE - Simulation Notes Europe, ARGESIM Publisher Vienna
ISSN Print 2305-9974, Online 2306-0271, www.sne-journal.org

Abstract. Public service infrastructure will increasingly be impacted by climate change and has therefore to become more resilient against extreme weather events and other climate change-related effects. A central part of urban infrastructure is public transit, often mainly consisting of interacting light-rail as well as express and community bus networks. To increase such a system's resilience against small disturbances and larger outages – as they might result from climate change – service providers need a toolbox of potential measures to mitigate such incidents' impact and to re-establish services as soon as possible after an outage. This paper presents a bi-modal urban transit simulation system covering both light rail and (express and community) bus networks. Central aims of the system are to enable operators to evaluate measures against small disturbances and larger outages as they happen, and to evaluate what combination of disaster risk management and resilience-building strategies shows most potential to help increasing the resilience of urban transit systems against extreme weather events resulting from climate change as well as other disasters.

Introduction

To protect their long-term utility against the increasing impact of climate change, urban infrastructure components have to become more resilient against extreme weather events like pluvial and fluvial flooding, heat waves, draughts, and windstorms [1]. Such urban infrastructure includes all types of publically and privately operated communication, electricity, and water networks, waste treatment, industrial facilities, as well as urban transportation.

Over the last decades, infrastructure systems that were perceived up until then as isolated services have transformed to connected ecosystems; tightly organised networks provided by a multitude of actors, involving a myriad of physical and digital structures, and offering services to society through all sorts of physical and digital channels. That includes the different modes of urban transit, including light rail systems, express and community buses, and at least partially integrated individual transportation services like taxi cabs, Uber, and Lyft. Out of all commonly available public transit modes, light rail and bus transit have the highest transit performance [2].

In case of sudden disasters impacting transit systems, including extreme weather and human-made events, operators have to be able to make decisions fast to a) transfer the infrastructure components into a pre-planned disaster mode and b) to be able to re-establish services as soon as the immediate event has passed. These operators can be assisted with a simulation application covering both light rail and bus transit that executes simulation runs sufficiently fast to enable evaluation and comparison of potential decisions and strategies, thereby contributing to increase the resilience of the transit system.

This paper presents a bi-modal simulation model representing an urban area's integrated light rail and bus transit network, designed to assist with increasing the transit infrastructure system's resilience against extreme weather events and human-made disasters. A specific focus is put on a) fast execution and b) the representation of operating decisions necessary in disaster risk management situations.

Many models representing urban transit are developed as an extension of already established models of individual traffic [3][4][5]. Many of the more recent simulation models including bus transit use microscopic agent-based modeling approaches [3][4][6][7], the mesoscopic approach to bus transit simulation proposed by Toledo et al. [5] extends a mesoscopic simulation

model for individual traffic based on queuing theory proposed by Burghout in [8], which represents the street network as a graph of interconnected queues and vehicles as individual entities traversing these queues based on speed/density functions.

Especially models utilizing a fine-grained modeling approach generally necessitate the availability of an extensive data basis, including detailed information on origin-destination matrices, vehicular dynamics, signaling strategies, and lane changing rules [9], and include many components which are not immediately interesting for public transit resilience management. This often leads to long runtimes [10][11], thereby rendering those models inadequate for the use case described above. Therefore, this paper builds upon the work presented by Lückerrath [12] by extending a runtime-efficient bus transit model to include light rail transit.

The paper continues by sharing some background on the core components and concepts of urban transit systems (Section 1) and then introduces the developed bi-modal transit simulation model (Section 2). It examines a first round of experiments, specifically concerning execution speed (Section 3), and concludes with an outlook on necessary further research steps (Section 4).

1 Urban Transit Components

Urban transit usually consists of a number of interacting networks, e.g., a light rail system, express and community bus networks, often connected at specific hubs to national rail systems as well as to individual transit systems like taxi cabs, Uber, or Lyft. For the presented model individual transit as well as national rail stations/airports are parameterized and not part of the core model itself.

A mixed light-rail and bus network consists of a network of street and rail segments as well as stops and stations where passenger exchanges take place. These stops and stations are served by a set of transit vehicles executing service trips, i.e., pairings of starting times and sequences of stops, according to a timetable. Each individual vehicle executes several service trips, interspersed with deadhead trips, over the course of an operational day, which is called a rotation. Such a rotation usually begins with a deadhead trip from the vehicle's depot to the first stop of its first service trip and, after a number of service trips, ends with a returning deadhead trip to the depot. The vehicle schedule defines the assignment of specific vehicles to rotations.

While some stops, mainly bus stops, include a bay with capacity for more than one vehicle, many other stops can contain only one vehicle at any given time. Some stops are marked as control points, i.e., locations in the network where control strategies may be employed, e.g., purposely delaying early vehicles until the scheduled departure time is reached. At other stops, vehicles depart as soon as the passenger exchange is completed. Each stop belongs to exactly one station, a geographically grouped collection of stops which usually share a common name.

Directed paths through the network, connecting two successive stops are called connections. They usually consist of several street and/or rail segments, junctions, and signals, that in turn can be shared by several connections.

Signals control access to individual segments, usually at junctions. Often, two or more signals constitute a signal group with a common scheduling strategy.

Urban transit vehicles generally follow pre-defined line routes, consisting of sequences of stops to be serviced. Often, a line consists of a number of line variants: while a main variant might be served by a majority of vehicles, some variants might contain only stops in the city center but not in the suburbs or might branch off the trunk route to connect to a commercial area or business park.

In most public transit systems, daily operations are managed by an operations center, with dispatcher personnel managing procedures for the mitigation of small disturbances and larger outages. While the number and intensity of the smaller disturbances might increase from the impacts of climate change, e.g., changing precipitation patterns, many will originate from everyday incidents, like street segments blocked by accidents, or failing transit vehicle doors. Larger outages might result from extreme weather events, like pluvial or fluvial flooding, high storms, or excessive heat waves – or from human-caused events like protests or terrorist attacks. In case of any of these events, transit operators have a number of remedies at their disposal to keep services running as long as possible, and to restore them as soon as possible. These include the authority to short-turn or cancel trips, to re-route vehicles, and to deploy extra vehicles.

2 Modelling Urban Transit

To represent the described entities and behavior that constitute urban light-rail and bus networks, a bi-modal simulation model based on the event-based approach [13] has been designed.

A description of its design and mechanics are shared in the following sections, highlighting partial models representing physical network components, the logical network, vehicle behavior, operational management, and the necessary randomization. All of these partial models are based on the bus transit model described by Lückerrath and Ullrich [14].

2.1 Physical Network Model

The basis of the model is the representation of the physical transit network as a directed graph. Stops, connections and segments are modeled as nodes of this graph, with their neighborhood relations modeled as edges. Each node has a geographic position, identifying attributes, and a maximum vehicle capacity. Furthermore, each node represents an entity in the sense of the event-based simulation paradigm, i.e., it can be producer and consumer of events. Thus, temporary changes of attribute characteristics, e.g., for modeling disruptions, can be mapped in a simple way via events and activities.

Stops are nodes in the model graph where transit vehicle entities – i.e., busses and light rail cars – stop for boarding and disembarking processes. They always belong to exactly one station and have time-of-day and location-specific stopping times. Different capacity or spatial dimensions of stops are modelled by a maximum number of vehicle entities they can service simultaneously. For example, at a larger stop within a bus station, several vehicles can usually stop at the same time. Whereas at a stop without a separate bay on a busy road, an arriving vehicle may have to wait for an already stopping vehicle before it can approach the stop.

Stations group together geographically related stops and give them a uniform name. They form an additional information layer within the model.

Connections are directed paths in the model graph that link two stops. They have a specific length as well as time of day and location specific average travel times. In addition, they are assigned a planned travel time by the timetable. Depending on the transit system to be modeled and the level of detail of the available data, connection nodes also manage model components of the segments, switches and signals belonging to their connection.

Segments represent subsections of connections, representing road or rail segments between two road junctions or between two switches of a rail transport system. Consequently, their corresponding model components

have a specific length, a scheduled travel time and manage empirical data on their average travel time. In addition, they have an allowed maximum traversal speed, which can be used, e.g., for microscopic simulation of driving behavior. To represent overlaps between different connections, segment nodes can be part of several connection nodes.

To represent the driving behavior of different traffic modes, the model distinguishes between two types of segment nodes: roads and tracks. Road nodes are segment nodes that are used by entities of individual traffic, have an unrestricted vehicle capacity, and do not enforce a fixed vehicle sequence. Without (detailed) information about lanes, it is assumed that there is sufficient space for overtaking maneuvers on each road node, i.e., travel times of individual vehicle entities can be calculated without considering other entities traveling on the node. A more detailed modeling can be achieved by a simple extension of the model by a specialized road node (e.g., based on the modeling of the Mezzo system [5][8]).

In contrast to road nodes, track nodes are used exclusively by rail vehicle entities and enforce both compliance with a maximum vehicle capacity as well as a fixed vehicle sequence. The latter prevents inadmissible overtaking maneuvers between vehicle entities traveling on the same track node and is realized via the travel time calculation (see Section 2.5): If available, the entity traveling directly ahead is always considered to determine the travel time of a vehicle entity newly arriving on a track node. The calculated simulation time at which the new vehicle entity arrives at the end of the track node can never be earlier than that of the entity directly in front. Without possibilities for overtaking maneuvers, the formation of backlogs – even across neighboring nodes – is considered in the model using the vehicle capacity of nodes. The combined length of all vehicle entities driving on the track node at a given time must always be less than or equal to the track length. If the combined vehicle length would become greater than the track length due to a new entity arriving on the track node, the arriving vehicle entity must wait on the neighboring node upstream of the track node until sufficient space is available.

Switches are locations in rail-based transit systems where track crossings take place without interrupting the journey, i.e., they have a unique geographical position and are related to at least three tracks – at least one each incoming and outgoing.

They are modeled as transfer points without spatial extension and are traversed in zero time. Switches can merge several tracks and must be activated to target the correct incoming/outgoing track before an entity can cross them. This is represented in the model by vehicles reserving switches before crossing them and releasing them after a successful transfer.

Signals represent traffic lights of road traffic as well as light signal systems of rail traffic. They usually form a signal group with other signals and have attributes such as switching time or signal status (e.g., green, yellow, red).

Both switches and signals are modelled as additional information layer and not as nodes of the model graph. They can only be found at start or end positions of segment nodes in the model and can be associated with the corresponding nodes based on these positions.

2.2 Logical Network Model

In addition to the physical network components presented so far, logical components such as lines, trips and timetables have to also be considered to model public transit.

Lines consist of an ordered set of stops, which specifies the route to be followed during regular operation. In the simulation model, this is represented by a reference to a set of corresponding nodes of the model graph. To avoid time-consuming dynamic path finding during the simulation run, lines are additionally supplemented by an ordered set of connection nodes. Furthermore, each line can be assigned to a specific transit mode (e.g., bus or train) and may additionally only be served by vehicle types permitted for it. E.g., a low-floor train may not serve a line whose stops are designed for high-floor trains. Accordingly, lines in the model manage references to their transit mode and the vehicle types permitted for them.

Trips combine ordered sets of stops and connections with a start time and are differentiated into service trips and deadheads. In the model, trips manage references to sets of stop and connection nodes, similar to lines. Service trips additionally refer to the line they serve. Deadheads do not follow a predefined route and therefore do not refer to a line in the model.

2.3 Vehicles

Vehicles are represented as transient entities [13] that encapsulate a significant portion of the event-based simulation logic and move across the model graph during a simulation run. Each vehicle entity has a reference to the trip it is currently serving, i.e., at each simulation time it only

has access to the information that is directly relevant for its current activity. All additional information, e.g., about the timetable and the vehicle fleet, is administered by specialized management modules (see Section 2.4).

In the model, vehicles are classified according to their transit mode, their vehicle type, and their individual vehicle characteristics. While transit mode discerns light-rail and bus vehicles, the vehicle type is used for a more detailed subdivision. For example, various types of Vossloh Kiepe GmbH vehicles are in use in the Cologne light rail network, including low-floor vehicles of type K4000 [15] and K4500 [16] and high-floor vehicles of type K5000 [17]. The most detailed classification is based on individual vehicle characteristics. They encapsulate attributes such as passenger capacity, vehicle length, maximum speed, minimum stopping time or boarding rate. This type of modeling allows the representation of vehicle entities of the same type with uniform equipment on the one hand, and on the other hand it allows the representation of disturbances of individual vehicles (e.g., an increased minimum stopping time due to a defective door).

A later extension of the simulation model by further traffic modes is possible in a simple way by creating new vehicle models derived from the generic vehicle model and providing them with individual vehicle characteristics.

Nine simulation event types represent the behavior of bus and light rail vehicles (see Table 1). For a detailed description of the bus-related simulation events see [14]. Figure 1 shows the relationships between the individual event and activity types for light-rail vehicles, based on the associated event process chains.

2.4 Operational Management

The model components presented so far are sufficient for the representation of elementary functions of public transit systems, but they neglect all higher-level management activities that contribute to the functioning and resilience of transit systems. To allow for management on a higher level than individual trips, the timetable must be supplemented by a rotation schedule, which combines trips into groups (so called rotations) [18] that can be executed by individual vehicles within an operating day. These and other management activities are encapsulated in three management modules: the fleet manager, the line manager, and the dispatcher. Thus, changes to the modeling of individual administrative activities do not affect the modeling of other areas of the simulation model. Work in progress on these modules has been reported in [19].

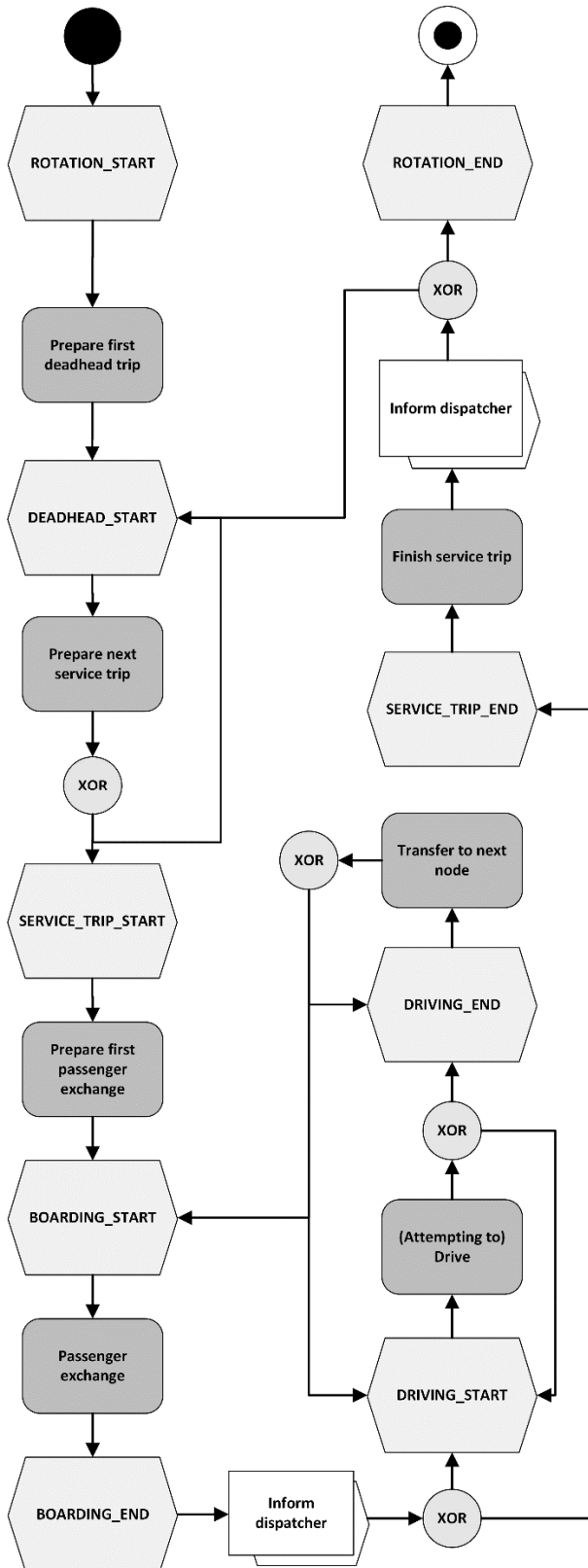


Figure 1: Relationships between the individual event and activity types for light-rail vehicles (based on the associated event process chains).

Simulation event type
ROTATION_START
ROTATION_END
DEADHEAD_TRIP_START
SERVICE_TRIP_START
TRIP_END
BOARDING_START
BOARDING_END
DRIVING_START
DRIVING_END

Table 1: Simulation event types for the light rail and bus vehicles.

Fleet manager

The fleet manager administrates the vehicle fleet and allows other components of the simulation model to access the vehicle fleet via defined interfaces, manages which vehicles are currently in use, and is responsible for generating and managing the initial rotation schedule.

If no rotation schedule is specified by the user, the fleet manager uses a rotation schedule generator to create an (artificial) rotation schedule. Initially, the simulation model is accompanied by a very simple generator, which is able to create schedules with the following properties:

- i. Vehicles only make trips that are allowed for their type.
- ii. Successive trips must belong to lines with identical line numbers.
- iii. End and start stops of successive trips must be part of the same station
- iv. Trips assigned to vehicles follow a permissible time order, i.e., the last trip assigned must end before the next trip starts; and
- v. A user-definable minimum turn time is observed between successive trips assigned to a vehicle.

As Algorithm 1 shows in pseudocode, the procedure traverses the given set of (service) trips (line 03) for this purpose and, for each trip, searches the set of vehicles with permissible vehicle type (line 05) either for a vehicle whose last assigned trip (line 06) satisfies conditions ii. to v. (lines 09 to 11) or, if no such vehicle exists, for a vehicle that has not yet been assigned a trip (lines 07 and 08). If more than one vehicle is suitable to complete a trip, the vehicle whose most recently assigned trip has the earliest scheduled completion time is selected (lines 13 and 14).

If a given vehicle fleet is not suitable to cover all trips under these conditions, or if no information is given about the vehicle fleet, the procedure generates (artificial) vehicle entities and adds them to the vehicle fleet (lines 18 to 22).

```

INPUT: Set of service trips B, vehicle fleet F, minimum
turnaround time tw
OUTPUT: Rotation schedule
01 procedure createRotationSchedule(B, F)
02 begin
03   for all b ∈ B do
04     Vehicle fopt := 0
05     for all f ∈ F with type(f) ∩ type(b) ≠ ∅ do
06       ServiceTrip bf := last(trips(f))
07       if bf = 0 then
08         fopt := f
09       else if lineNumber(bf) = lineNumber(b)
10         and stop(end(bf)) = stop(start(b))
11         and startTime(bf)+travelTime(bf)+tw ≤ startTime(b) then
12         ServiceTrip bopt := last(trips(fopt))
13         if startTime(bf) + travelTime(bf) < startTime(bopt) +
           travelTime(bopt) then
14           fopt := f
15         fi
16       fi
17     od
18   if fopt = 0 then
19     Vehicle fnew := createVehicle(type(b))
20     F := F ∪ fnew
21     fopt := fnew
22   fi
23   trips(fopt) := trips(fopt) ∪ b
24   od
25 end

```

Algorithm 1: Rotation schedule generator.

Line manager

The line manager administrates the lines served as part of a timetable and associates their outward and return directions with each other. In addition, it provides uniform interfaces for accessing individual lines as well as sets of lines. This allows, for example, access to all lines serving a specific stop or a specific connection.

Dispatcher

The dispatcher is the most important and comprehensive management module and can be understood as a model of the operator's decision processes. It holds all the data required for the operational process, such as the current

timetables and rotation schedules at a specific point in time. In addition to managing regular operations, the dispatcher also includes the simulation logic required for traffic management. Four different event types address the module's behavior during regular operation (see Table 2).

Simulation event type
OPERATIONAL_DAY_START
OPERATIONAL_DAY_END
BOARDING_END
SERVICE_TRIP_END

Table 2: Simulation event types concerning the dispatcher module.

The event type OPERATIONAL_DAY_START models the start of the operating day. As a result of this event type, the dispatcher assigns to the vehicle entities of the vehicle fleet, based on the rotation schedule, the first trip to be served by them. A subsequent event of the type ROTATION_START is sent to each assigned vehicle entity.

The end of the operating day is modeled by the event type OPERATIONAL_DAY_END. It signals that all service trips have been performed and all vehicle entities have returned to the depot.

Vehicle entities send events of the type BOARDING_END, which signal the end of the pure boarding process, to the dispatcher during the simulated operating day. The dispatcher then makes further decisions on traffic management measures based on this information. For this purpose, the dispatcher can resort to different strategies (see [14] and [19] for detailed descriptions of different strategies).

For determining the departure time of a vehicle during regular operations, a location-based departure strategy is employed. Under this strategy, selected stops are defined as control stops at which vehicles always have to wait until their planned departure time, as defined by the timetable, has been reached (e.g., to allow transfers between bus and light rail systems). At all other stops of the network vehicles always depart as soon as the boarding process has been completed, regardless of whether the planned departure time has already been reached or not. If the dispatcher receives an event of the type BOARDING_END, it checks whether traffic management measures are to be applied or not. Depending on the result of this check, the waiting time to be added to the entry/exit time is determined.

This waiting time is communicated to the affected vehicle entity by sending it a subsequent event corresponding to the end of the waiting time. This subsequent event can be either of the type `SERVICE_TRIP_END` or `DRIVING_START`. The former is the case when the vehicle entity is at the last stop of its current trip. The latter is sent to tell the entity to move to the next node specified in the line route. In addition to traffic management used under ‘normal operating conditions’, the dispatcher also contains an arsenal of ‘emergency traffic management strategies’ (as described in [19]), e.g., dynamic rerouting of vehicles in case of blocked segments, shortturning of trips in case of high delay, or temporary splitting of routes.

The last event type relevant for regular operation is `SERVICE_TRIP_END`. It represents the end of a service trip and the subsequent signaling of the control center. As a result of this event, the dispatcher assigns the next service trip to the vehicle entity according to the current schedule and initiates the previously required deadhead. It is ensured that the minimum turnaround time specified by the user is observed between the end of one service trip and the start of the next one. If the finished service trip was the last planned trip of the vehicle entity for the simulated operational day, the dispatcher instructs it to end its rotation. If all trips to be performed on this operating day are completed at the end of the service trip, the dispatcher ends the operating day by scheduling an event of type `OPERATIONAL_DAY_END`.

2.5 Randomization

Two randomized elements are part of the proposed model: the vehicle’s traversal time for connections, and the passenger exchange times at stops. Both are directly adapted from [14] with only slight adaptation.

A lognormal distribution is assumed for the **traversal times** for a connection c [20]. Lacking detailed data, the parameters of this distribution, i.e., expectancy value and standard deviation, have to be approximated from the planned traversal times $t_p(c)$. These traversal times usually comprise the planned driving time $t_d(c)$ and the planned passenger exchange time $t_b(c)$, which in turn are comprised of average observed driving/passenger exchange times, standard deviations, and unknown terms (see Equation 1).

$$\begin{aligned} t_p(c) &= t_d(c) + t_b(c) \\ &= (\mu_c^d + \sigma_c^d + \epsilon_c^d) \\ &\quad + (\mu_c^b + \sigma_c^b + \epsilon_c^b) \end{aligned} \quad (1)$$

It can be assumed that the planned traversal time $t_p(c)$ is greater than the average observed traversal time μ_c^d to avoid systematic delays. The average traversal time can then be roughly approximated as follows:

$$\hat{\mu}_c^d = t_p(c) * \gamma, \forall c \in C, 0 < \gamma < 1 \quad (2)$$

The ratio γ has to be determined by the user. The standard deviation σ_c^d can be approximated in the same way. It can be assumed that the standard deviation is only a small fraction of the planned traversal time. This yields Equation 3.

$$\hat{\sigma}_c^d = t_p(c) * \eta, \forall c \in C, 0 < \eta < 1, \eta \ll \gamma \quad (3)$$

The **passenger exchange times** for busses and light-rail vehicles can be modeled following the method first proposed in [21]. This method is suitable for high frequency transit systems like urban light-rail and bus transit, where it can be assumed that passengers arrive randomly during the inter-arrival time of two successive vehicles, instead of arriving in bulk shortly before the planned departure time. Furthermore, the method facilitates the modeling of vehicle bunching, i.e. the effect that two vehicles form an undesired platoon because the vehicle in front takes on more passengers than planned and subsequently suffers longer passenger exchange times, while the rear vehicle takes on fewer passengers as planned and thus catches up to the vehicle in front.

If the number $N_{b,s}$ of passengers entering a vehicle b at a stop s , and the average time I_b a passenger takes to enter vehicle b are known, the passenger exchange time $T_{b,s}$ can be determined as follows:

$$T_{b,s} = T_b^{min} + I_b + N_{b,s} \quad (4)$$

Here T_b^{min} describes a vehicle specific minimum time, e.g., for opening and closing the vehicle’s doors. If the passenger arrival rate a_s at stop s is known, $N_{b,s}$ can be modeled dependent on the basic interval $T_{L(b)}$ of line $L(b)$ currently served by vehicle b . With $N_{b,s} = T_{L(b)} * a_s$ the passenger exchange time can then be approximated as shown in Equation 5.

$$T_{b,s} = T_b^{min} + I_b + T_{L(b)} * a_s \quad (5)$$

If instead of the basic interval between vehicles of the same line, simulated headways between successive vehicles servicing the same stop are used, the model becomes dynamic and thus suitable for a simulation model.

If $t_{dep}(b-1, s)$ describes the time a vehicle b 's predecessor has serviced the stop, the passenger exchange time $T_{b,s}(t_{sim})$ can be determined by Equation 6.

$$T_{b,s}(t_{sim}) = \begin{cases} T_b^{min}, & b \text{ is first vehicle at } s \\ T_b^{min} + (t_{sim} - t_{dep}(b-1, s)) * a_s * I_b, & \text{else} \end{cases} \quad (6)$$

3 Results and Discussion

For the model to be practically applicable in the use case described above, transit operators have to be able to execute it quickly: When disaster hits, it is not feasible to wait many hours for first simulated data on the impact of mitigation strategies to come in.

To estimate its execution time, the model was implemented as a Java application [12], and a number of experiments were conducted with representations of the transit network of the authors' hometown of Cologne, Germany. Table 3 depicts the number of simulation events executed per simulation run, while Table 4 depicts the runtime in seconds of the various phases of the simulation run, each for a model of the urban light-rail and the bus network. The preprocessing stage is mainly concerned with reading the model from a database and building up data structures, it has to be run only once independent of the number of simulations runs to be executed. Following each model execution itself a short postprocessing phase serializes the resulting data and releases memory. After all simulation runs have been successfully completed, the application engages in a final and more comprehensive postprocessing phase, reading the results of the individual runs, calculates statistics, assigns them to the relevant entities, and constructs Excel sheets with graphical overviews and detailed reports.

Simulation event type	Light rail	Bus network
DEADHEAD_TRIP_START	1,827	4,080
SERVICE_TRIP_START	1,800	4,080
TRIP_END	3,585	8,150
BOARDING_START	50,470	89,015
BOARDING_END	50,470	89,015
DRIVING_START	60,746	84,951
DRIVING_END	62,913	84,961

Table 3: Average number of main simulation events per simulation run for the light rail and bus networks.

Execution stage	Light rail	Bus network
Preprocessing	6.19	9.31
Model execution	6.77	12.88
Postprocessing per run	0.15	0.30
Postprocessing final	1,270.72	2,229.28
Total runtime (1 run)	1,283.83	2,251.77
Total runtime (100 runs)	1,968.91	3,556.59
Runtime per run (100 runs)	19.69	35.57

Table 4: The simulation application's run time in seconds for the bus and light-rail models, broken down to the common preprocessing step executed only once, the duration of an actual simulation run itself, the postprocessing phase for each run, and the final postprocessing phase only executed once. Assuming the application is used to execute 100 runs, the run time per run amounts to 19.69 seconds for the light-rail model and 35.57 seconds for the larger bus network model.

As seen, the timing requirement is only partially met: While the core model execution itself is concluded in under 7 seconds for the light rail network and under 13 seconds for the much larger bus network, the postprocessing phase with its 1,270 and 2,229 seconds is much too long for the envisioned use case.

Here, instead of compiling comprehensive statistics on all involved model entities, the application has to be reworked to only collect and depict only the statistics most relevant to the operators.

4 Conclusions

This paper presented a bi-modal transit simulation model aimed at supporting public transit operators to increase the resilience of public transit infrastructure. Central aims include to enable operators to evaluate measures against small disturbances and larger outages as they happen, as well as to evaluate what combination of disaster risk management and resilience-building strategies shows most potential to help increasing the resilience of urban transit systems against extreme weather events resulting from climate change as well as other disasters.

The paper discussed the components of public transit infrastructure systems and then went on to present the developed simulation model, focusing on modelling physical components, the logical network, vehicle behaviour, operational decisions, and the necessary randomization.

The discussion of first results showed that the model – implemented as a Java application – works well and executes the core model quickly enough for the stated use cases. However, the currently employed analytical post-processing engine collects a much too comprehensive set of statistics and has to be adapted to prioritize information that is most relevant to transit operators in case of emergencies.

In further research and development steps, after overhauling the statistics engine, the model will be applied to evaluate what combination of disaster risk management and resilience-building strategies shows most potential to help increasing the resilience of urban transit systems against extreme weather events resulting from climate change as well as other disasters.

Acknowledgements

This paper is an updated and extended version of the conference paper “Towards Increasing Resilience of Public Transit Infrastructure – A Bi-Modal Simulation Model” by Daniel Lückerrath and Oliver Ullrich that was published as part of the proceedings of ASIM 2022, 26th Symposium on Simulation Techniques. It has been partially supported by the framework of the European project ARCH – Advancing Resilience of historic areas against Climate-related and other Hazards. This project has received funding from the European Union’s Horizon 2020 research and innovation programme under grant agreement no. 820,999. The sole responsibility for the content of this publication lies with the authors. It does not necessarily represent the opinion of the European Union. Neither the REA nor the European Commission are responsible for any use that may be made of the information contained therein.

References

- [1] Olfert A, et al. Sustainability and resilience - a practical approach to assessing sustainability of infrastructure in the context of climate change. Hutter G, Neubert M, Ortlepp R. Building resilience to natural hazards in the context of climate change - Knowledge integration, implementation, and learning. Springer, 2021.
- [2] Vuchic VR: *Urban Transit - Systems and Technology*. Verlag John Wiley & Sons, Hoboken, New Jersey 2007.
- [3] Behrisch M, Erdmann J, Krajzewicz D. Adding intermodality to the microscopic simulation package SUMO. In: Al-Akaidi, M., editor. MESM’ 2010 – GAMEON-ARABIA’2010. 11th Middle Eastern Simulation Multiconference; 2010 Dec; Alexandria. Alexandria: eurosis. 59-66.
- [4] Kendziorra A, Weber M. Extensions for logistics and public transport in SUMO. In: Behrisch M, Weber M, editors. SUMO 2015 – Intermodal Simulation for Intermodal Transport. 3rd SUMO User Conference; 2015 May. Berlin: Deutsches Zentrum für Luft- und Raumfahrt, Institut für Verkehrssystemtechnik. 83-90.
- [5] Toledo T, Cats O, Burghout W, Koutsopoulos H. Mesoscopic simulation for transit operations. *Transport. Res. C-Emer.* 2010; 18(6): 896-908.
- [6] Suzumura T, Kanezashi H. Multi-modal traffic simulation platform on parallel and distributed systems. In: Tolk A, Diallo S, Ryzhow I, Yilmaz L, Buckley S, Miller J. Proceedings of the 2014 Winter Simulation Conference. *Winter Simulation Conference*; 2014 Dec; Savannah. Piscataway, NJ, USA: IEEE Press. 769-780.
- [7] Suzumura T, McArdle G, Kanezashi, H. A high-performance multi-modal traffic simulation platform and its case study with the Dublin city. In: Yilmaz L, Chan W, Moon I, Roeder T, Macal C, Rossetti M, editors. Proceedings of the 2015 Winter Simulation Conference. *Winter Simulation Conference*; 2015 Dec; Huntington Beach. Piscataway, NJ, USA: IEEE Press. 767-778.
- [8] Burghout W. *Hybrid microscopic-mesoscopic traffic simulation* [dissertation]. Department of Infrastructure, Royal Institute of Technology, Sweden. University of Stockholm, 2004.
- [9] Ullrich O, Proff I, Lückerrath D, Kuckertz P, Speckenmeyer E. Agent-based modeling and simulation of individual traffic as an environment for bus schedule simulation. In: Busch F, Spangler M, editors. ITS for Connected Mobility. *mobil.TUM*; 2014; Munich. Munich: Schriftenreihe des Lehrstuhls für Verkehrstechnik der Technischen Universität München. 89-98.
- [10] Kastner K, Keber R, Pau P, Samal M. Real-Time Traffic Conditions with SUMO for ITS Austria. In: Behrisch M, Knocke M, editors. 1st SUMO User Conference 2013. 1st SUMO User Conference; 2013 May, Berlin. Berlin: Deutsches Zentrum für Luft- und Raumfahrt, Institut für Verkehrssystemtechnik. 43-53.
- [11] Kastner K, Pau P. Experiences with SUMO in a Real-Life Traffic Monitoring System. In: Behrisch M, Weber M, editors. SUMO 2015 – Intermodal Simulation for Intermodal Transport. 3rd SUMO User Conference; 2015 May. Berlin: Deutsches Zentrum für Luft- und Raumfahrt, Institut für Verkehrssystemtechnik. 1-10.
- [12] Lückerrath D: *Ein Simulationsmodell für Öffentlichen Personennahverkehr mit regelbasiertem Verkehrsmanagement* (Dissertation). Institut für Informatik, Universität zu Köln; 2017, 182 pg.
- [13] Ullrich O, Lückerrath D. An Introduction to Discrete-Event Modeling and Simulation. *Simulation Notes Europe (SNE)* 2017; 27(1): 9-16.

- [14] Lückcrath D, Rische N, Speckenmeyer E, Ullrich O. A Mesoscopic Bus Transit Simulation Model Based on Scarce Data. *Simulation Notes Europe (SNE)* 2018; 28(1): 1-10.
- [15] Vossloh Kiepe GmbH. *Elektrische Ausrüstung der Niederflur-Stadtbahnwagen K4000 der Kölner Verkehrs-Betriebe AG 2003*. Druckschrift Nr. 00KV7DE.
- [16] Vossloh Kiepe GmbH. *Elektrische Ausrüstung des Niederflur-Stadtbahnwagens K4500 für die Kölner Verkehrs-Betriebe AG 2003*. Druckschrift Nr. 00KN2DE.
- [17] Vossloh Kiepe GmbH. *Elektrische Ausrüstung der Hochflur-Stadtbahnwagen K5000 der Kölner Verkehrs-Betriebe AG 2003*, Druckschrift Nr. 00KB5DE.
- [18] Lückcrath D, Ullrich O, Kupicha A, Speckenmeyer E. Multi-depot multi-vehicle-type vehicle scheduling for Cologne's tram network. In: Proc. *ASIM-Workshop STS/GMMS 2014*, ARGESIM Report 42, ASIM-Mitteilung AM 149, ARGESIM/ASIM Pub., TU Vienna/Austria, 191-197.
- [19] Lückcrath D, Bogen M, Rome E, Sojeva B, Ullrich O, Worst R, Xie J. Strategies to Mitigate the Impacts of Climate Change Related Events on Public Transit Networks. In: Proc. *24th Symp. Simulationstechnik*, Hamburg, Germany, October 03-04, 2018, 175-182.
- [20] Andersson P, Hermansson A, Tengvald E, Scalia-Tomba G. Analysis and simulation of an urban bus route. *Transport. Res. A-Pol.*, 1979, 13(6): 439-466.
- [21] Chapman R, Michel J. Modelling the Tendency of Buses to Form Pairs. *Transport. Sci.*, 1978, 12(2): 165-175.

Advanced Machine Learning in Recursive Data-based Modelling

Esko K. Juuso

Control Engineering, Environmental and Chemical Engineering, Faculty of Technology, P.O. BOX 4300, 90014 University of Oulu, Finland; esko.juuso@oulu.fi

SNE 32(2), 2022, 113-120, DOI: 10.11128/sne.32.tn.10608
Received: 2021-02-10 (selected EUROSIM 2019 Postconf.
Publication; Revised: 2022-05-30; Accepted: 2022-05-31
SNE - Simulation Notes Europe, ARGESIM Publisher Vienna,
ISSN Print 2305-9974, Online 2306-0271, www.sne-journal.org

Abstract. Recursive data-based modelling is needed for making decision online in varying operating conditions. Recursive algorithms are useful in adapting the parameters within selected memory horizons. Abrupt changes can be handled when the situation change is approved to be drastic. The nonlinear scaling based on generalized norms includes additional alternatives: the norm orders adapt to the gradually changing operating conditions. The drastic shape changes of the scaling functions require full analyses of the orders. The orders can also be stored for different situations and re-used later. Fuzzy inequalities are useful in finding out if the feasible ranges of the most recent period are different from the current active ranges or similar with some of previous feasible ranges. Machine learning is integrated in the system in three levels: (1) finding the appropriate time windows, (2) interactions of feasible levels, and (3) finding decision support when some of feasible ranges need to change. These decisions are supported by expert knowledge. Other model parameters can be included in the analysis. The solution has been tested with measurement data from several application cases. The recursive approach is beneficial in the control and maintenance in varying operating conditions.

Introduction

Models understood as relationships between variables are used for predicting of properties or behaviours of the system. Variable interactions and nonlinearities are important in extending the operation areas of control

and fault diagnosis, where the complexity is alleviated by introducing software sensors [1]. Recursive data-based modelling is needed in varying operating conditions. In industry, where very large datasets have been common already long time, the problem has been tackled by *data analytics* and *intelligent systems*, where linear regression and parametric models are used in the recursive tuning of the interaction equations [2]. Adaptation of the parametric systems is essential in varying operating conditions. Various nonlinear multivariable systems combine statistical and intelligent methodologies with sensor fusion based on data pre-processing, signal processing and feature extraction [3]. Dynamic models are based on additional parametric model structures.

Artificial intelligence (AI) mimic human cognitive functions, including reasoning, knowledge, planning, learning, natural language processing, perception and the ability to move and manipulate objects. *Machine learning (ML)* is a subset of AI: the iterative seeking of solutions is done by using new architectures, techniques and algorithms in order to perform a specific task effectively without using explicit instructions, relying on patterns and inference instead. *artificial neural networks* have been widely used in these studies as a behavioural model to map a systems input to its output regardless of the nature of the system.

Fuzzy logic extends the approximate reasoning, and the connection of fuzzy rule-based systems and expert systems is clear. Fuzzy set systems separate meanings and interactions which is an important key in the adaptation in varying operating conditions. *Linguistic equation (LE)* approach originates from fuzzy set systems: rule sets are replaced with linear equations, and meanings of the variables with nonlinear scaling functions [4]. Constraints handling [5] and data-based analysis [6], facilitate the recursive updates of the systems [7]. The nonlinear scaling revises the meanings and linear models represent the interactions [1].

Table 1: Adaptation level and learning.

Adaptation	Smart adaptive systems	Machine learning
Changing environment	Recursive data analytics for parametric solutions	Statistical techniques, network tuning.
Similar setting, not explicitly ported	Computational intelligence, expertise and data analytics, including variable selection	Data mining utilizing previous experience
New or unknown application	Computational intelligence, expertise and data analytics, including variable selection.	Deep learning with big data ideas.

Statistical analysis with steady state models form the basic elements of different intelligent models. Decomposed systems can be based on weighting the local models with *linear parameter varying (LPV) models* [8]. External dynamic models provide the dynamic behaviour for the LE models developed for a defined sampling interval.

Smart adaptive systems (SAS) are aimed for developing successful applications in different fields by using three levels of adaptation [9]: (1) adaptation to a changing environment, (2) adaptation to a similar setting without explicitly being ported to it, and (3) adaptation to a new or unknown application (Table 1). The recursive analysis is important in all these levels. The smart adaptive data analysis and the data processing form a five-layer advanced deep learning (ADL) platform which supports levels of smart adaptive systems and development of cyber-physical systems (CPS). [2]

Machine learning (ML) is focusing on algorithmic data-based analyses which provide promises for automatic modelling. Performance is good in small scale systems and interesting interactions are found in big data analysis where the previous knowledge is limited. Additional levels bring more challenges for explanations. How far we can go in complex systems? How can we guide the automatic analysis? Different measurements have specific processing requirements [2]. Therefore, the recursive adaptation has application specific requirements.

This article focuses on the possibilities of applying machine learning in data-based modelling. Data analysis (Section 1) is the key part of the modelling. The resulting parametric systems are recursively updated (Section 2) and the solutions are analysed in four different applications (Section 3). The overall system is analysed in Section 4 and conclusions about the applicability of the advanced machine learning in these applications are drawn in Section 5.

1 Data analysis

The main part of the data analysis is variable specific extended with parametric models.

1.1 Variable specific analysis

Machine learning is suitable for the variable specific analysis: features, parameters of the nonlinear scaling functions and intelligent indicators are obtained by using a set of algorithms. Several measurements and sets of features can be analysed in parallel.

Features The arithmetic means and medians are suitable for recursive tuning, but the resulting scaling functions are narrow and sensitive to outliers. More flexible solutions can be obtained with generalized norms defined by

$$\|{}^\tau M_j^p\|_p = (M_j^p)^{1/p} = \left[\frac{1}{N} \sum_{i=1}^N (x_j)_i^p \right]^{1/p}, \quad (1)$$

where the order of the moment $p \in R$ is non-zero, and N is the number of data values obtained in each sample time τ . The norm (1) calculated for variables $x_j, j = 1, \dots, n$, have the same dimensions as the corresponding variables [10]. These norms can be extended to variables including negative values [7]. The norm values are monotonously increasing with the norm order.

The norm values are updated by including new equal sized sub-blocks in calculations since the computation of the norms can be done from the norms obtained for the equal sized sub-blocks, i.e. the norm for several samples can be obtained as the norm of the norms of

the individual samples:

$$\|^{K_s \tau} M_j^p\|_p \left\{ \frac{1}{K_s} \sum_{i=1}^{K_s} [(\tau M_j^p)_i^{1/p}]^p \right\}^{1/p} = \left[\frac{1}{K_s} \sum_{i=1}^{K_s} [(\tau M_j^p)_i]^{1/p} \right]^p, \quad (2)$$

where K_s is the number of samples $\{x_j\}_{i=1}^N$. [10] In automation and data collection systems, the sub-blocks are normally used for arithmetic mean ($p = 1$).

Nonlinear scaling Meanings of the feature or measurement values are represented by using monotonously increasing functions $x_j = f(X_j)$ where x_j is the variable and X_j the corresponding scaled variable. The function $f()$ consist of two second order polynomials, one for the negative values of X_j and one for the positive values, respectively. The corresponding inverse functions $x_j = f^{-1}(X_j)$ based on square root functions are used for scaling to the range $[-2, 2]$. Both functions, $f()$ and $f^{-1}()$, are monotonously increasing. [4, 5]

The parameters of these scaling functions are extracted from measurements by using generalized norms and moments. The support area is defined by the minimum and maximum values of the variable, i.e. the support area is $[\min(x_j), \max(x_j)]$ for each variable $j, j = 1, \dots, m$. The central tendency value, c_j , divides the support area into two parts, and the core area is defined by the central tendency values of the lower and the upper part, $(c_l)_j$ and $(c_h)_j$, correspondingly. This means that the core area of the variable j defined by $[(c_l)_j, (c_h)_j]$ is within the support area. [6] Monotonicity constraints and special requirements are used if needed [5].

The scaling is defined by five parameters which allow highly asymmetric functions, i.e. different shapes for upper and lower parts of the functions. The range $[-2, 2]$ provides a good basis for natural language representations [11]

Intelligent indicators All features and measurements processed with the nonlinear scaling can be used as intelligent indicators. Several indicators can combined and additional indicators, including trends and fluctuations, can be constructed with temporal analysis [12]. *Trend indices*,

$$I_j^T(k) = \frac{1}{n_S + 1} \sum_{i=k-n_S}^k X_j(i) - \frac{1}{n_L + 1} \sum_{i=k-n_L}^k X_j(i), \quad (3)$$

are based on the means obtained for a short and a long time period, defined by delays n_S and n_L , respectively. Time periods are variable specific. The index value represents the strength of both the decrease and increase of the variable x_j . The derivative of the index $I_j^T(k)$, denoted as $\Delta I_j^T(k)$, is used for analyzing triangular episodic representations. Severity of the situation evaluated by a *deviation index*

$$I_j^D(k) = \frac{1}{3} (X_j(k) + I_j^T(k) + \Delta I_j^T(k)). \quad (4)$$

All the indicators are in the range $[-2, 2]$, which facilitates the natural language representation also them [11].

Fluctuation indicators are based on the moving range of variable values obtained as a difference of two moving generalized norms:

$$\Delta x_j^F(k) = \|^{K_s \tau} M_j^{p_h}\|_{p_h} - \|^{K_s \tau} M_j^{p_l}\|_{p_l}, \quad (5)$$

where the orders $p_h \in \mathfrak{R}$ and $p_l \in \mathfrak{R}$ are large positive and negative, respectively. The moments are calculated from the latest $K_s + 1$ values, and an average of several latest values of $\Delta x_j^F(k)$ is used as an indicator of fluctuations. [13]

1.2 Parametric models

The performance of the scaling functions can be analysed by using combinations of several indicators, e.g. the deviation index (4) combines three indicators. The analysis is expanded with models, which have only linear interactions between the indicators. All the scaled variables and linear combinations of them are in the same range $[-2, 2]$ where integer numbers correspond labels, e.g. {very low, low, normal, high, very high}. [11]

2 Recursive analysis

Recursive data analysis facilitates the adaptation of the scaling functions to changing operating conditions, also the orders of the norms are re-analyzed if needed. The existing scaling functions provide a basis for assessing the quality of new data: outliers should be excluded, but the suspicious values may mean that the operating conditions are changing. The scaling functions are extended for analysing outliers and suspicious values to select data for the adaptive scaling. The borders represent the data distribution for different shape factors α_j^+ (Figure 1).

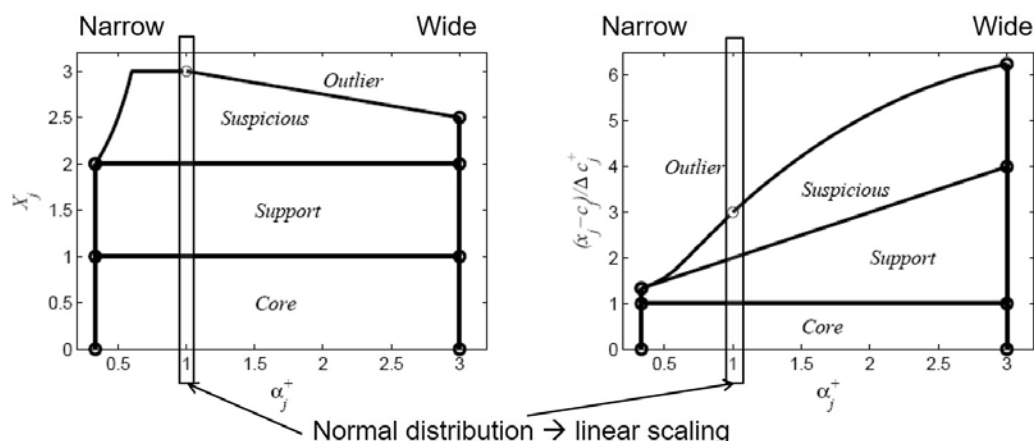


Figure 1: Limits for the core, support, suspicious and outlier areas as a function of shape factor $\alpha_j^+ \in [\frac{1}{3}, 3]$ [14]

The parameters of the nonlinear scaling functions can be recursively updated with (2) by including new equal sized sub-blocks in calculations. The number of samples K_s can be increasing or fixed with some forgetting, and weighting of the individual samples can be used in the analysis. If the definitions should cover all the operating areas, also suspicious values are included as extensions of the support area. In each adaptation step, the acceptable ranges of the shape factors α_j^- and α_j^+ are checked and corrected if needed. The analysis has two levels: the parameters of the scaling functions and the corresponding orders of the norms. [15]

Outliers Clear outliers need to be excluded in both the first analysis and the subsequent recursive steps. In linear scaling, the z-score values outside the range $[-3, 3]$ are often considered as an indication of an outlier (Figure 1). The scaled values are in the range $[-2, 2]$, and this is also the range for the monotonous increase if the minimum and maximum points are obtained from the derivatives of the scaling functions.

Recursive adaptation The parameter of the scaling functions can be recursively updated by using the norms (1) with five defined orders, $(p_{min})_j, (p_l)_j, (p_0)_j, (p_h)_j$ and $(p_{max})_j$, which correspond the corner points of the scaling function. A highly negative and highly positive orders are used instead of *min* and *max*, respectively. Calculations are done in two windows: short and long. If the corner points are not drastically different, the new blocks are included in the calculation of the parameters.

Drastic changes are needed for the corner points if the smooth adaptation does not provide suitable parameters for the new data distribution, i.e. the distribution is changing considerably with new measurements. The orders of the corresponding norms need to be re-analysed. The new situation may require a totally new set of parameters.

Change detectors and decision making Intelligent trend analysis may provide an early indication of the coming changes [12]. Generalised statistical process control (GSPC) notifies if the limits are exceeded more often [16].

3 Applications

The solution has been tested with measurement data from application cases.

3.1 Solar thermal collectors

Solar power plants should collect any available thermal energy in a usable form at the desired temperature range. Irradiation varies considerably between days and on cloudy periods, the variations are very fast and strong variations (Figure 2). The efficient collection requires a fast start-up and reliable operation in the varying cloudy conditions without unnecessary shutdowns and start-ups.

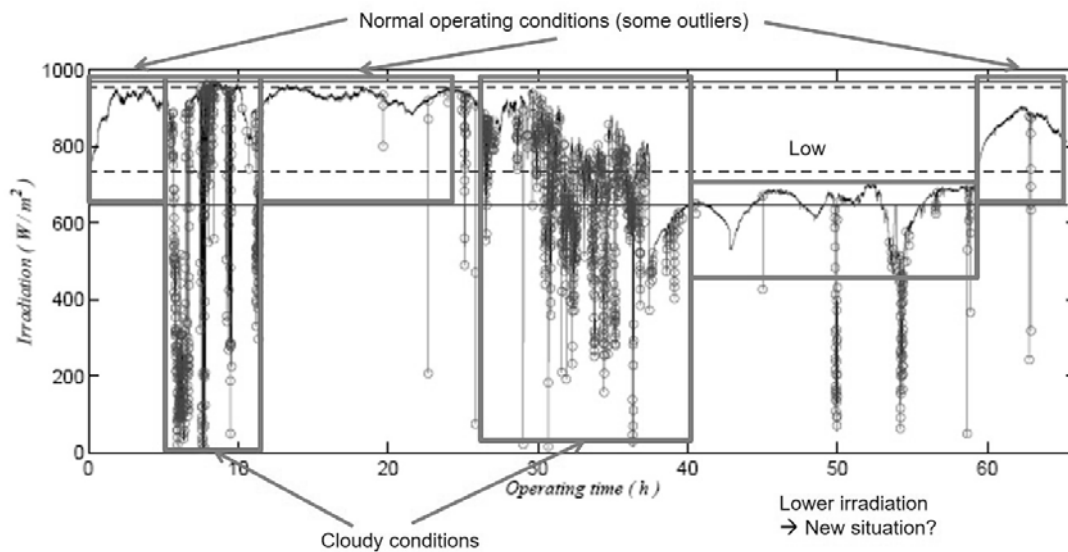


Figure 2: Varying irradiation on a solar collector field: measurements are from 65 hours in 12 days.

The irradiation measurements shown in Figure 2 include typical operating periods. In the first normal period, the feasible area expands until the solar noon is achieved and scaling functions are only slightly modified in the afternoon. The second normal period after cloudy conditions continues from the scaling functions of the first period. The fast dropping single values are considered as outliers which do not affect on the recursive updates of the parameters. This period is followed by a short cloudy situation.

Cloudy periods are detected with the fluctuation indicator (5). The norms are calculated, but they are not used for the recursive updating. In the long cloudy period, the irradiation is fluctuating and the level is going down. The controller limits the acceptable range of control actions by changing the working point in these situations.

After recovering from the cloudy conditions, the situation is compared with the active set of scaling functions which were updated during the second normal period. A new situation is detected: the irradiation is lower than during the previous normal operating conditions. The new set of scaling functions are activated and gradually refined. The parameters of the previous functions are stored for future use. Short cloudy periods disturb operation in this period as well.

The parameters of the first normal period were recovered for the last day of the measurement period.

Trend indices (3) and deviation indices (4) are used for the early detection of changes for adaptive control [17]. For example, the decrease of the irradiation during the long cloudy period.

This research analysed the irradiation measurements. The same methodologies can be used e.g. for the energy demand, temperature difference over the collector field, and properties of the field devices and environment. The machine learning will be used for this extended problem.

3.2 Prognostics

In the prognostics, the range of the scaling functions need to be expanded when new phenomena activate. This is quite typical when wearing progresses. Recursive data analysis has been demonstrated by using root mean square (rms) velocity, v_{rms} , measurements collected from a paper machine: resin problems of a press roll in the felt washer. The scaling functions were recursively updated three times (Figure 3(a)) after expanding the data set by using spline interpolation to get sufficiently long data sets for the recursive predictions (Figure 3(b)) [18]. The system clearly shows the point when decisions are needed. Domain expertise is needed to assess the situation. There are three alternatives: (1) update the scaling functions, (2) change control actions or (3) start maintenance.

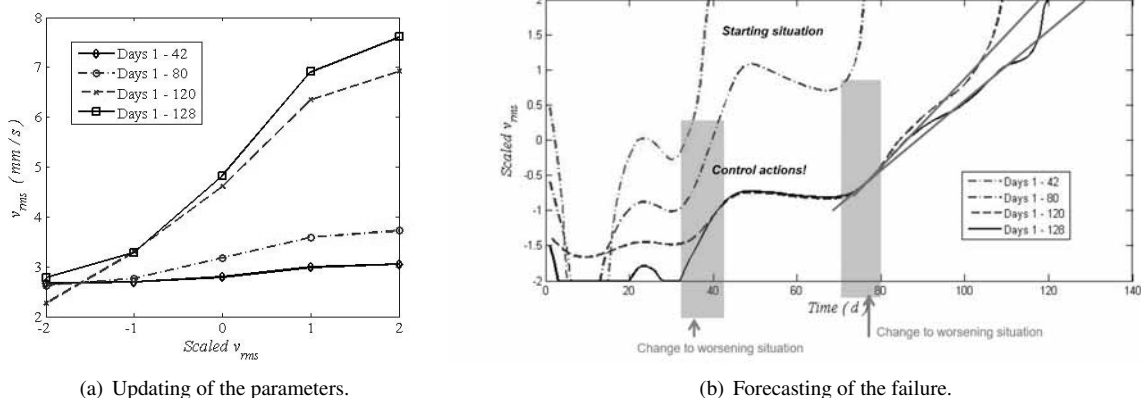


Figure 3: Recursively scaled values of v_{rms} for a press roll of the washer, modified from [18]

The decision is based on the assessment of condition, remaining useful time and alternative schedules of maintenance. The control actions to reduce the speed of wearing are good options. In this case, the operation time was extended and the maintenance was postponed to a better time period. The analysis was extended to uncertainty processing and natural language in [19].

3.3 Wastewater treatment

Biological water treatment depends strongly on the inlet water quality. Load and nutrient should be balanced since both an exceptionally high load and excess nutrients cause problems. The operating conditions are modified by oxygen, temperature and flow. Much slower changes in the biological state drastically influence the purification result and subsequent process phases. Scaled values are used together with intelligent trend indices. [20]

The recursive updates of the scaling functions are important for modelling in different situations. Also, the interaction coefficients can depend on operating conditions. Therefore, the early indications of changes provided by the temporal analysis are beneficial in getting warnings and avoiding alarming situations.

3.4 Fatigue

Fatigue is caused by repeated loading and unloading. The mechanism proceeds through cracks formed when the load exceeded certain thresholds. Structures fracture suddenly when a crack reaches a critical

size. Stress-cycle (S-N) curves, also known as Wöhler curves, are represented by a linguistic equation

$$I_S(k) = \log_{10}(N_C(k)), \tag{6}$$

where the stress index $I_S(k)$ is obtained the stress based on the torque measurements [21]. The scaling of the logarithmic values of the number of cycles, $N_C(k)$, is linear. As the LE model is nonlinear, the LE based S-N curve covers a wide operating range. The continuous model (6) extends the principle of the Palmgren-Miner linear damage hypothesis. In each sample time, τ , the cycles $N_C(k)$ obtained from $I_S(k)$ by (6), and the resulting contribution $\tau/N_C(k)$ is summarised to the previous contributions in the risk analysis. Since the stress is not constant for the whole cycle, the sample time is taken as a fraction of the cycle time. The previous history can be updated whenever the scaling functions are changed. [22]

4 Discussions

Compact linear models enhanced with the nonlinear scaling are used in the selected application cases. Recursive data-based modelling is needed for making decision online in varying operating conditions (Table 2): disturbances, activation of new phenomena, different operating conditions and material properties are taken into account. Recursive algorithms are useful in adapting the parameters within selected memory horizons. Abrupt changes can be handled when the situation change is approved to be drastic.

Table 2: Recursive adaptation in applications.

Application	Phenomena	Recursive analysis
Solar thermal collectors	Daily and seasonal variations	Temporal analysis
Prognostics	Cloudy conditions	Fluctuations
	New phenomena activation	Smoothly extending scaling range
Wastewater treatment	Several operating conditions	Early detection with temporal analysis
Fatigue	Stress scaling	Tuning of risk analysis

Temporal analysis provides early indications in slow processes. Risk analysis is needed to set appropriate labels for the calculation results.

Machine learning is integrated in the system in three levels: (1) finding the appropriate time windows, (2) interactions of the feasible levels, and (3) finding decision support when some feasible ranges need to change. Selecting the time windows, sample times, frequencies and the weights of different indicators are supported by expert knowledge.

In applications, linear interactions can be widely used together with the nonlinear scaling. This does not need to be taken as a limitation, since the approach can be understood as a data pre-processing for any type of nonlinear models, including fuzzy and neural models. Dynamic models are based dynamic structures. All the variables, features and indicators are represented with natural language.

5 Conclusions

The machine learning can focus on the variable specific analysis: algorithms for extracting features, tuning parameters of the nonlinear scaling functions and developing intelligent indicators can be integrated in the machine learning approach. Several measurements and sets of features can be analysed in parallel. The decision-making required in the recursive analysis and the adaptation solutions can be performed within the machine learning. The algorithmic solutions can be improved by using domain expertise and feedback information through other methodologies of computational intelligence.



References

- [1] Juuso EK. Intelligent Methods in Modelling and Simulation of Complex Systems. *Simulation Notes Europe SNE*. 2014;24(1):1–10.
- [2] Juuso E. Smart Adaptive Big Data Analysis with Advanced Deep Learning. *Open Engineering*. 2018; 8(1):403–416.
- [3] Fortuna L, Graziani S, Rizzo A, Xibilia MG. *Soft Sensors for Monitoring and Control of Industrial Processes*. Advances in Industrial Control. New York: Springer. 2007. 270 pp.
- [4] Juuso EK. Integration of Intelligent Systems in Development of Smart Adaptive Systems. *International Journal of Approximate Reasoning*. 2004; 35(3):307–337.
- [5] Juuso EK. Tuning of Large-Scale Linguistic Equation (LE) Models with Genetic Algorithms. In: *Revised selected papers of the International Conference on Adaptive and Natural Computing Algorithms - ICANNGA 2009, Kuopio, Finland, Lecture Notes in Computer Science*, edited by Kolehmainen M, vol. LNCS 5495, pp. 161–170. Heidelberg: Springer-Verlag. 2009;.
- [6] Juuso E, Lahdelma S. Intelligent scaling of features in fault diagnosis. In: *7th International Conference on Condition Monitoring and Machinery Failure Prevention Technologies, CM 2010 - MFPT 2010, 22-24 June 2010, Stratford-upon-Avon, UK*, vol. 2. 2010; pp. 1358–1372.
- [7] Juuso EK. Recursive Tuning of Intelligent Controllers of Solar Collector Fields in Changing Operating Conditions. In: *Proceedings of the 18th World Congress The International Federation of Automatic Control, Milano (Italy) August 28 - September 2, 2011*, edited by Bittani S, Cenedese A, Zampieri S, pp. 12282–12288. IFAC. 2011;.
- [8] Ljung L. Perspectives on system identification. In: *Plenary papers, milestone reports & selected survey*




- papers, 17th IFAC World Congress, Seoul, Korea, July 6-11, 2008*, edited by Chung MJ, Misra P, pp. 47–59. IFAC. 2008;<http://www.ifac-papersonline.net/>.
- [9] Anguita D. Smart Adaptive Systems - State of the Art and Future Directions for Research. In: *Proceedings of Eunite 2001 - European Symposium on Intelligent Technologies, Hybrid Systems and their implementation on Smart Adaptive Systems, July 13-14, 2001, Tenerife, Spain*, pp. 1–4. Aachen: Wissenschaftsverlag Mainz. 2001;.
- [10] Lahdelma S, Juuso E. Signal processing and feature extraction by using real order derivatives and generalised norms. Part 1: Methodology. *International Journal of Condition Monitoring*. 2011;1(2):46–53.
- [11] Juuso EK. Informative process monitoring with a natural language interface. In: *2016 UKSim-AMSS 18th International Conference on Modelling and Simulation, 6-8 April, 2016, Cambridge, UK*, pp. 105–110. IEEE Computer Society. 2016;.
- [12] Juuso EK. Intelligent Trend Indices in Detecting Changes of Operating Conditions. In: *2011 UKSim 13th International Conference on Modelling and Simulation*, pp. 162–167. IEEE Computer Society. 2011;.
- [13] Juuso EK. Model-based Adaptation of Intelligent Controllers of Solar Collector Fields. In: *Proceedings of 7th Vienna Symposium on Mathematical Modelling, February 14-17, 2012, Vienna, Austria, Part 1*, edited by Troch I, Breitenecker F, vol. 7, pp. 979–984. IFAC. 2012;.
- [14] Juuso E. Integration of intelligent systems in development of smart adaptive systems: linguistic equation approach. Ph.D. thesis, University of Oulu. 2013. 258 pp., <http://urn.fi/urn:isbn:9789526202891>.
- [15] Juuso EK. Recursive Dynamic Modelling in Changing Operating Conditions. In: *Proceedings of the 56th Conference on Simulation and Modelling (SIMS 56), October, 7-9, 2015, Linköping University, Sweden*. Linköping, Sweden: Linköping University Electronic Press. 2015; pp. 169–174.
- [16] Juuso EK. Generalised statistical process control GSPC in stress monitoring. *IFAC-PapersOnline*. 2015; 48(17):207–212.
- [17] Juuso E. Intelligent trend analysis for a solar thermal energy collector field. vol. 136. 2018; .
- [18] Juuso EK. Recursive Data Analysis and Modelling in Prognostics. In: *12th International Conference on Condition Monitoring and Machinery Failure Prevention Technologies, CM 2015 - MFPT 2015, 9-11 June 2015, Oxford, UK*, pp. 560–567. BINDT. 2015; ISBN: 978-1-5108-0712-9. URL www.proceedings.com
- [19] Juuso EK. Intelligent Performance Analysis with a Natural Language Interface. *Management Systems in Production Engineering*. 2017;25(3):168–175.
- [20] Juuso EK. Data-based development of dynamic models for biological wastewater treatment in pulp and paper industry. In: *SIMS 2010 Proceedings, The 51st Conference on Modelling and Simulation, Oulu, 14-15 October, 2010*. 2010;9 pp.
- [21] Juuso EK, Ruusunen M. Stress Indices in Fatigue Prediction. In: *International Conference on Maintenance, Condition Monitoring and Diagnostics, and Maintenance Performance Measurement and Management, MCMD 2015 & MPMM 2015, Oulu, Finland. 30 September - 1 October 2015*. Oulu, Finland: POHTO. 2015;8 pp., ISBN 978-951-98113-7-6.
- [22] Juuso EK. Advanced prognostics based on intelligent data analysis. In: *WCCM 2017 - 1st World Congress on Condition Monitoring 2017*, vol. 2. Red Hook, NY: Curran Associates. 2017; pp. 782–794.

SNE Simulation News

EUROSIM Data and Quick Info

VESS – Virtual EUROSIM Seminar
Virtual Simulation Presentations, since June 2020 www.eurosim2023.eu

MATHMOD Vienna 2022
July 27-29, 2022, Vienna, Austria www.mathmod.at
ASIM 2022 - 26. Symposium Simulation Technique
July 25-27, 2022, Vienna, Austria www.asim-gi.org/asim2022




EUROSIM CONGRESS 2023
June 28-30, 2023, Amsterdam, The Netherlands www.eurosim2023.eu

Contents

Short Info EUROSIM	N2
Short Info ASIM, CEA-SMSG	N3
Short Info CSSS, DBSS, LIOPHANT, LSS	N4
Short Info KA-SIM, NSSM, PSCS	N5
Short Info SIMS, SLOSIM, UKSIM	N6
Short Info ROMSIM, Albanian Society	N7
Short Info ARGESIM, SNE	N8
EUROSIM Conferences & Seminars	Back Cover

Simulation Notes Europe SNE is the official membership journal of EUROSIM and distributed / available to members of the EUROSIM Societies as part of the membership benefits.

If you have any information, announcement, etc. you want to see published, please contact a member of the editorial board in your country or the editorial office. For scientific publications, please contact the EiC.

This *EUROSIM Data & Quick Info* compiles data from EUROSIM societies and groups: addresses, weblinks, and officers of societies with function and email, to be published regularly in SNE issues. This information is also published at EUROSIM's website www.eurosim.info.

SNE Reports Editorial Board

- EUROSIM Miguel Mujica Mota, m.mujica.mota@hva.nl
P. M. Scala, p.m.scala@hva.nl
ASIM A. Körner, andreas.koerner@tuwien.ac.at
CEA-SMSG José L. Pitarch, jlpitarch@isa.upv.es
CSSS Mikuláš Alexík, alexik@frtk.utc.sk
DBSS M. Mujica Mota, m.mujica.mota@hva.nl
LIOPHANT F. Longo, f.longo@unical.it
LSS Juri Tolujew, Juri.Tolujew@iff.fraunhofer.de
KA-SIM Edmond Hajrizi, info@ka-sim.com
NSSM Y. Senichenkov, senyb@den.icc.spbstu.ru
PSCS Zenon Sosnowski, zenon@ii.pb.bialystok.pl
SIMS Esko Juuso, esko.juuso@oulu.fi
SLOSIM Vito Logar, vito.logar@fe.uni-lj.si
UKSIM David Al-Dabass, david.al-dabass@ntu.ac.uk
ROMSIM Constanta Zoe Radulescu, zoe@ici.ro
ALBSIM Majlinda Godolja, majlinda.godolja@feut.edu.al

SNE Editorial Office /ARGESIM

→ www.sne-journal.org, www.eurosim.info

✉ office@sne-journal.org, eic@sne-journal.org

✉ SNE Editorial Office

Johannes Tanzler (Layout, Organisation)
Irmgard Husinsky (Web, Electronic Publishing)
Felix Breitenecker EiC (Organisation, Authors)
ARGESIM/Math. Modelling & Simulation Group,
Inst. of Analysis and Scientific Computing, TU Wien
Wiedner Hauptstrasse 8-10, 1040 Vienna, Austria



EUROSIM Federation of European Simulation Societies

General Information. EUROSIM, the Federation of European Simulation Societies, was set up in 1989. The purpose of EUROSIM is to provide a European forum for simulation societies and groups to promote modelling and simulation in industry, research, and development – by publication and conferences. → www.eurosim.info

Member Societies. EUROSIM members may be national simulation societies and regional or international societies and groups dealing with modelling and simulation. At present EUROSIM has *Full Members* and *Observer Members* (*), and *Member Candidates* (**).

ASIM	Arbeitsgemeinschaft Simulation <i>Austria, Germany, Switzerland</i>
CEA-SMSG	Spanish Modelling and Simulation Group; <i>Spain</i>
CSSS	Czech and Slovak Simulation Society <i>Czech Republic, Slovak Republic</i>
DBSS	Dutch Benelux Simulation Society <i>Belgium, Netherlands</i>
KA-SIM	Kosovo Simulation Society, <i>Kosovo</i>
LIOPHANT	LIOPHANT Simulation Club; <i>Italy & International</i>
LSS	Latvian Simulation Society; <i>Latvia</i>
PSCS	Polish Society for Computer Simulation; <i>Poland</i>
NSSM	Russian National Simulation Society <i>Russian Federation</i>
SIMS	Simulation Society of Scandinavia <i>Denmark, Finland, Norway, Sweden</i>
SLOSIM	Slovenian Simulation Society; <i>Slovenia</i>
UKSIM	United Kingdom Simulation Society <i>UK, Ireland</i>
ALBSIM	Albanian Simulation Society*; <i>Albania</i>
ROMSIM	Romanian Society for Modelling and Simulation*; <i>Romania</i>
Societies in Re-Organisation:	
CROSSIM	<i>Croatian Society f. Simulation Modeling; Croatia</i>
FRANCO-SIM	<i>Société Francophone de Simulation Belgium, France</i>
HSS	<i>Hungarian Simulation Society; Hungary</i>
ISCS	<i>Italian Society for Computer Simulation, Italy</i>

EUROSIM Board / Officers. EUROSIM is governed by a board consisting of one representative of each member society, and president, past president, and SNE representative. The President is nominated by the society organising the next EUROSIM Congress. Secretary, and Treasurer are elected out of members of the board.

President	M. Mujica Mota (DBSS), <i>m.mujica.mota@hva.nl</i>
Past President	Emilio Jiménez (CAE-SMSG), <i>emilio.jimenez@unirioja.es</i>
Secretary	P. M. Scala, <i>p.m.scala@hva.nl</i>
Treasurer	Felix Breitenecker (ASIM) <i>felix.breitenecker@tuwien.ac.at</i>
Webmaster	Irmgard Husinsky, <i>irmgard.husinsky@tuwien.ac.at</i>
SNE Editor	F. Breitenecker, <i>eic@sne-journal.org</i>

SNE – Simulation Notes Europe. SNE is EUROSIM's scientific journal with peer reviewed contributions as well as a membership journal for EUROSIM with information from the societies. EUROSIM societies distribute SNE (electronic or printed) to their members as official membership journal. SNE Publishers are EUROSIM, ARGESIM and ASIM.

SNE	Felix Breitenecker
Editor-in-Chief	<i>eic@sne-journal.org</i>

→ www.sne-journal.org,  office@sne-journal.org

EUROSIM Congress and Conferences.

Each year a major EUROSIM event takes place, the EUROSIM CONGRESS organised by a member society, SIMS EUROSIM Conference, and MATHMOD Vienna Conference (ASIM).

EUROSIM Congress 2019, the 10th EUROSIM Congress, was organised by CEA-SMSG, the Spanish Simulation Society, in La Rioja, Logroño, Spain, July 1-5, 2019;

Due to Covid-19 virus some EUROSIM events had to be cancelled in 2020 or 2021, resp. To bridge this gap, EUROSIM is organising the series VESS - Virtual EUROSIM Simulation Seminar – seminars by simulation professionalists (2 hours via web), in preparation for upcoming EUROSIM events. → www.eurosim2023.eu

Next main event is MATHMOD Vienna. This triennial EUROSIM Conference is mainly organized by ASIM, the German simulation society, and ARGESIM, with main co-sponsor IFAC.

MATHMOD 2022, the 10th MATHMOD Vienna Conference on Mathematical Modelling will take place in Vienna, July 27-29, 2022. → www.mathmod.at

EUROSIM Congress 2023, the 11th EUROSIM Congress, will be organised by DBSS, the Dutch Benelux simulation society, in Amsterdam, June 28-30, 2023.

→ www.eurosim2023.eu

Furthermore, EUROSIM Societies organize also local conferences, and EUROSIM co-operates with the organizers of the I3M Conference Series.

→ www.liophant.org/conferences/



EUROSIM Member Societies



ASIM
German Simulation Society
Arbeitsgemeinschaft Simulation

ASIM (Arbeitsgemeinschaft Simulation) is the association for simulation in the German speaking area, servicing mainly Germany, Switzerland and Austria. ASIM was founded in 1981 and has now about 400 individual members (including associated), and 90 institutional or industrial members.

→ www.asim-gi.org with members' area

✉ info@asim-gi.org, admin@asim-gi.org

✉ ASIM – Inst. of Analysis and Scientific Computing
 Vienna University of Technology (TU Wien)
 Wiedner Hauptstraße 8-10, 1040 Vienna, Austria

ASIM Officers

President	Felix Breiteneker felix.breiteneker@tuwien.ac.at
Vice presidents	Sigrid Wenzel, s.wenzel@uni-kassel.de T. Pawletta, thorsten.pawletta@hs-wismar.de A. Körner, andreas.koerner@tuwien.ac.at
Secretary	Ch. Deatcu, christina.deatcu@hs-wismar.de I. Husinsky, Irmgard.husinsky@tuwien.ac.at
Membership Affairs	S. Wenzel, s.wenzel@uni-kassel.de Ch. Deatcu, christina.deatcu@hs-wismar.de F. Breiteneker, felix.breiteneker@tuwien.ac.at
Repr. EUROSIM	F. Breiteneker, felix.breiteneker@tuwien.ac.at A. Körner, andreas.koerner@tuwien.ac.at
Internat. Affairs – GI Contact	O. Rose, Oliver.Rose@tu-dresden.de N. Popper, niki.popper@dwh.at
Editorial Board SNE	T. Pawletta, thorsten.pawletta@hs-wismar.de Ch. Deatcu, christina.deatcu@hs-wismar.de
Web EUROSIM	I. Husinsky, Irmgard.husinsky@tuwien.ac.at

Last data update April 2020

ASIM is organising / co-organising the following international conferences:

- ASIM SPL Int. Conference 'Simulation in Production and Logistics' – biannual
- ASIM SST 'Symposium Simulation Technique' – biannual
ASIM SST 2022: TU Vienna, July 25-27, 2022
www.asim-gi.org/asim2022
- MATHMOD Int. Vienna Conference on Mathematical Modelling – triennial

Furthermore, ASIM is co-sponsor of WSC - Winter Simulation Conference, of SCS conferences *SpringSim* and *SummerSim*, and of *IBM* and *Simutech* conference series.

ASIM Working Committees

GMMS	Methods in Modelling and Simulation Th. Pawletta, thorsten.pawletta@hs-wismar.de
SUG	Simulation in Environmental Systems Jochen Wittmann, wittmann@informatik.uni-hamburg.de
STS	Simulation of Technical Systems Walter Commerell, commerell@hs-ulm.de
SPL	Simulation in Production and Logistics Sigrid Wenzel, s.wenzel@uni-kassel.de
Edu	Simulation in Education/Education in Simulation A. Körner, andreas.koerner@tuwien.ac.at
Big DATA	Working Group Data-driven Simulation in Life Sciences; niki.popper@dwh.at
WORKING GROUPS	Simulation in Business Administration, in Traffic Systems, for Standardisation, etc.

CEA-SMSG – Spanish Modelling and Simulation Group

CEA is the Spanish Society on Automation and Control and it is the national member of IFAC (International Federation of Automatic Control) in Spain. Since 1968 CEA-IFAC looks after the development of the Automation in Spain, in its different issues: automatic control, robotics, *SIMULATION*, etc. The association is divided into national thematic groups, one of which is centered on Modeling, Simulation and Optimization, constituting the CEA Spanish Modeling and Simulation Group (CEA-SMSG). It looks after the development of the Modelling and Simulation (M&S) in Spain, working basically on all the issues concerning the use of M&S techniques as essential engineering tools for decision-making and optimization.

→ <http://www.ceautomatica.es/grupos/>

→ emilio.jimenez@unirioja.es
simulacion@cea-ifac.es

✉ CEA-SMSG / Emilio Jiménez, Department of Electrical Engineering, University of La Rioja, San José de Calasanz 31, 26004 Logroño (La Rioja), SPAIN

CEA - SMSG Officers

President	José L. Pitarch, jlpitarch@isa.upv.es
Vice president	Juan Ignacio Latorre, juanignacio.latorre@unavarra.es
Repr. EUROSIM	Emilio Jiménez, emilio.jimenez@unirioja.es
Edit. Board SNE	Juan Ignacio Latorre, juanignacio.latorre@unavarra.es
Web EUROSIM	Mercedes Perez mercedes.perez@unirioja.es

Last data update May 2022



CSSS – Czech and Slovak Simulation Society

CSSS -The *Czech and Slovak Simulation Society* has about 150 members working in Czech and Slovak national scientific and technical societies (*Czech Society for Applied Cybernetics and Informatics*, *Slovak Society for Applied Cybernetics and Informatics*). CSSS main objectives are: development of education and training in the field of modelling and simulation, organising professional workshops and conferences, disseminating information about modelling and simulation activities in Europe. Since 1992, CSSS is full member of EUROSIM.

→ www.fit.vutbr.cz/CSSS

✉ snorek@fel.cvut.cz

✉ CSSS / Miroslav Šnorek, CTU Prague
FEE, Dept. Computer Science and Engineering,
Karlovo nám. 13, 121 35 Praha 2, Czech Republic

CSSS Officers

President	Miroslav Šnorek, snorek@fel.cvut.cz
Vice president	Mikuláš Alexik, alexik@frtk.fri.utc.sk
Scientific Secr.	A. Kavička, Antonin.Kavicka@upce.cz
Repr. EUROSIM	Miroslav Šnorek, snorek@fel.cvut.cz
Edit. Board SNE	Mikuláš Alexik, alexik@frtk.fri.utc.sk
Web EUROSIM	Petr Peringer, peringer@fit.vutbr.cz

Last data update December 2012

DBSS – Dutch Benelux Simulation Society

The *Dutch Benelux Simulation Society* (DBSS) was founded in July 1986 in order to create an organisation of simulation professionals within the Dutch language area. DBSS has actively promoted creation of similar organisations in other language areas. DBSS is a member of EUROSIM and works in close cooperation with its members and with affiliated societies.

→ www.DutchBSS.org

✉ a.w.heemink@its.tudelft.nl

✉ DBSS / A. W. Heemink
Delft University of Technology, ITS - twi,
Mekelweg 4, 2628 CD Delft, The Netherlands

DBSS Officers

President	M. Mujica Mota, m.mujica.mota@hva.nl
Vice president	A. Heemink, a.w.heemink@its.tudelft.nl
Treasurer	A. Heemink, a.w.heemink@its.tudelft.nl
Secretary	P. M. Scala, p.m.scala@hva.nl
Repr. EUROSIM	M. Mujica Mota, m.mujica.mota@hva.nl
Edit. SNE/Web	M. Mujica Mota, m.mujica.mota@hva.nl

Last data update June 2016



LIOPHANT Simulation

Liophant Simulation is a non-profit association born in order to be a trait-d'union among simulation developers and users; Liophant is devoted to promote and diffuse the simulation techniques and methodologies; the Association promotes exchange of students, sabbatical years, organization of International Conferences, courses and internships focused on M&S applications.

→ www.liophant.org

✉ info@liophant.org

✉ LIOPHANT Simulation, c/o Agostino G. Bruzzone,
DIME, University of Genoa, Savona Campus
via Molinero 1, 17100 Savona (SV), Italy

LIOPHANT Officers

President	A.G. Bruzzone, agostino@itim.unige.it
Director	E. Bocca, enrico.bocca@liophant.org
Secretary	A. Devoti, devoti.a@iveco.com
Treasurer	Marina Massei, massei@itim.unige.it
Repr. EUROSIM	A.G. Bruzzone, agostino@itim.unige.it
Deputy	F. Longo, f.longo@unica.it
Edit. Board SNE	F. Longo, f.longo@unica.it
Web EUROSIM	F. Longo, f.longo@unica.it

Last data update June 2016

LSS – Latvian Simulation Society

The Latvian Simulation Society (LSS) has been founded in 1990 as the first professional simulation organisation in the field of Modelling and simulation in the post-Soviet area. Its members represent the main simulation centres in Latvia, including both academic and industrial sectors.

→ www.itl.rtu.lv/imb/

✉ Egils.Ginters@rtu.lv

✉ Prof. Egils Ginters, Kirshu Str.13A, Cesis LV-4101,
Latvia

LSS Officers

President	Yuri Merkurjev, merkur@itl.rtu.lv
Vice President	Egils Ginters, egils.ginters@rtu.lv
Secretary	Artis Teilans, artis.teilans@rta.lv
Repr. EUROSIM	Egils Ginters, egils.ginters@rtu.lv
Deputy	Artis Teilans, artis.teilans@rta.lv
Edit. Board SNE	Juri Tolujew, Juri.Tolujew@iff.fraunhofer.de
Web EUROSIM	Vitaly Bolshakov, vitalijs.bolsakovs@rtu.lv

Last data update November 2020



KA-SIM Kosovo Simulation Society

Kosova Association for Modeling and Simulation (KA-SIM, founded in 2009), is part of Kosova Association of Control, Automation and Systems Engineering (KA-CASE). KA-CASE was registered in 2006 as non Profit Organization and since 2009 is National Member of IFAC – International Federation of Automatic Control. KA-SIM joined EUROSIM as Observer Member in 2011. In 2016, KA-SIM became full member.

KA-SIM has about 50 members, and is organizing the international conference series International Conference in Business, Technology and Innovation, in November, in Durrhës, Albania, and IFAC Simulation Workshops in Pristina.

→ www.ubt-uni.net/ka-case

✉ ehajrizi@ubt-uni.net

✉ MOD&SIM KA-CASE; Att. Dr. Edmond Hajrizi
Univ. for Business and Technology (UBT)
Lagjja Kalabria p.n., 10000 Prishtina, Kosovo

KA-SIM Officers

President	Edmond Hajrizi, ehajrizi@ubt-uni.net
Vice president	Muzafer Shala, info@ka-sim.com
Secretary	Lulzim Beqiri, info@ka-sim.com
Treasurer	Selman Berisha, info@ka-sim.com
Repr. EUROSIM	Edmond Hajrizi, ehajrizi@ubt-uni.net
Deputy	Muzafer Shala, info@ka-sim.com
Edit. Board SNE	Edmond Hajrizi, ehajrizi@ubt-uni.net
Web EUROSIM	Betim Gashi, info@ka-sim.com

Last data update December 2016

NSSM – National Society for Simulation Modelling (Russia)

NSSM - The Russian National Simulation Society (Национальное Общество Имитационного Моделирования – НОИМ) was officially registered in Russian Federation on February 11, 2011. In February 2012 NSS has been accepted as an observer member of EUROSIM, and in 2015 NSSM has become full member.

→ www.simulation.su

✉ yusupov@iias.spb.su

✉ NSSM / R. M. Yusupov,
St. Petersburg Institute of Informatics and Automation
RAS, 199178, St. Petersburg, 14th lin. V.O, 39

NSSM Officers

President	R. M. Yusupov, yusupov@iias.spb.su
Chair Man. Board	A. Plotnikov, plotnikov@sstc.spb.ru
Secretary	M. Dolmatov, dolmatov@simulation.su
Repr. EUROSIM	R.M. Yusupov, yusupov@iias.spb.su Y. Senichenkov, senyb@dcn.icc.spbstu.ru
Deputy	B. Sokolov, sokol@iias.spb.su
Edit. Board SNE	Y. Senichenkov, senyb@mail.ru , senyb@dcn.icc.spbstu.ru ,

Last data update February 2018

PSCS – Polish Society for Computer Simulation

PSCS was founded in 1993 in Warsaw. PSCS is a scientific, non-profit association of members from universities, research institutes and industry in Poland with common interests in variety of methods of computer simulations and its applications. At present PSCS counts 257 members.

→ www.eurosim.info, www.ptsk.pl

✉ leon@ibib.waw.pl

✉ PSCS / Leon Bobrowski, c/o IBIB PAN,
ul. Trojdena 4 (p.416), 02-109 Warszawa, Poland

PSCS Officers

President	Tadeusz Nowicki, Tadeusz.Nowicki@wat.edu.pl
Vice president	Leon Bobrowski, leon@ibib.waw.pl
Treasurer	Z. Sosnowski, zenon@ii.pb.bialystok.pl
Secretary	Zdzisław Galkowski, Zdzislaw.Galkowski@simr.pw.edu.pl
Repr. EUROSIM	Leon Bobrowski, leon@ibib.waw.pl
Deputy	Tadeusz Nowicki, tadeusz.nowicki@wat.edu.pl
Edit. Board SNE	Zenon Sosnowski, z.sosnowski@pb.edu.pl
Web EUROSIM	Magdalena Topczewska m.topczewska@pb.edu.pl

Last data update May 2022



SIMS – Scandinavian Simulation Society

SIMS is the *Scandinavian Simulation Society* with members from the five Nordic countries Denmark, Finland, Iceland, Norway and Sweden. The SIMS history goes back to 1959. SIMS practical matters are taken care of by the SIMS board consisting of two representatives from each Nordic country (Iceland one board member).

SIMS Structure. SIMS is organised as federation of regional societies. There are **FinSim** (Finnish Simulation Forum), **MoSis** (Society for Modelling and Simulation in Sweden), **DKSIM** (Dansk Simuleringsforening) and **NFA** (Norsk Forening for Automatisering).

→ www.scansims.org

✉ bernt.lie@usn.no

✉ SIMS / Bernt Lie, Faculty of Technology, Univ.College of Southeast Norway, Department of Technology, Kjølnes ring 56, 3914 Porsgrunn, Norway

SIMS Officers

President	Tiina Komulainen, tiina.komulainen@oslomet.no
Vice president	Erik Dahlquist, erik.dahlquist@mdh.se
Treasurer	Vadim Engelson, vadime@mathcore.com
Repr. EUROSIM	Esko Juuso, esko.juuso@oulu.fi
Edit. Board SNE	Esko Juuso, esko.juuso@oulu.fi
Web EUROSIM	Vadim Engelson, vadime@mathcore.com

Last data update May 2022



SLOSIM – Slovenian Society for Simulation and Modelling

SLOSIM - Slovenian Society for Simulation and Modelling was established in 1994 and became the full member of EUROSIM in 1996. Currently it has 90 members from both Slovenian universities, institutes, and industry. It promotes modelling and simulation approaches to problem solving in industrial as well as in academic environments by establishing communication and cooperation among corresponding teams.

→ www.slosim.si

✉ slosim@fe.uni-lj.si

✉ SLOSIM / Vito Logar, Faculty of Electrical Engineering, University of Ljubljana, Tržaška 25, 1000 Ljubljana, Slovenia

SLOSIM Officers

President	Vito Logar, vito.logar@fe.uni-lj.si
Vice president	Božidar Šarler, bozidar.sarler@ung.si
Secretary	Simon Tomažič, simon.tomazic@fe.uni-lj.si
Treasurer	Milan Simčič, milan.simcic@fe.uni-lj.si
Repr. EUROSIM	B. Zupančič, borut.zupancic@fe.uni-lj.si
Deputy	Vito Logar, vito.logar@fe.uni-lj.si
Edit. Board SNE	R. Karba, rihard.karba@fe.uni-lj.si
Web EUROSIM	Vito Logar, vito.logar@fe.uni-lj.si

Last data update December 2018

UKSIM - United Kingdom Simulation Society

The UK Simulation Society is very active in organizing conferences, meetings and workshops. UKSim holds its annual conference in the March-April period. In recent years the conference has always been held at Emmanuel College, Cambridge. The Asia Modelling and Simulation Section (AMSS) of UKSim holds 4-5 conferences per year including the EMS (European Modelling Symposium), an event mainly aimed at young researchers, organized each year by UKSim in different European cities. Membership of the UK Simulation Society is free to participants of any of our conferences and their co-authors.

→ uksim.info

✉ david.al-dabass@ntu.ac.uk

✉ UKSIM / Prof. David Al-Dabass
Computing & Informatics,
Nottingham Trent University
Clifton lane, Nottingham, NG11 8NS, United Kingdom
UKSIM Officers

President	David Al-Dabass, david.al-dabass@ntu.ac.uk
Secretary	T. Bashford, tim.bashford@uwtsd.ac.uk
Treasurer	D. Al-Dabass, david.al-dabass@ntu.ac.uk
Membership chair	G. Jenkins, glenn.l.jenkins@smu.ac.uk
Local/Venue chair	Richard Cant, richard.cant@ntu.ac.uk
Repr. EUROSIM	Dr Taha Osman, taha.osman@ntu.ac.uk
Deputy	T. Bashford, tim.bashford@uwtsd.ac.uk
Edit. Board SNE	D. Al-Dabass, david.al-dabass@ntu.ac.uk

Last data update March 2020



EUROSIM Observer Members

ROMSIM – Romanian Modelling and Simulation Society

ROMSIM has been founded in 1990 as a non-profit society, devoted to theoretical and applied aspects of modelling and simulation of systems.

→ www.eurosim.info/societies/romsim/

✉ florin_h2004@yahoo.com

✉ ROMSIM / Florin Hartescu,
National Institute for Research in Informatics, Averescu
Av. 8 – 10, 011455 Bucharest, Romania

ROMSIM Officers

President	N. N.
Vice president	Florin Hartescu, florin_h2004@yahoo.com Marius Radulescu, mradulescu.csmro@yahoo.com
Repr. EUROSIM	Marius Radulescu
Deputy	Florin Hartescu
Edit. Board SNE	Constanta Zoe Radulescu, zoe@ici.ro
Web EUROSIM	Florin Hartescu

Last data update June 2019

ALBSIM – Albanian Simulation Society

The Albanian Simulation Society has been initiated at the Department of Statistics and Applied Informatics, Faculty of Economy at the University of Tirana, by Prof. Dr. Kozeta Sevrani. The society is involved in different international and local simulation projects, and is engaged in the organisation of the conference series ISTI - Information Systems and Technology. In July 2019 the society was accepted as EUROSIM Observer Member.

→ www.eurosim.info/societies/albsim/

✉ kozeta.sevrani@unitir.edu.al

✉ Albanian Simulation Goup, attn. Kozeta Sevrani
University of Tirana, Faculty of Economy
rr. Elbasanit, Tirana 355 Albania

Albanian Simulation Society- Officers

Chair Kozeta Sevrani,
kozeta.sevrani@unitir.edu.al

Repr. EUROSIM Kozeta Sevrani

Edit. Board SNE Albana Gorishti,
albana.gorishti@unitir.edu.al
Majlinda Godolja,
majlinda.godolja@feut.edu.al

Last data update July 2019

Societies in Re-organisation / Former Societies

The following societies are at present inactive or under re-organisation:

- CROSSIM – *Croatian Society for Simulation Modelling*
Contact: Tarzan Legović, Tarzan.Legovic@irb.hr
- FRANCOSIM – Société Francophone de Simulation
- HSS – Hungarian Simulation Society
- ISCS – Italian Society for Computer Simulation

The following societies have been formally terminated:

- MIMOS – Italian Modeling & Simulation Association; terminated end of 2020.

HSS – Hungarian Simulation Society

There are plans to reactivate Hungarian Simulation Society. M. Mujica Mota EUROSIM President, is in contact with András Gábor, Head of the Dean's office at the Faculty of International Management and Business of Budapest Business School University of Applied Sciences (BBS). We ask interested people to contact Mr. Gábor, andrasi.gabor@uni-bge.hu.



Association Simulation News



SNE – Simulation Notes Europe

SNE

ARGESIM is a non-profit association generally aiming for dissemination of information on system simulation – from research via development to applications of system simulation. **ARGESIM** is closely co-operating with **EUROSIM**, the Federation of European Simulation Societies, and with **ASIM**, the German Simulation Society. **ARGESIM** is an 'outsourced' activity from the *Mathematical Modelling and Simulation Group* of TU Wien, there is also close co-operation with TU Wien (organisationally and personally).

→ www.argesim.org

✉ → office@argesim.org

✉ → ARGESIM/Math. Modelling & Simulation Group,
Inst. of Analysis and Scientific Computing, TU Wien
Wiedner Hauptstrasse 8-10, 1040 Vienna, Austria
Attn. Prof. Dr. Felix Breitenecker

ARGESIM is following its aims and scope by the following activities and projects:

- Publication of the scientific journal **SNE – Simulation Notes Europe** (membership journal of **EUROSIM**, the *Federation of European Simulation Societies*) – www.sne-journal.org
- Organisation and Publication of the **ARGESIM Benchmarks for Modelling Approaches and Simulation Implementations**
- Publication of the series **ARGESIM Reports** for monographs in system simulation, and proceedings of simulation conferences and workshops
- Publication of the special series **FBS Simulation – Advances in Simulation / Fortschrittsberichte Simulation** - monographs in co-operation with **ASIM**, the German Simulation Society
- Support of the Conference Series **MATHMOD Vienna** (triennial, in co-operation with **EUROSIM**, **ASIM**, and **TU Wien**) – www.mathmod.at
- Administration of **ASIM** (German Simulation Society) and administrative support for **EUROSIM** www.eurosim.info
- Simulation activities for TU Wien

ARGESIM is a registered non-profit association and a registered publisher: **ARGESIM Publisher Vienna**, root ISBN 978-3-901608-xx-y, root DOI 10.11128/z...zz.zz. Publication is open for **ASIM** and for **EUROSIM Member Societies**.

The scientific journal **SNE – Simulation Notes Europe** provides an international, high-quality forum for presentation of new ideas and approaches in simulation – from modelling to experiment analysis, from implementation to verification, from validation to identification, from numerics to visualisation – in context of the simulation process. **SNE** puts special emphasis on the overall view in simulation, and on comparative investigations.

Furthermore, **SNE** welcomes contributions on education in/for/with simulation.

SNE is also the forum for the **ARGESIM Benchmarks on Modelling Approaches and Simulation Implementations** publishing benchmarks definitions, solutions, reports and studies – including model sources via web.

→ www.sne-journal.org,

✉ → office@sne-journal.org, eic@sne-journal.org

✉ → SNE Editorial Office

ARGESIM/Math. Modelling & Simulation Group,
Inst. of Analysis and Scientific Computing, TU Wien
Wiedner Hauptstrasse 8-10, 1040 Vienna, Austria
EiC Prof. Dr. Felix Breitenecker

SNE, primarily an electronic journal, follows an open access strategy, with free download in basic layout. **SNE** is the official membership journal of **EUROSIM**, the *Federation of European Simulation Societies*. Members of **EUROSIM Societies** are entitled to download **SNE** in high-quality, and to access additional sources of benchmark publications, model sources, etc. On the other hand, **SNE** offers **EUROSIM Societies** a publication forum for post-conference publication of the society's international conferences, and the possibility to compile thematic or event-based **SNE Special Issues**.

Simulationists are invited to submit contributions of any type – *Technical Note, Short Note, Project Note, Educational Note, Benchmark Note*, etc. via **SNE's** website:

→ www.sne-journal.org,

Schedule for EUROSIM Conferences and Congress

EUROSIM societies organise the following virtual and in-person events in 2022 and 2023:



The banner features the EUROSIM logo on the left, followed by the DBSS logo (Dutch Benelux Simulation Society) and the website www.eurosim2023.eu. The main text reads: **VESS - VIRTUAL EUROSIM SIMULATION SEMINAR** and **free online seminar series**.

The **EUROSIM Board** and **DBSS** organise **VESS** – the **Virtual EUROSIM Seminar**, a series of online presentations discussing trends in modelling and simulation. These international online simulation seminars – monthly or bi-monthly – are open to everybody, via Zoom, lasting 60 minutes (45 minutes presentations, 15 minutes Q & A). Information and informal registration via website www.eurosim2023.eu



The banner features a background image of a classical building. The text reads: **MATHMOD 2022 Vienna**, *10th Vienna International Conference on Mathematical Modelling*, and **July 27 - 29, 2022, Vienna, Austria**.

MATHMOD organizers continue the conference series one year later, with **10th MATHMOD 2022**, July 27-29, 2022, as *in-person* event. **MATHMOD 2022**, one of **EUROSIM**'s main events, provides a forum for professionals, researchers, and experts in the field of theoretic and applied aspects of mathematical modelling for systems of dynamic nature. The scope of the **MATHMOD 2022** conference covers theoretic and applied aspects of various types of mathematical modelling (equations of various types, automata, Petri nets, bond graphs, qualitative and fuzzy models) for systems of dynamic nature (deterministic, stochastic, continuous, discrete or hybrid) – info and details www.mathmod.at



The banner features a city skyline background. The text reads: **ASIM 2022**, **26. Symposium Simulationstechnik**, **25. - 27. 7. 2022, Wien**. Logos for **asim**, **GI**, and **TU WIEN** are also present.

ASIM - the German / Austrian / Swiss simulation society – is organising the **26th Symposium Simulation Technique – ASIM 2022** at TU Vienna, July 25-27, just before **MATHMOD 2022**. ASIM hopes for a German/English-based event as it used to be before – with personal contacts, and in synergy with **MATHMOD 2022**. – info www.asim-gi.org/asim2022



The banner features a background image of a building at night. The text reads: **EUROSIM 2023**, **AMSTERDAM**, **Summer 2023**, and the **DBSS** logo (Dutch Benelux Simulation Society).

EUROSIM 2023, the **11th EUROSIM Congress**, will take place in Amsterdam, The Netherlands, June 28-30, 2023. It will be organized by the Dutch Benelux Simulation Society (www.dutchbss.org) supported mainly by their corporate members like TU Delft, Amsterdam University of Applied Sciences, EUROCONTROL and IGAMT (www.igamt.eu). Due to the growth of Simulation and its relationship with other analytical techniques like Big Data, AI, Machine Learning, Large Scale Simulation and others, the event will be structured, for the first time, in dedicated tracks focused on different areas and applications of Simulation ranging from aviation to health care and humanitarian activities. Please follow the news and activities towards the **EUROSIM 2023** at www.eurosim2023.eu

ASIM 2022 and MATHMOD 2022 July 25-29, 2022

Due to the critical pandemic situation in Europe the conferences **ASIM 2022** and **MATHMOD 2022** have been shifted to **July 2022**. The organizers invite participants to come to personal face-to-face – conferences – *as conferences used to be* !



ASIM 2022

26. Symposium Simulationstechnik
25. - 27. 7. 2022, Wien

The scope of the *ASIM Symposium Simulationstechnik* – also including the *workshop of the working groups GMMS and STS* – covers basics, methods, and tools of modeling and simulation as well as all areas of application (from engineering sciences to computer science, production and logistics, bio-, environmental and geosciences, climate and ecosystem, up to training and education in modeling and simulation).

The **Scientific Programme** of **ASIM 2022** includes *Invited Lectures*, *Contributed Lectures* in parallel sessions, *Tutorials* in parallel sessions, and a *Forum Simulation Technique*. The **Social Programme** invites for *Conference Dinner* at Monday, for an *Evening Party* on Tuesday (also *Welcome Party of MATHMOD 2022*), and for a '*Strudel Session*' within the *Forum Simulation Technique* on Wednesday.

Conference languages are German and English. Registration is open until begin of conference.

Website: www.asim-gi.org/asim2022

Contact: asim2022@asim-gi.org



MATHMOD 2022
Vienna

10th Vienna International Conference
on Mathematical Modelling

July 27 - 29, 2022, Vienna, Austria

The scope of *MATHMOD 2022* covers theoretic and applied aspects of various types of mathematical modelling (e.g., equations of various types, automata, Petri nets, bond graphs, qualitative and fuzzy models, machine learning) for systems of dynamic nature (deterministic, stochastic, continuous, discrete or hybrid with respect to time).

The **Scientific Programme** of **MATHMOD 2022** includes *Invited Lectures*, *Contributed Lectures* and *Minisymposia Contributions* in parallel sessions, *Tutorials* in parallel sessions (on Tuesday afternoon !), and an *Evening Lecture*. The **Social Programme** invites for *Welcome Party* at Tuesday, for an *Evening Party* on Wednesday (included in the *Evening Lecture*), for a *Heurigen Evening* at Thursday, and for a *Closing Party* at Friday

The reviewing of submitted papers is already finished, and authors have been informed about acceptance. Registration is open until midst of July. See www.mathmod.at for details.

Website: www.mathmod.at

Contact: mathmod@acin.tuwien.ac.at

www.tuverlag.at
ISBN 978-3-903311-31-2

